p-Doping and Valence Band Engineering of ZnO and Epitaxial Growth, Optical Properties and Alloys of Transition Metal Dichalcogenides

A Thesis
Submitted for the Degree of
DOCTOR OF PHILOSOPHY
in the Faculty of Science

by

Rajib Sahu

CHEMISTRY AND PHYSICS OF MATERIALS UNIT
INTERNATIONAL CENTRE FOR MATERIALS SCIENCE
JAWAHARLAL NEHRU CENTRE FOR ADVANCED SCIENTIFIC RESEARCH
Bangalore – 560064, INDIA.
September 2017

Dedicated to

My Parents & Teachers

DECLARATION

I hereby declare that the thesis entitled "***p*-Doping and Valence Band Engineering of ZnO and Epitaxial Growth, Optical Properties and Alloys of Transition Metal Dichalcogenides**" is an authentic record of research work carried out by me at the Chemistry and Physics of Materials Unit, Jawaharlal Nehru Centre for Advanced Scientific Research, Bangalore, India under the supervision of **Prof. Ranjan Datta** and that it has not been submitted elsewhere for the award of any degree or diploma.

In keeping with the general practice in reporting scientific observations, due acknowledgment has been made whenever the work described is based on the findings of other investigators. Any omission that might have occurred due to oversight or error in judgment is regretted.

Rajib Sahu

Rajib Sahu

CERTIFICATE

Certified that the work described in this thesis titled "***p*-Doping and Valence Band Engineering of ZnO and Epitaxial Growth, Optical Properties and Alloys of Transition Metal Dichalcogenides**" has been carried out by Mr. **Rajib Sahu** at the Chemistry and Physics of Materials Unit, Jawaharlal Nehru Centre for Advanced Scientific Research, Bangalore, India under my supervision and that it has not been submitted elsewhere for the award of any degree or diploma.

Prof. Ranjan Datta

(Research Supervisor)

Acknowledgements

I take this opportunity to sincerely thank my research supervisor Prof. Ranjan Datta for his constant motivation, excellent guidance and encouragement throughout my Ph.D. His valuable instructions, comments and suggestions in preparing research manuscripts and for oral and poster presentations at various conferences and for colloquium have helped me immensely. His endless enthusiasm for science and hardworking nature has inspired and motivated me at various times.

I sincerely thank Bharat Ratna Prof. C. N. R. Rao (FRS) for creating world class facilities at International Centre for Materials Science (ICMS). I specially thank him for providing aberration corrected transmission electron microscope facility and pulsed laser deposition for crystal growth facility at this centre which gave me an excellent opportunity to learn and carry out research using advanced microscopy techniques.

I thank the past and present chairman and Int. PhD coordinator of Chemistry and Physics of Materials Unit for all their invaluable support.

I am grateful to Dr. Shetty, Dr. Nagraja, Dr. Dhanya, Dr. Sumanta, Dr. Somnath, Prof. S. C. Peter and Prof. C. Narayan for fruitful collaboration.

I would like to take this opportunity to specially thank all the professors who offered me courses on various subjects, starting from Prof. S. Balasubramanian, Prof. G. U. Kulkarni, Prof. H. Ila, Prof. S. M. Shivaprasad, Prof. K. S. Narayan, Prof. A. Sundaresan, Prof. S. Easwaramoorthy, Prof. C. Narayan, Prof. S. K. Pati, Prof. U. V. Waghmare, Prof. S. Narasimhan, Prof. N. S. Vidyadhiraja, Prof. R. Ganapathi and Prof. R. Datta for their excellent teaching and the courses they have offered.

I would like to thank the entire faculty at JNCASR for being a constant source of inspiration with their advanced research. I take this opportunity to thank all my past teachers at school and college level for sharing their knowledge, providing their support and encouragement without which it is impossible for me to be here. Especially I would like to acknowledge Pranab da, Bidhan da and Motim da from Visva Bharati University, being always a constant inspiration for research.

I take this opportunity to thank my past and present lab mates, Dr. Loukya, Dr. Dileep, Dr. Devendra, Mr. Badri, Ms. Usha, Ms. Sharon, Mr. Ankit and Mr. Rajendra for their useful discussions and creating a cheerful environment.

I extend my gratitude to all the efficient staff at the Library, Academic, Administration sections and Hostel for their timely help and cooperation.

I acknowledge and thank all my friends from the integrated PhD-2011 batch - Abhijit, Ragesh, Sonu, Uttam, Suchitra, Mohini, Krishnendu, Sushela, Nileema, Pallabi, Monali, Dipwanita and Debopreeti. I also thank all the friends I made in JNCASR while at recreation and sports, Dr. Pralok, Dr. Chandan, Anshul, Arkmita, Kousik, Sisir, Debdipto, Manoj, Anaranaya, Subhajit, Somnath, Jiya, Arpan, Soumabrata, Samantak, Niloy, Shreyan, Satya, Sudip, Chaitali and Manodeep.

I finally acknowledge and thank all my parents and family members for their unconditional love, support and encouragement.

Synopsis

There are two different topics presented in the present thesis. The first part deals with the *p*- doping issues on ZnO thin film and second topic is large area epitaxial growth and poly-type (2H to 1T) phase transition in transition metal dichalcogenides (TMDs).

p-doping problem in ZnO is studied in two different ways; a) valance band engineering by Te substitution at the O site along with the acceptor doping (Li) and b) acceptor doping (Li and BN) in ZnO. In case of Te doped ZnO, we have shown how to control the Te location at both Zn and O sites. A band bowing parameters of ~7 eV is obtained for Te at O site. However, incorporation of acceptor dopant at ZnO:Te and subsequent annealing did not render the film *p*-type because of formation of Schottky-I defect. In case of Li doped ZnO, it is found that Li occupies both the substitutional and interstitial positions and does not lead to *p*-type conductivity in the system. Oxygen vacancy defect concentration in ZnO lattice affects relative separation between the Li_i-Li_{Zn} and tunes the optical emission in this system. In case of BN co-doped of ZnO, we obtain stable *p*-type conductivity due to the off stoichiometry of BN_{1+x} in the lattice. Stable *p*-type conductivity with a carrier concentration and mobility of ~3×10^{16} cm^{-3} and ~10 $cm^2/V.s$ are achieved in film grown at higher oxygen partial pressure (~10^{-1} Torr). It is also found that BN is a good dopant compared to the Li in terms of possibility of occupation of intestinal positions.

In the second part of the thesis, we demonstrate large area epitaxial thin film growth of MoS_2 and WS_2 with control over layer numbers by pulsed laser deposition. Sapphire substrate is found to induce compressive strain in the layer and blue shifts the band gap of both MoS_2 and WS_2. Poly-type phase transition (2H↔1T) in MoS_2-ReS_2 and WS_2-ReS_2 alloy systems are studied both experimentally and theoretically. Rich variations of low dimensional structural modulation are observed in MoS_2-ReS_2 and WS_2-ReS_2 system. It is predicted from theory the 50% alloy system is suitable for nano-scale switching device due to small energy barrier between metal and semiconductor states.

List of Publications

1. **R. Sahu,** K. Dileep, B. Loukya, R. Datta, Native defects affecting the Li atom distribution tune the optical emission of ZnO:Li epitaxial thin film, ***Applied Physics Letters,*** *104, 051908 (2014).*

2. **R. Sahu,** K. Dileep, D. S. Negi, K. K. Nagaraja, S. Shetty, R. Datta, Structural and optical property characterization of epitaxial ZnO:Te thin films grown by pulsed laser deposition, ***Journal of Crystal Growth,*** *410, 69-76 (2015).*

3. **R. Sahu,** K. Dileep, D. S. Negi, K. K. Nagaraja, R. Datta, Ambipolar behavior of Te and its effect on the optical emission of ZnO:Te epitaxial thin film, ***Physica Status Solidi (b),*** *252 (8), 1743-1748 (2015).*

4. **R. Sahu,** H. B. Gholap, G. Mounika, K. Dileep, B. Vishal, S. Ghara, R. Datta, Stable p-type conductivity in B and N co-doped ZnO epitaxial thin film, ***Physica Status Solidi (b),*** *253 (3), 504-508 (2016).*

5. **R. Sahu,** D. Radhakrishnan, B. Vishal, D. S. Negi, A. Sil, C. Narayana, R. Datta, Substrate induced tuning of compressive strain and phonon modes in large area MoS_2 and WS_2 van der Waals epitaxial thin films, ***Journal of Crystal Growth,*** *470, 51-57 (2017).*

6. **R. Sahu,** U. Bhat, N. M. Batra, H. Sharona, B. Vishal, S. Sarkar, S. Assa Aravindh, S. C. Peter, I. S Roqan, P. M. F. J. D. Costa, R. Datta, Nature of low dimensional structural modulations and relative phase stability in $Re_xMo(W)_{1-x}S_2$ transition metal dichalcogenide alloys, ***Journal of Applied Physics,*** *121, 105101 (2017)* (Selected as ***Feature article*** and ***Front Cover page***).

7. D. S. Negi, B. Loukya, K. Dileep, **R. Sahu,** K. K. Nagaraja, N. Kumar, R. Datta, Robust room temperature ferromagnetism in epitaxial CoO thin film, ***Applied Physics Letters,*** *103(24), 242407 (2013).*

8. K. Dileep, **R. Sahu,** K. K. Nagaraja, R. Datta, Crystallographic phase separation and band gap of $ZnO_{1-x}S_x$ (x = 0.1-0.3) alloy thin films grown by pulsed laser deposition, ***Journal of Crystal Growth,*** *402, 124-129 (2014).*

9. D. S. Negi, B. Loukya, K. Dileep, **R. Sahu,** S. Shetty, N. Kumar, J. Ghatak, N. Pachauri, A. Gupta, R. Datta, Structural and magnetic characterization of mixed valence Co (II, III)xZn1-xO epitaxial thin films, ***Journal of Magnetism and Magnetic Materials,*** *354, 39-43 (2014).*

10. K. Dileep, **R. Sahu,** S. Sarkar, S. C. Peter, R. Datta, Layer specific optical band gap measurement at nanoscale in MoS_2 and ReS_2 van der Waals compounds by high resolution electron energy loss spectroscopy, ***Journal of Applied Physics,*** *119, 114309 (2016).*

11. B. Loukya, D. S. Negi, **R. Sahu,** N. Pachauri, A. Gupta, R. Datta, Structural characterization of epitaxial LiFe5O8 thin films grown by chemical vapour deposition**,** ***Journal of Alloys and Compounds,*** *668, 187-193 (2016).*

12. B. Vishal, **R. Sahu,** U. Bhat, R. Datta, Investigation of microstructural details in low thermal conducting thermoelectric Sn1-xSbxTe alloy, ***Journal of Applied Physics,*** *122 (5), 055102 (2017).*

Contents

Part I

Chapter I

Valence band engineering and highly soluble acceptor dopants; possible solutions to overcome p-type doping problem in ZnO

This chapter gives a brief introduction to 'p-type doping problem' in ZnO along with our approaches towards solving this problem by valence band engineering and highly soluble acceptor dopants. Chapter I also describes how to grow epitaxial thin film on highly lattice mismatched sapphire (α-Al_2O_3) substrate.

1.1 *p* - Doping problem in ZnO

ZnO is a wide band gap (~3.3 eV) semiconductor at room temperature with high excitation binding energy (~60 meV) making it extremely attractive in many optoelectronic applications, e.g., light emitting diodes (LEDs), laser diodes (LDs), transparent semiconductors, and photovoltaic [1-2]. Compared to GaN, which is already in application, ZnO is significantly cheaper and offers alternatives to overcome the cost associated with GaN technology [2]. GaN is the most important semiconductor after silicon [3]. The market of lighting industry will be amount to 120 billion by 2020 [4]. This huge lighting industry can be accessible if ZnO based technology can be realized. However, stable *p*-doping remains elusive in this system, thus hindering its application in bi-polar devices [5]. Extensive research is being pursued to understand the problem and overcome the difficulty. The first part of this thesis is directed towards this challenge by one of the several approaches already proposed in the literature i.e. by pushing the valence band upwards towards the vacuum level and at the same time understanding the role of native defects their role and control in this system. We have grown epitaxial forms of ZnO films so that any success can be translated immediately to device fabrication stage.

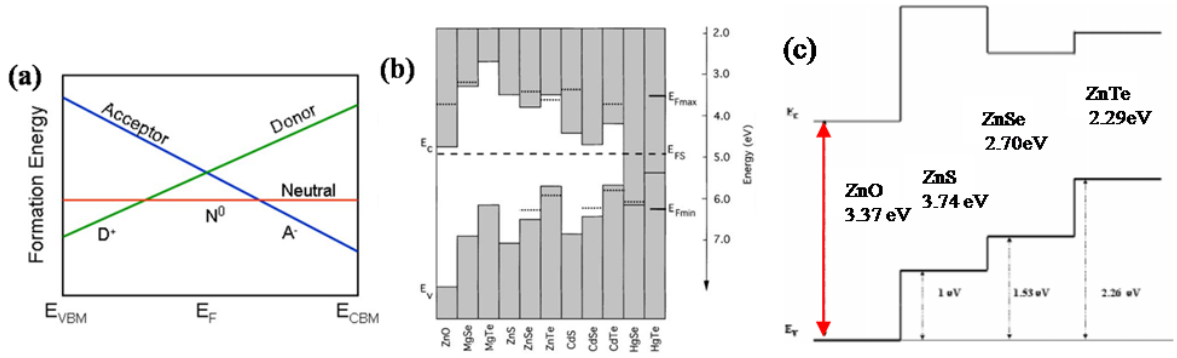

Figure 1.1 (a) Schematic model showing the dependence of defect formation energy as a function of Femi level (E_F) position. Copyright (2010) by IEEE [5]. (b) Band offsets and the Fermi level stabilization energy, E_{FS}, in II–VI compounds and (c) Band offsets of ZnX (O, S, Se and Te) compounds. Copyright (2010) by Elsevier [9]. The valence band offset progressively shifts toward vacuum level as O is replaced with S, Se and Te.

p-type doping problem in ZnO is a great challenge to the researchers working towards realizing the all ZnO based practical devices. This *p*-type doping issue in ZnO is known also 'doping asymmetry problem' and similar to many band insulator where one type of

conductivity can easily achieved. The three fundamental obstacles identified to *p*-type doping problem in ZnO based on literature and our experiences; (i) limited solubility of *p*-type impurities in ZnO, (ii) deep acceptor level and (iii) spontaneous formation of defects (intrinsic defects, figure 1.1(a)) which compensate *p*-type impurities [5]. It was already pointed out that the native defects form spontaneously in order to main the Femi level stabilization energy in the system which determines the limit up to which a particular doping can be obtained.

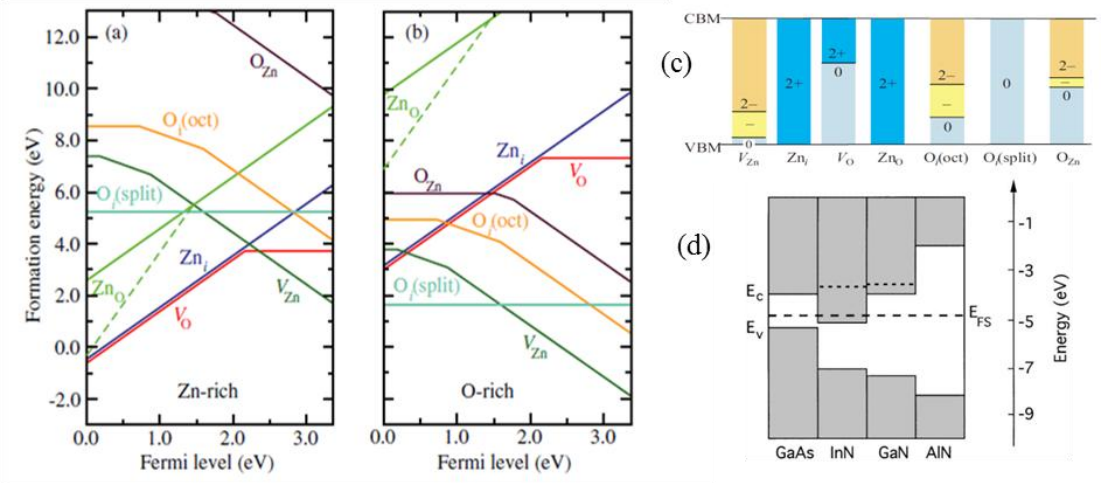

Figure 1.2 (a) and (b) show the variation of formation energy of defects as a function of Fermi level position, (c) shows the position of VBM and CBM. Copyright (2007) by American Physical Society [6]. (d) shows band energy with respect to E_{FS}. Copyright (2010) by Elsevier [9].

Theoretically, it has been shown how the possible intrinsic native defects are formed as a function of Fermi energy as well as the chemical potential of either Zn or O in figure 1.2 [6]. Oxygen vacancies, zinc interstitials, and zinc anti-sites are donor defects and zinc vacancies, oxygen interstitials and oxygen anti-sites are known as acceptor defects. When one is trying to dope *p*-type (*n*-type) by moving E_F toward the valance band maximum E_{VBM} (conduction band minimum E_{CBM}), the donor (acceptor) defect formation energies become lower leading to the spontaneous formation of compensating defects. Vidya *et al.* [7] have calculated the formation energies of different vacancy complexes which are formed by the combination of two or more of the individual defect species mentioned here. It has been found that all of these defects complexes, (V_O+ Zn_i), (V_O+ V_{Zn}), (V_O+ O_i) and (V_{Zn}+ Zn_i) have too high formation energies to be feasible at room temperature under thermodynamic equilibrium. Among all the possible impurities, hydrogen stands out an unintentional incorporation donor impurities [8]. Chris G.Van de Walle has observed substitution hydrogen

acts as a shallow donor having lowest formation energy can explain the conductivity in *n*-type ZnO.

Walukiewicz has shown in his 'amphoteric defect model' that for sufficiently high defect density (when the properties of materials are fully controlled by native point defects), Fermi energy becomes 'stabilized' to a value called as 'Fermi level stabilization energy' (E_{FS}) and becomes insensitive to any further damage [9]. Amphoteric suggests defects can reversibly transform between donor and acceptor as a function of Fermi level position. A pure material having high defect density will have E_F pinned to E_{FS}. Introducing acceptor (donor) impurities the donor (acceptor) will form resulting in a shift of E_F back towards E_{FS} because of the amphoteric nature of these defects. Figure 1.1 (b) shows the schematic energy band offsets with respect to E_{FS} for various II-VI semiconductors. The doted line represents the position of the Fermi energy corresponding to the highest electron/hole concentration reported in these materials.

1.2 Our contributions and approaches

Figure 1.1 (b) shows ZnO has its E_{VBM} deep down in the energy compared to E_{FS}. The deep low value of E_{VBM} is due to high electronegativity of Oxygen which hinders *p*-type doping in ZnO. On the other hand, GaN has just been lucky to overcome from this problem. O. Masimov has come up the idea of improving the *p*-type doping through anion substitution with electronegative group VI elements such as S, Se and Te [10]. These anionic substitutions will shift valance band higher in energy and brings E_{VBM} closer to E_{FS} and also will make deep acceptor level shallow.

Dileep *et al.* has incorporated 17 at. % S in ZnO as a single phase epitaxial thin film which shows a valence band shift of ~ 0.2 eV [11, 12]. Our group has found that Ag and Li are 'not good dopants' to activate *p*-type carriers in ZnO with S. We have found that both Li and Ag are occupying both substitutional and interstitials position in ZnO lattice. This interstitials positions compensate the *p*-type activity in ZnO.

From our experiences, we came up with two different possible approaches to overcome this *p*-type doping problems in ZnO.

- Valance band engineering with Te doping
- Reduction of ionization energy to activate *p*-type carries with Li and BN co-doping.

Figure 1.1 (b) shows valance band of ZnTe is much higher than ZnO with respect to E_{FS}, so there is probability to raise the valance band of ZnO if we could incorporate high % of Te at

oxygen site in ZnO. We have found that Li has higher solubility and lower ionization energy (0.09 eV) in ZnO which could be effective to activate *p*-type carriers [13, 14]. Our attempt with BN co-doping is due to increase the solubility of dopants in ZnO to reduce ionization energy between acceptor and host.

The primary aim of our effort related to this topic is to grow epitaxial and single phase alloy which will ensure the best performance and allow ionization of dopants (Li and B) and valance band engineering ZnO (by Te) on highly lattice mismatched sapphire (18% for ZnO on c-plane sapphire.

1.3 Epitaxial thin film growth of ZnO on highly lattice mismatched substrate (18%) of *c*-plane sapphire substrate

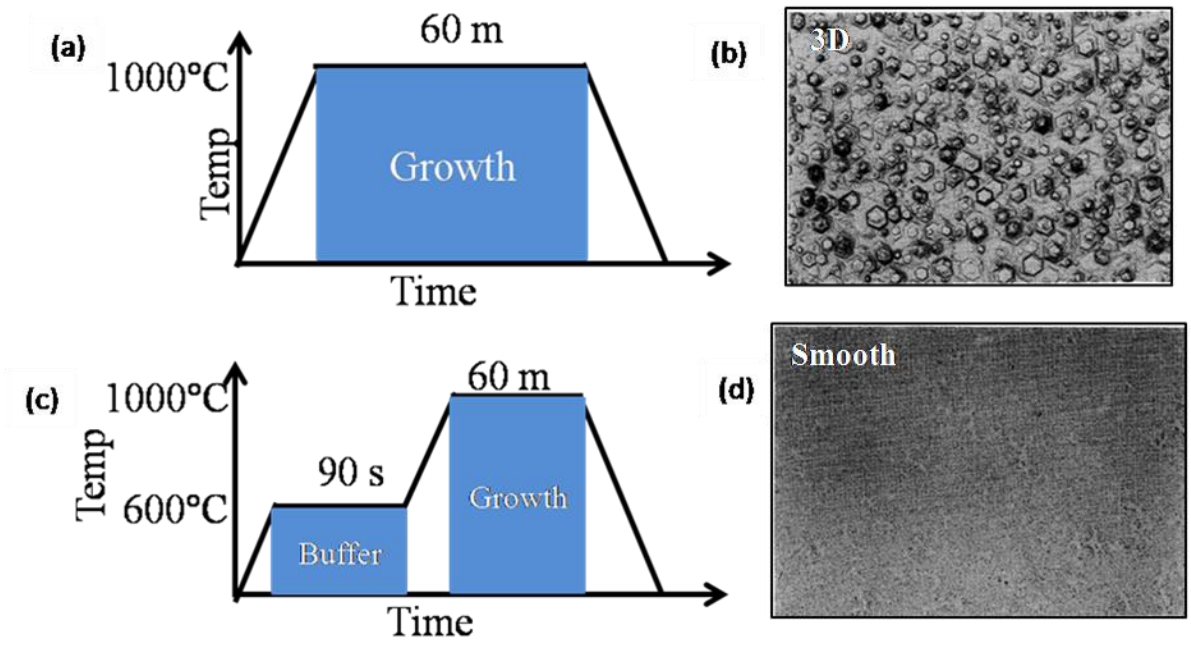

Figure 1.3 (a) The growth scheme for single step growth, (b) shows interference micrograph for the three dimensional island-like growth in a single step. (c) The growth scheme for the two step growth and (d) Mirror-like surface for the two-step growth scheme. Copyright (2010) by the Japan Society of Applied Physics (JSAP) [15].

The *p*-type doping problem in ZnO is quite similar to the *p*-type doping issue faced by the scientific community during the early research of GaN. Both GaN and ZnO have highly lattice mismatch (16%) with the sapphire substrate. Suji Nakamura, using pure

materials science based approach has solved the three major challenges for realizing GaN based devices. Based on a two-step growth approach he could grow an epitaxial thin film of GaN on highly lattice mismatched (16%) sapphire using metal organic chemical vapour deposition (MOCVD) [15].

He has observed 3D island growth of GaN on sapphire at 1000°C for 60 minutes. This problem was solved when a two step growth method is employed, a nucleation layer of GaN directly on sapphire at 600°C for 90 seconds ensured complete wetting of the substrate which when followed by annealing and a subsequent growth for 60 minutes at 1000°C ensured an optically flat and smooth film with mirror-like finish. From this transmission electron microscopy images, it is clear that this poorer epitaxy has to improve with much slower kinetics of PLD.

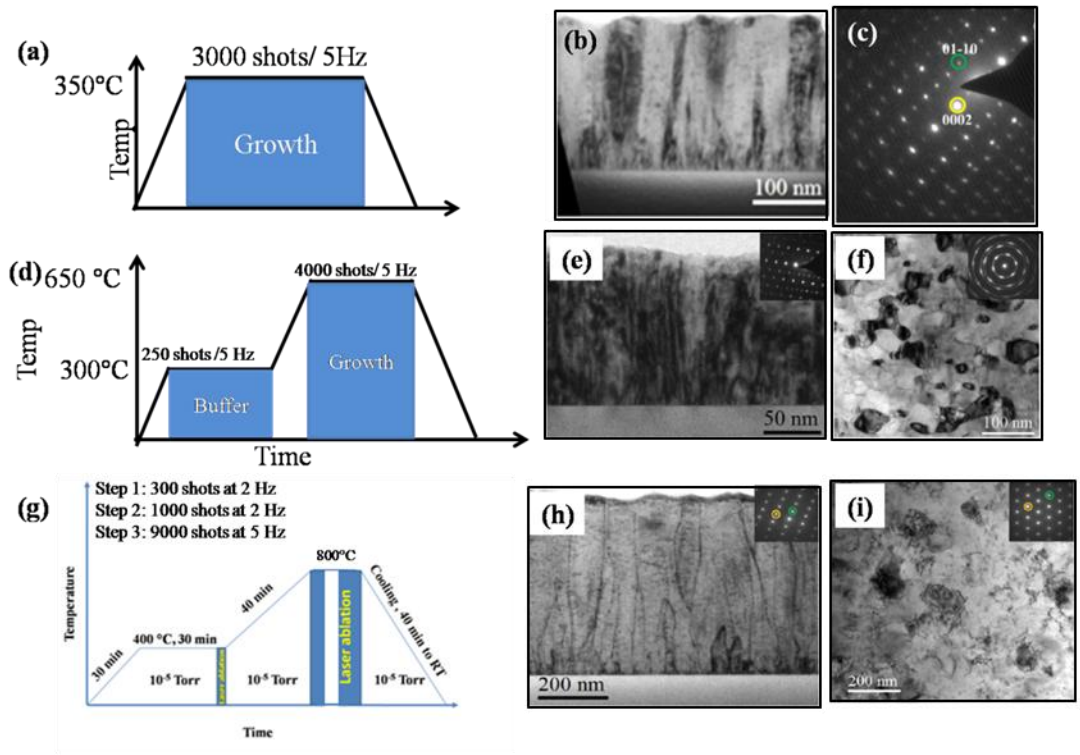

Figure 1.4 Growth scheme for (a) one step, (d) two step and (g) three step method. (b) TEM crosssectional image and (c) diffraction pattern from sample grown with one step. (e) Cross sectional image and (f) plan view image of two step grown sample. (h) Cross sectional image and (i) plan view image of three step grown sample. Copyright (2010) by Elsevier [17].

We have extended this two-step method to three step method in our growth strategy of ZnO on sapphire by pulsed laser deposition (PLD) [16]. PLD system is much cheaper but it has much faster growth rate than MOCVD. B. Loukya *et al.* has studied systematically the effect of various growth parameters like nucleation layer temperature, initial deposition rate (laser ablation frequency), nucleation layer growth kinetics, initial temperature and pressure, final growth temperature and pressure, number of steps of deposition and annealing duration for depositing high quality epitaxial thin film of ZnO on highly lattice mismatched sapphire substrate [17].

Figure 1.4 (a) shows a single step growth, i.e. 3000 laser pulse shots at 5 Hz at 350°C gives a film which shows streaking of spots with high g indicating rotation of grains. To solve this problem, a two step method was introduced where a buffer layer of 250 shots at 5 Hz at 300°C followed by ramping to 650°C in 30 minutes plus annealing for 10 minutes at 10^{-5} Torr. Annealing was required to improve the crystalline quality and establish large area epitaxial relationship with the substrate. The final growth temperature was 650°C with 4000 shots at 5 Hz at 10^{-5} Torr pressure (figure 1.4 (d)). The cross sectional bright field image of the film showed Moire fringes due to rotation of grains. The plan view bright field image showed the rotated grains with dark field contrast) and it is clearly demonstrated by rotation of spots in PV diffraction (inset of figure 1. 4 (f)).

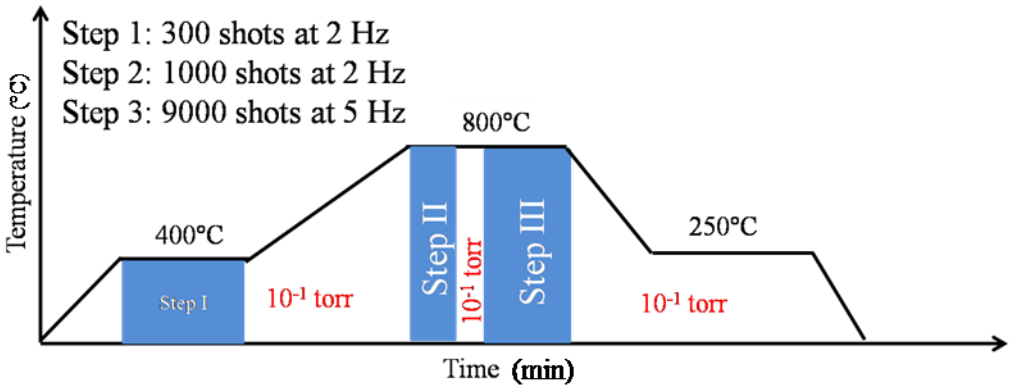

Figure 1.5 Schematic diagram of the resistive type or r-type growth.

A three step growth method was introduced with slower kinetics to allow the nucleation layer to relax, where the nucleation layer was grown at 400°C for 300 shots at 10^{-5} Torr with a very slow growth rate (2 Hz/1 Hz pulse rate of the laser) in order to allow sufficient time

for relaxation. In the second step, the growth was followed by ramping to 800°C in 40 minutes, followed by annealing at 800°C for 20 minutes at 10^{-5} Torr, followed by a slow (2Hz) second step growth at 800°C for 1000 shots at 10^{-5} Torr. The third step was started after a further annealing for 10 minutes at 800°C, for 9000 shots at 10^{-5} Torr. The system was slowly cooled down to room temperature in 2 hours at 10^{-3} Torr (figure 1. 4 (g)). Both cross sectional and plane view images showed a single crystalline pattern and the rotated grain density has significantly reduced as demonstrated by the plan view image.

This three step method for epitaxial growth has been slightly modified depending on the need of dopant, but the mechanism is constant. Sometimes we need buffer layer for better epitaxy and to remove 3D island. The three step growth mention above shows spontaneous *n*-type conductivity with a carrier concentration ~ 10^{19} cm^{-3} and a resistivity ~0.3 **Ω**.cm. This growth scheme will be called *n-type* growth throughout the thesis. We have extended this growth technique with extensive annealing in between growth shown in figure 1.5, addressed as *r-type* growth. While retaining the crystalline quality with this growth scheme, we obtained a carrier concentration of ~ 10^{15} cm^{-3} and a resistivity ~ 3000 **Ω**.cm.

We have used the experiences and the success of this work in growing high quality epitaxial, single crystalline Li:ZnO, ZnO:Te and BN:ZnO thin films described in chapter III-V.

1.4 Overview of the thesis based on part I

In the chapters III-V, we have understood the effect of both intrinsic and extrinsic defects in ZnO and addressed the '*p*-type doping problem' in ZnO. To begin with chapter III, we have engineered valance band through Te doping in ZnO. We have systematically studied ambipolar behavior, crystallographic phase separation and optical properties of $ZnO_{(1-x)}Te_x$ and $Zn_{(1-x)}Te_xO$ alloys thin film grown by pulsed laser deposition (PLD) on the c-plane sapphire substrate. We chosed Te as a possible candidate for valance band engineering to facilitate *p*-type carriers in ZnO. Incorporation of Te at the oxygen (Te_O) or zinc (Te_{Zn}) site can be controlled through the deposition scheme to transfer Te during the film growth. The solubility of Te at the oxygen site is strongly dependent on the growth temperature and a maximum of ~ 4 at.% Te is obtained at 400 °C with the film remained to be in epitaxial form. For Te at the Zn site a maximum of ~ 3.4 at. % is achieved with the film to be in the epitaxial form with tilt and phase separation is observed beyond this composition. Band gap decreases with Te incorporation both in the oxygen and zinc sites but a decrease in band gap is found to

be pronounced and composition dependent for the former case. An experimental band bowing parameter of ~7 eV is obtained for Te_O and in agreement with mBJLDA based theoretical calculation.

Next work shows native defects affecting Li atom distribution to tune optical emission of Li:ZnO epitaxial thin film. Using first principle based mBJLDA calculation we have understood how the optical emission id affected by defects and defects complexes like V_O, Li_{Zn}-Li_i and Schottky defect type I. Band gap measurement using EELS and cathodoluminescence (CL) match with the type (direct/indirect) and value predicted for Schottky defect (V_{Zn} + V_O) type I by mBJLDA calculated band gap.

In the next work, we have co-doped simultaneously both B as cation and N as an anion in ZnO to increase the solubility of dopants. In this growth, we have used ZnO buffer layer between the film and substrate to get 2D morphology and smooth surface of the film. We have observed films grown at higher oxygen partial pressure (~10^{-1} Torr) shows *p*-type conductivity with a carrier concentration of ~3×10^{16} cm^{-3}. This *p*-type conductivity is associated with the significant decrease in defect emission peaks due to the vacancy oxygen (V_O) and Schottky type-I native defects compared to films grown at low oxygen partial pressure (~10^{-5} Torr). The *p*-type conductivity is explained with the help of density functional theory calculation considering off-stoichiometric BN_{1+x} in the ZnO lattice.

1.5 Bibliography

[1] W.W. Wenas, A. Yamada, K. Takahashi, M. Yoshino, M. Konagai, J. Appl. Phys. **70**, 7119 (1991).

[2] U. Özgur, Ya. I. Alivov, C. Liu, A. Teke, M. A. Reshchikov, S. Dogan, V. Avrutin, S. J. Cho, H. Morkoc, J. Appl. Phys. **98**, 041301 (2005).

[3] C. J. Humphreys, MRS Bulletin **33**, 459 (2008).

[4] *www.ledsmagazine.com*

[5] V. Avrutin, H. Morkoc, Proc. IEEE **98**, 1269 (2010).

[6] A. Janotti, C. G. Van de Walle, Phys. Rev. B **75**, 165202 (2007).

[7] R. Vidya, P. Ravindran, H. Fjellvag, G. B. Svensson, E. Monakhov, M. Ganchenkova, M. R. Nieminen, Phys. Rev B **83**, 045206 (2011).

[8] C. G. Van de Walle, Physica B **308**, 809-903 (2001).

[9] W. Walukievicz, Physica B **302**, 123 (2001).

[10] O. Maksimov, Rev. Adv. Mater. Sci. **24**, 26 (2010).

[11] K. Dileep, R. Datta, J. All. and Comp. **586**, 499 (2014).

[12] K. Dileep, R. Sahu, K. K. Nagaraja, R. Datta, J. Cryst. Growth **402**, 124 (2014).

[13] C. H. Park, S. B. Zhang, S. Wei, Phys. Rev. B **66**, 073202 (2002).

[14] J. B. Yi, C. C. Lim, G. Z. Xing, H. M. Fan, L. H. Van, S. L. Huang, K. S. Yang, X. L. Huang, X. B. Qin, B. Y. Wang, T. Wu, L. Wang, H. T. Zhang, X. Y. Gao, T. Liu, A. T. S. Wee, Y. P. Feng, J. Ding, Phys. Rev. Lett. **104**, 137201 (2010).

[15] S. Nakamura, J. J. Appl. Phys. **30**, 1705 (1991).

[16] J. Narayan and B. C. Larson J. App. Phys. **93**, 278 (2003).

[17] B. Loukya, P. Sowjanya, K. Dileep, R. Shipra, S. Kanuri, L. S. Panchakarla, R. Datta, J. Cryst. Growth **329**, 20 (2011).

Chapter II

Experimental methods, advanced techniques for characterization, and theoretical tools

This chapter gives a brief description about experimental methods, advanced techniques like electron energy loss spectroscopy, and theoretical methods like WIEN2k based density functional theory and FEFF based excited state calculation.

2.1 Pulsed laser deposition

Epitaxial thin film growth is essential for any device fabrication and applications. Pulsed laser deposition (PLD) is one of the promising techniques for the formation of true layer by layer growth of transition metal oxides, complex-oxides heterostructure, super lattice and well controlled interface [1-6]. The development of pulsed laser to introduce the stoichiometric transfer of materials from solid pellet to substrate, simulating flash evaporation methods, is reported in the literature as early as 1965 [7], where a ruby laser was used to grow films of semiconductors and dielectrics. The breakthrough for PLD was its successful usefulness in the application to in-situ growth of epitaxial high temperature superconductors in 1987 at Bell Communications Research [8]. The PLD mechanism works as laser ablation, plasma formation, plume propagation as well as nucleation and growth. The basic idea of PLD is to exploit high power lase pulse in order to evaporate a small amount of matter in plasma state from a solid target [9]. The focus laser pulses are absorbed at the target surface to break any chemical bond of molecules in the volume due to sufficient absorbed energy density. Among various thin film growth technology pulsed laser deposition (PLD) is most suitable for laboratory experimentations and less expensive compared to other technologies e.g., metal organic chemical vapor deposition (MOCVD), molecular beam epitaxy (MBE), atomic layer deposition (ALD) etc. PLD has advantages compared to other growth methods like

- For uniform growth, one needs large number of nucleation sites. This could be possible when a laser is pulsed a super saturation of the target materials arrives at the substrate. This super saturation causes a large number of nucleation sites on substrate.
- Another advantage of PLD is to control the film stoichiometry very precisely than other methods. In PLD the optimum stoichiometry of the film come from the ability to produce a target with the desired composition, this is an advantage compared to other techniques such as MBE where the composition has to be produced by controlling the ratio of the different sources arriving on the substrate.
- The deposition rate is higher than other techniques which show competing control over stoichiometry.
- PLD is a versatile technique and can be used to grow very wide range of materials including metals, semiconductors, borides, carbides, nitrides, oxides, fluorides, silicides and sulfides.

- Due to high background pressures in PLD chamber (e.g. oxygen, sulpher) allows the stoichiometry of oxide targets to be maintained during grown of thin films.
- This cost effective for large scale production than other methods.

Our PLD method based on two steps process, one is the low temperature nucleation and second is high temperature growth. We have used the rotatory pump here to create vacuum in PLD chamber and from that we can creat the vacuum level up to 10^{-6} Torr. Excimer laser (KrF, $\lambda \sim 248$ nm) with 150 mJ energy (~1.5 J cm^{-2} energy density at the target) is used to ablate target sample. Distance between the substrate and target is kept at ~5 cm. Though high quality ZnO substrates are available in the market for the homo-epitaxial growth, but they are relatively expensive compared to single crystal sapphire. Therefore, our epitaxial growth scheme was developed for highly lattice mismatched (~ 16%) c-plane oriented sapphire. Single crystal sapphire substrate is relatively less expensive and robust against range of growth temperature and chemical environment. We have developed epitaxial growth scheme of ZnO on sapphire in a PLD which consist of three stages of growth mentioned in chapter I. Direct growth of ZnO on sapphire at higher temperature does not wet the surface and three dimensional discrete islands form (Volmer Weber type). It is therefore important to wet the substrate first and this is performed by depositing ZnO nucleation layer at low temperature (400 °C). Final growth takes place at 800 °C. The schematic is shown in the figure 2.1

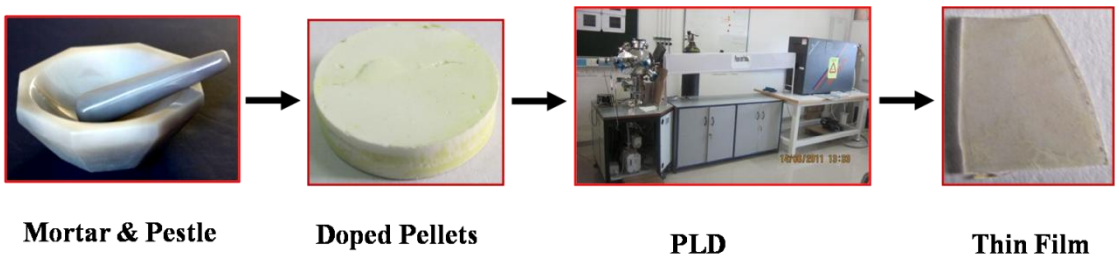

Figure 2.1 Schematic of Pulsed Laser Depostion growth. Solid targets are made using solid state synthesis for laser ablation.

Those solid target pellets are synthesized in solid state reaction method in our lab to use in PLD. First we make solid sintered pellet by grinding and crushing solid powder using mortar and pestle and give a shape under 20 kN pressure. Now the pellet is sintered in the furnace at

elevated temperature to make it hard for laser ablation. Depending on our projects, we change the growth methods.

2.2 TEM sample preparation

We have used mechanical polishing and followed by Ar+ ion milling for perforation to generate large electron transparent areas for transmission electron microscopy samples. For TMDs sample, we have taken special cares so that the weekly van der Waal layers should not be detached from the sapphire substrate.

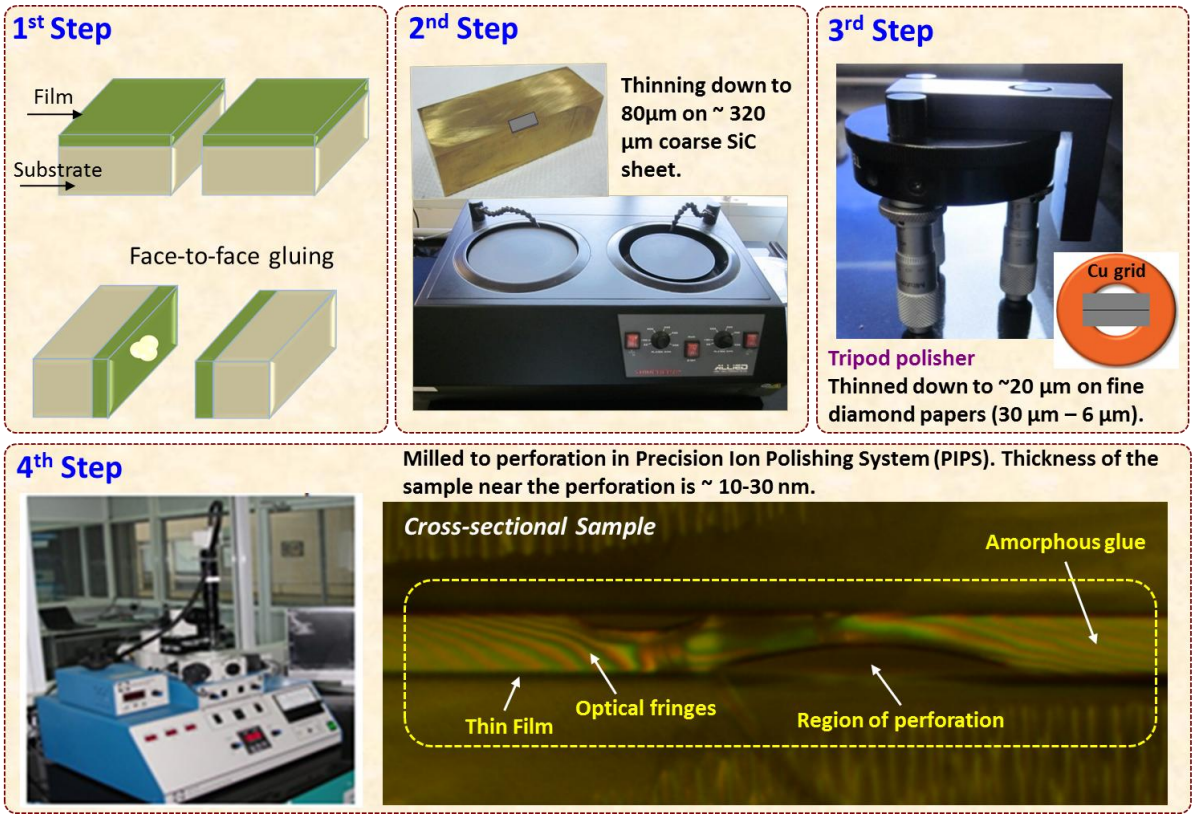

Figure 2.2 Step-by-step TEM cross-sectional sample preparation. Step 1 to step 4 describes how we have thinned down the sample thickness to ~20 µm using mechanical polishing, SiC and diamond poling paper. At the end Precision Ion Polishing (PIPS) is necessary to obtain an electron transparent thin area.

Figure 2.2 shows different steps involved in the TEM sample preparation method. In the first step we glue the sample face-to-face and prepare a sandwich. Now it is mounted on a brass block with a temporary mounting wax having melting point of 140 °C. In the second

step we polish it mechanically along the cross-sectional direction in order to shape it to fit within Cu grid of diameter 3 mm and reduce the thickness below 80 µm. We use SiC polishing paper for mechanical polishing. In the next step, we use diamond polishing sheet of varying grit sizes from 30 to 6 µm to further thin it down to ~20 µm. In the final step, the sample is mounted on to a Cu grid and milled in the Ar+ ion polishing system to perforation. The beam settings used in PIPS were +8° and -8° angles for left and right guns with double modulation and with 4.5 kV of energy. The energy was reduced to 3 kV in the end to remove any amorphous layers.

2.3 Electron energy loss spectroscopy in TEM

Mainly two types of interaction between fast electrons and materials in TEM can be classified as elastic and inelastic category [10-15]. Elastic interaction has only momentum exchange but inelastic has both exchange of energy and momentum between electron and atomic constituents namely nucleus and electrons. Generally EELS, vortex, EMCD are considered as inelastic interaction whereas Lorentz forces, dipole-dipole interaction, magnetic phase imaging, Arahnov-Bomb effect show elastic interaction in TEM.

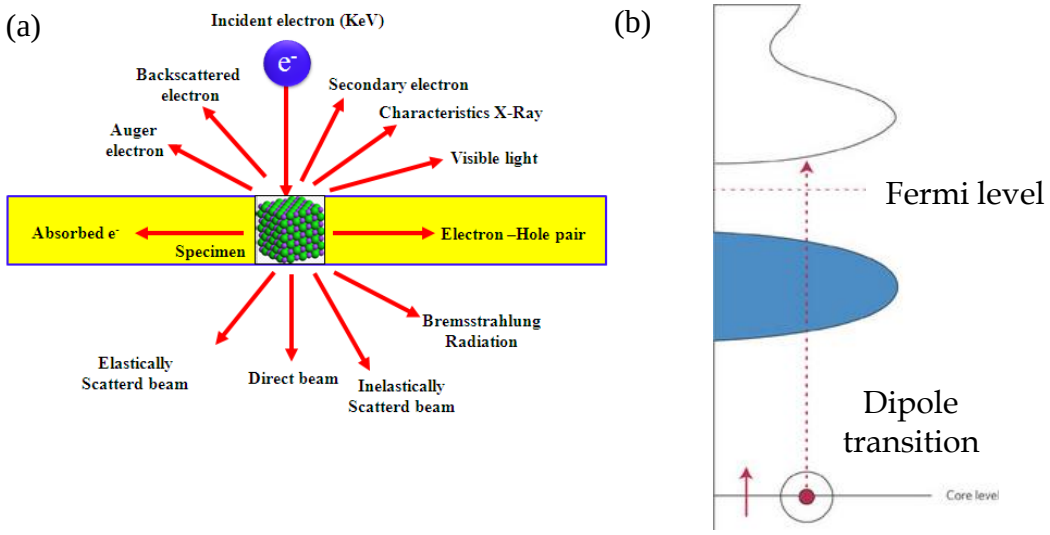

Figure 2.3 (a) Types of interaction between electron and matters. (b) Electronic transition in Electron energy loss spectroscopy.

The elastic scattered electrons form a peak of highest intensity known as the 'zero loss peak' (ZLP) in EELS and the major contribution comes from the in elastically electrons forming a spanning up to 2000 eV accessible through the spectrometer (figure 2.4 (b)). Among various type of interaction, we have considered mainly two varieties, firstly low loss spectra within few eV from the ZLP which gives information about band gap (figure 2.4 (c)) and second type is core loss spectra e.g., O K edge (figure 2.4 (d)) which provides information on density of unoccupied states. The low-loss EELS provides intensity due to excitation of weakly bound outer-shell electrons of the atoms and core-loss EELS contains information of electronic transition from the core level of atoms to the unoccupied levels above the Fermi level (E_F) of the absorbing atom. The spectrum till ~50 eV from any core loss absorption onset is known as electron energy loss near edge structure (ELNES) which provides information on the surrounding electronic structure of the absorbing atoms and the spectra beyond 50 eV is known as electron energy loss extended fine structure (EXELFS) which provides information on the bonding environment and co-ordination. Both ELNES and EXELFS are compared with XANES and EXAFS techniques in X-ray absorption performed in a synchrotron. Both the techniques have their own advantages and disadvantages over each other.

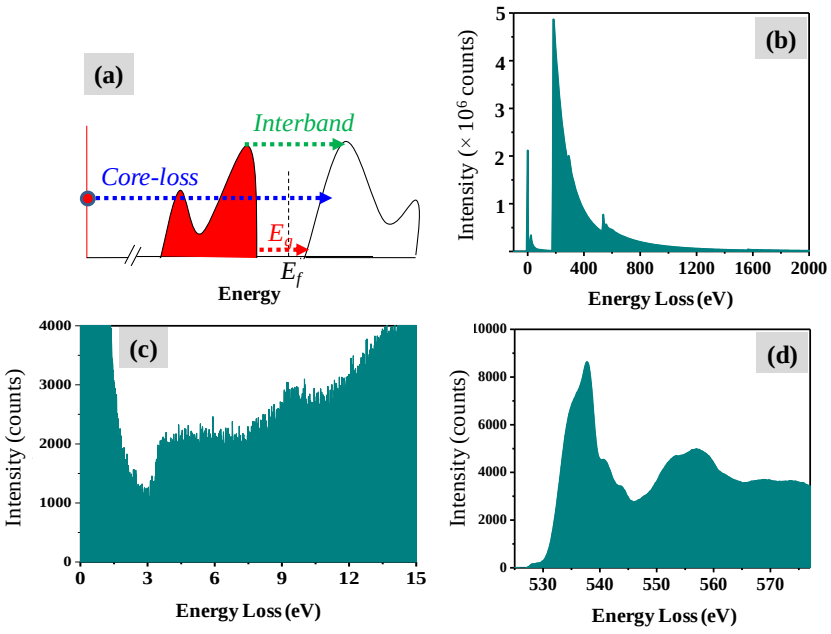

Figure 2.4 (a) Schematic energy level diagram of absorption phenomena in EELS showing various electronic transitions like band gap, inter-band and core-loss absorption. (b) Spectra displayed till 2000 eV for Al_2O_3. The intensity is blown up by × 350 times after 178 eV to highlight fine features. (c) EELS in the low-loss region and (d) core loss EELS for O K from ZnO.

The XAS mainly provides information from near the surface of the materials and energy loss over a wide range can be achieved with brilliant signal; on the other side, EELS contains information from the bulk of the sample and both energy and momentum are transferred during inelastic events with un-contending superior spatial resolution at individual atom. For a detailed description of various atomic absorption processes and associated techniques based on EELS can be found in Ref. 11. However the conventional TEM provides an energy resolution of 0.7 eV (the full width at half maxima) with Schottky field emission gun, which can be improved further to 0.3 eV by using a cold field emission source for EELS experiment. To overcome form this poor energy resolution for the low loss signal and fine feature of the core loss absorption spectroscopy, we need a monochromated electron source for acquisition of spectra with high energy resolution and subsequent extraction and interpolation of the information, which is called as high resolution electron energy loss spectroscopy (HR-EELS).

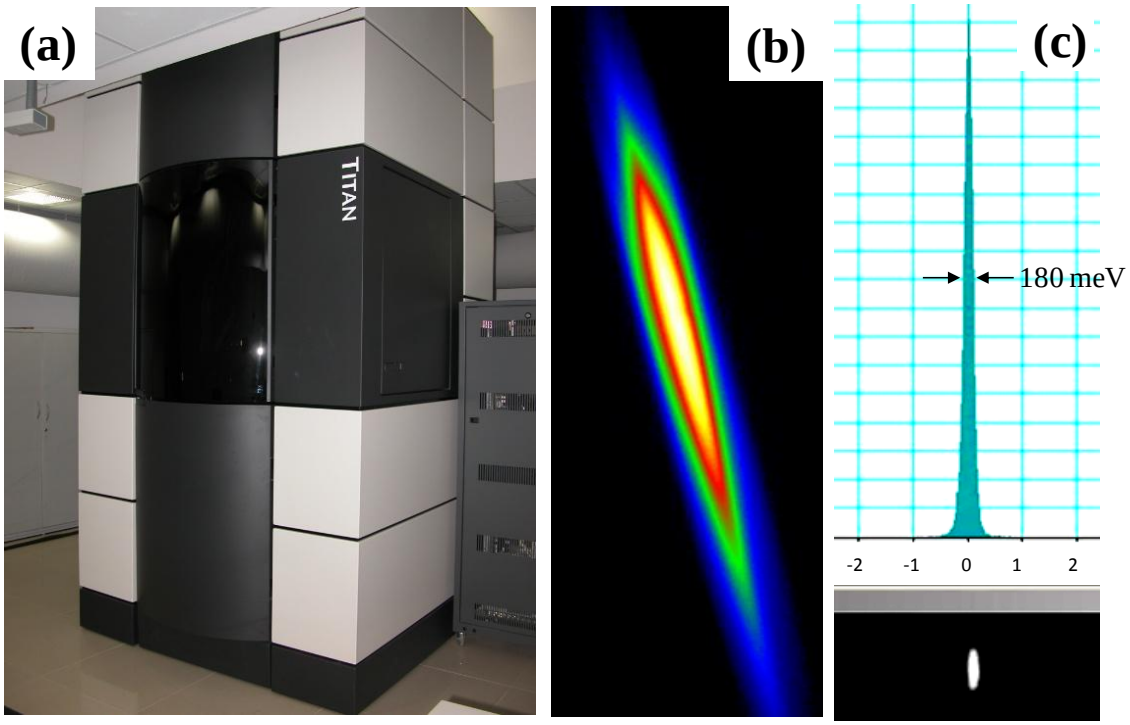

Figure 2.5 (a) FEI TITAN^{3TM} 80-300 kV double aberration corrected transmission electron microscope (b) Monochromated beam after mono-excitation to a value of 1.8. (c) Zero loss peaks after monochromatization gives FWHM of 0.18 eV which is a measure of the energy resolution.

For HR-EELS experiments in FEI TITAN^{3TM} 80-300 kV TEM is equipped with a 'single Wien filter' gun monochromator [16].With the availability of gun monochromator in FEI TITAN^{3TM} 80-300 kV TEM, it is now possible to record electron energy loss spectra with high energy resolution i.e. better than 0.18 eV for the low loss spectra (relevant for band gap information) and ~ 0.25 eV for the near edge structure (this compromise with resolution is at the cost of signal for higher energy loss events). The principle of gun monochromator based on single wien filter which act as a lens that has constant electric and magnetic field perpendicular to each other and perpendicular to the optic axis [16]. The dispersion happens due to applied electric (electric force = $-eE$, e is the electronic charge; E is the electric field) and magnetic field (magnetic force = $-evB$, v is the velocity of electron; B is the magnetic field) experienced by incident electron, which disperses electron beam depending on its energy spread. The centre part of the probe is highly monochromatic, having High electron beam currents and highest resolution better than 0.18 eV as measured from the full width half maxima (FWHM) of the zero loss peak under suitable experimental condition.

With the development of electron monochromators, low-loss EELS have now become a powerful tool for measuring optical absorption spectra at nano and atomic scale. We have used this technique to measure local band gap variation in Li:ZnO as well as for the ZnO:Te thin films. We have calculated local band gaps from TEM samples by Kramers – Kronig analysis [17] of low loss region of EELS (Electron energy loss spectroscopy) spectra. Kramers – Kronig analysis shows the energy related part of the real and imaginary part of the dielectric function of the specimen to be calculated from low loss single scattering distribution. The real and imaginary part of the dielectric function offers a complete description of the electronic and optical properties of the specimen. In this process we have removed zero loss peak of low loss region of EELS spectra. Then the plural scattering is removed by Fourier – log deconvolution process. We have taken the collection semi angle and refractive index as 1.316 mrad and 2.00 (refractive index of ZnO). The band gaps of the sample are also calculated by DFT which will be discussed in theoretical calculation section. Li and Te position in the ZnO lattice was determined by ELNES. Details of which are described in the respective sections. Our developed techniques demonstrate the power of HREELS as a nanoscale optical absorption tool where no other alternative exists in term of simultaneous imaging and spectroscopy at the atomic and nanometre length scale [18-20].

2.4 Others techniques and characterization tools

X-ray measurements for characterizing epitaxial quality of the films were done in a Bruker D8 DISCOVER high resolution diffractometer with four-bounce Ge (022) monochromator. Cathodoluminescence (CL) spectra were collected using Gatan mono CL (serial mode) installed in a FEI quanta 3D FE-SEM at 20 keV electron beam energy. All the spectra have been collected with Peltier cooled (-25 ºC) photo multiplier tube (PMT) with a step of 1 nm and accusation time of 0.6 sec/step. Carrier concentration and mobility at room temperature were calculated from Hall measurements performed with the physical property measurement system (PPMS, Quantum Design).

2.5 Density functional theory

Several methods like Hartree-Frok method, Green's function etc were developed to tackle the many-body Schrodinger equation in terms of wave function, but density functional theory (DFT) deals with electron charge density and gives ground state energy of the system accurately. This was a landmark achievement in the field of computational science. It represents a complete reformulation of the Schrödinger equation in terms of electron charge density. The many body N-electron wave function is replaced by electron density in DFT. One of the main advantage is it can limit the number of dimensions. The number of dimension is 3 for DFT for N-electron system compared to 3N for a wave function. In DFT electron density becomes key variable which was earlier just an observable of the wave function. DFT is based on Hohenberg-Kohn theorems [21]. It states that from the knowledge of ground state density, its ground state wave function can be calculated i.e. one to one correspondence between the ground state electron density of many-electron system and the external potential, which is a functional of electron density. In the second part of the theorem we find energy is minimized with respect to the density, and the ground state density and energy have been obtained. In 1965 Kohn-Sham approach [22] came replacing the difficult interacting many-body system. The Kohn-Sham approach rests on two assumptions. In the first assumption, the exact ground state density can be represented by the ground state density of an auxiliary system of non-interacting particles. In the second assumption, the auxiliary Hamiltonian can be chosen to have the usual kinetic energy and an effective local potential acting on the particle at a point. The Kohn-Sham approach is to replace the Hohenberg – Kohn approach for the ground state energy functional. In this assumption the main important

concept was exchange-correlation potential. The exchange-correlation energy is sum of exchange energy and correlation energy. Exchange energy is the difference between the real kinetic energy and that of a system of non-interacting electrons and the correlation energy is the difference between the real interaction energy between the electron and the Hartree energy. Functional often perform better for the sum then for the separate energy. The exact formulation of the exchange-correlation functional is not known so this can be approximated in several ways. The most commonly used approaches are local density approximation (LDA) [21] and the generalized gradient approximation (GGA) [23, 24]. In LDA, the exchange correlation energy density is the same as that of a homogeneous electron gas of that density, on the other hand, in GGA, with consideration of the exchange correlation energy density as a function of both, the density and the gradient of density makes an improvement over LDA [25, 26].

In this calculation we have used WIEN2k package for DFT. WIEN2k is based on full potential instead of pseudo potential approximation where most of the properties of a system are determined by its valance electron with little or no contribution from its core electron. This package use full potential. The linearized augmented plane wave (LAPW) method is one of the most perfect ways to calculate the electronic structure in crystal. The LAPW method use local spin density approximation (LASD) and generalized gradient approximation (GGA). The LAPW method solves the Kohn-Sham equation for the ground state energy, eigen values and ground state electron density of many electron system by using a special basis set. The LAPW method is one of the most accurate methods for calculating electronic structure. We have used modified Becke-Johnson potential (mBJLDA) [27, 28] which is an orbital independent exchange correlation potential to calculate accurate band gap of semiconductors. This is a first semi local potential which can compete in accuracy with expensive hybrid and GW method. The agreement of mBJLDA is very good for wide range of solid materials e.g. wide band gap semiconductors, sp semiconductors, strongly correlated 3D transition metal oxides. The semi local exchange potential recover the local density approximation (LDA) for a constant electron density and mimics very well the orbital dependent potentials leading a calculation which are barely more expensive than LDA calculations. This potential is cheap as LDA and GGA and thus can be used to large system in an efficient way which can't be possible for hybrid or GW method.

In our calculation, we have done non spin polarized calculation to study electronic properties of ZnO system with dopants. The Generalized gradient approximation (GGA) was

used with Perdew-Bruke-Ernzenhof (PBE) functional for optimization of lattice parameter. The optimized lattice parameters of ZnO were a = 3.2973 A and c = 5.2824 A. We have used 12x12x6 k-mesh for ZnO unit cell and it was reduced proportionally to the number of unit cell in each direction for the super cell calculation. We have used modified Becke-Johnson potential (mBJLDA) to calculate band gaps for different systems. We have calculated cohesive energy which is the energy required to break the atoms of solid into isolated atomic species using the equation 2a.

$$\mathbf{E_{coh} = E_{solid} - \sum_A E_A^{isolated}} \quad \textbf{..... (2a)}$$

Where A stands for the different atoms that constitute the solid. E_{solid} is the total energy of the solid and $E_A^{isolated}$ is the energy of individual atom of different species in zero force state in the solid.

We have used WIEN2k based density functional theory to study electronic structures of both ZnO and transition metal dichalcogenides.

2.6 FEFF code

The FEFF program allows both electron and X-ray absorption spectroscopy measurement for any arbitrary system, and their interpretation in terms of local electronic and geometrical structure [29, 30]. FEFF is an *ab-initio* self-consistent real space multiple scattering (RSMS) for clusters of atom. It includes polarization dependence, core hole effect, local field correction based on self-consistent and spherical muffin-tin scattering potentials. This is based on real space relativistic Green's function formalism with no symmetry requirements. It is an all-electron calculation process. FEFF includes the vibration effects in term of correlated Debye-Waller factors [31]. The FEFF calculation allows a quantitative interpretation of EELS [32] based on self-consistent-energy (SCF) calculation of both excited and ground state electronic structure along with electronic density of states and charge transfer. A FEFF calculation is usually a sequence of six steps corresponding to different program modules. The first step belongs to the calculation of the potential self-consistently using an automated self-consistent-field procedure. In this step the absolute edge energies are calculated, typically to within a few electron volts. In the second step we calculate the scattering phase shift, dipole matrix elements, and angular-momentum projected density of states (LDOS). The third step belongs to the calculation of full multiple scattering EELS for a specified cluster of atoms around the absorbing atom. In the fourth module, the leading

multiple scattering paths for the system are numerated. In module five the calculation related to effective scattering amplitudes for that path are done. Finally in sixth step the parameters from one or more path are combined to calculate EELS spectra. FEFF is one of the master keys to study core level spectroscopy of materials which contains excited state information.

The lattice parameter of ZnO used in FEFF was optimized by GGA in WIEN2k. The Hedin-Lundquist (HL) exchange correlation potential was used for the calculation and the core hole was treated according to the "final state rule". A spherical cluster of 10 Å radius was used for the calculations with absorbing at the centre. In chapter four, two different cases were considered, i.e. (i) Li_{Zn} and (ii) Li_i as the absorbing atom for Li K edge. In chapter three, we have considered three different cases (i) Te at O site, (ii) Te at Zn site, and (iii) Te at interstitial (octahedral) site. In that case we have calculated Te N_4, N_5 and Te M_4, M_5 edge to compare with experimental ELNES and EXELFS respectively.

2.7 Bibliography

[1] D. B. Chrisey, G. K. Hubler, Pulsed Laser Deposition of Thin Films (New York: John Wiley &Sons), (1994).

[2] D. H. Lowndes, D. B. Geohegan, A. A. Puretzky, D. P. Norton, C. M. Rouleau, Science **273**, 898 (1996).

[3] P. R. Willmott, J. R. Huber, Rev. Mod. Phys. **72**, 315 (2000).

[4] P. R. Willmott, Prog. Surf. Sci. **76**, 163 (2004).

[5] H. N. Lee, H. M. Christen, M. F. Chisholm, C. M. Rouleau and D. H. Lowndes, Nature **433**, 395 (2005).

[6] H. Yamada, M. Kawasaki, Y. Ogawa, Y. Tokura, Appl. Phys. Lett. **81**, 4793 (2002).

[7] H. M. Smith, A. F. Turner Appl. Opt. **4**, 147 (1965).

[8] D. Dijkkamp, T. Venkatesan, X. D. Wu, S. A. Shaheen, N. Jisrawi, Y. H. Min-Lee, W. L. McLean, M. Croft, Appl. Phys. Lett. **51**, 619 (1987).

[9] R. K. Singh and J. Narayan Phys. Rev. B **41**, 8843, (1990).

[10] D. B. Williams, C. B. Carter, Transmission Electron Microscopy; A Text Book for Materials Science (Springer Science + Business Media LLC, 2009).

[11] R. F. Egerton, Electron Energy Loss Spectroscopy in the Electron Microscope (2nd edn. Plenum, New York, 1996).

[12] P. W. Hawkes, J. C. Spence, Science of Microscopy (Springer Science + Business Media LLC, 2007).

[13] S. J. Pennycook, P. D. Nellist, Scanning Transmission Electron Microscopy (Springer Science + Business Media LLC, 2011).

[14] R. Brydson, Electron Energy Loss Spectroscopy (Garland Science, first edition, 2001).

[15] R. Brydson, Aberration Corrected Analytical Transmission Electron Microscopy, (John Wiley & Sons, Ltd. 2011).

[16] P. C. Tiemeijer, J. H. A. van Lin, A. F. de Jong, Microsc. Microanal. **7**, 1130 (2001).

[17] J. Tauc, Mat. Res. Bulletin **3**, 37 (1968).

[18] K. Dileep, B. Loukya, N. Pachauri, A. Gupta, R. Datta, J. Appl. Phys. **116**, 103505 (2014).

[19] K. Dileep, B. Loukya, P. Silwal, A. Gupta, R. Datta, J. Phys. D: Appl. Phys. **47**, 405001 (2014).

[20] K. Dileep, R. Sahu, S. Sarkar, S. C. Peter, R. Datta, J. Appl. Phys. **119**, 114309 (2016).

[21] P. Hohenberg, W. Kohn, Phys. Rev. Lett. **97**, 135901 (2006).

[22] W.Kohn, L. J. Sham, Phys. Rev. A **140**, 1133 (1965).

[23] J. P. Perdew, K. Burke, M. Ernzerhof, Phys. Rev. Lett. **77**, 3865 (1996).

[24] J. P. Perdew, P. Ziesche, H. Eschrig, Akademie-Verlag, Berlin 11 (1991).

[25] B. Hammer, M. Scheffler, K. W. Jacobsen, J. K. Nørskov, Phys. ReV. Lett. **73**, 1400 (1994).

[26] E. Penev, P. Kratzer, M. Scheffeler, Journal of Chemical Physics 110, (1999).

[27] F. Tran and P. Blaha, Phys. Rev. Lett. **102**, 226401 (2009).

[28] D. Koller, F. Tran, P. Blaha, Phys. Rev. B **85**, 155109 (2012).

[29] J. J. Rehr, J. J. Kas, F. D. Vila, M. P. Prange, K. Jorissen, Phys. Chem. Chem. Phys. **12**, 5503-5513 (2010).

[30] J. J. Rehr, J. J. Kas, M. P. Prange, A. P. Sorini, Y. Takimoto, F. D. Vila, Comptes Rendus Physique **10(6)**, 548-559 (2009).

[31] K. Jorissen, J. J. Rehr, J. Verbeeck, Phys. Rev. B **81**, 155108 (2010).

[32] F. D. Vila, J. J. Rehe, H. H. Rossner, H. J. Krappe, Phys. Rev. B **76**, 014301 (2007).

Chapter III

Structural and optical properties of epitaxial ZnO:Te thin films grown by pulsed laser deposition

This chapter provides investigation of the Te atom incorporation, solubility, structural features and the corresponding optical property of epitaxial ZnO:Te thin film grown on c-plane sapphire by pulsed laser deposition. Incorporation of Te at the oxygen (Te_O) or zinc (Te_{Zn}) site can be controlled through the deposition scheme to transfer Te during the film growth. Experimentally, the decrease in band gap is found to be strongly dependent on Te percentage for Te_O compared to Te_{Zn}. Emission at 3eV for Te_{Zn}, irrespective of Te content is explained by first principle calculation considering Zn vacancy in the lattice. An experimental band bowing parameter of ~7 eV is obtained for Te_O and in agreement with mBJLDA based theoretical calculation. The physical insight into the nature of band bowing is elucidated.

This work has been published in Journal of Crystal Growth, ***410,*** *69-76 (2015) and physica status solidi (b),* ***252 (8),*** *1743-1748 (2015).*

3.1 Introduction

The application of ZnO based bipolar devices is still finding obstacles due to difficulty in *p*-type doping, its stability and reproducibility issues[1-4].Among various approaches, doping ZnO with chalcogens (e.g., S, Te, Se) at the oxygen site has been proposed to overcome the *p*-doping difficulty through raising the valence band of ZnO with respect to the vacuum level[1].This will in turn help in lowering the ionization energy of acceptor dopants and shifts the valence band towards the Fermi level stabilization energy. However, incorporation of chalcogens in ZnO lattice and associated optical band gap need to be explored in details first towards this effort. We already have reported the solubility and band gap bowing in case of ZnO alloyed with S [4, 5].A maximum S of 17 at.% can be incorporated in ZnO in epitaxial film form and a band gap of 3.17 eV is obtained. However, desired amount of S is close 30 at.% for sufficient band bowing for the acceptor atom ionization beyond the compensation level which could not be achieved due to phase separation. On the other hand, requirement in percentage of Te doping may be less (within few percentages) as the atomic size mismatch with O is large (for the Te at the O site) and raises the valence band significantly upwards compared to S [6]. Few reports exist in the literature on the Te doped ZnO[7-14]. Among these reports, MBE grown films were shown to have Te at both the lattice sites and upon annealing switches to only O site as determined by X-ray photo emission spectroscopy (XPS)[10]. In the present report, we have attempted to grow ZnO:Te by pulsed laser deposition (PLD) on *c*-plane sapphire and investigated the experimental conditions required for Te incorporation at both the oxygen and zinc site, its solubility and corresponding epitaxial quality and optical band gap. We have found that the Te incorporation can be controlled through the scheme to transfer Te during PLD growth and the solubility depends strongly on the deposition temperature. We have obtained maximum Te of ~4 at.% at 400 °C with the film remained to be epitaxial as confirmed by both X-ray diffraction and transmission electron microscopy and attempt to incorporate more Te either at the same temperature or at reduced temperature resulted in formation of amorphous films. Optical band gap is decreased to 2.8 eV for 4 at.% of Te and for amorphous film emission peak is broad with the presence of multiple peaks near the longer wavelength side of the spectra as measured by cathodoluminescence (CL). However, incorporation of Li with the ZnO:Te (1 at.% grown at 400 °C) film and subsequent annealing did not result in enough carries to be measured their type in anordinary Hall system rather emission at 2.11/2.37 eV has become intense. For Te at the Zn site we obtained maximum of 7 at.% Te (with phase

separation) and band gap reduction is not significant at this composition i.e. ~3.01 eV, and is composition independent compared to Te at the O site. A band bowing parameter of ~7 eV is obtained for Te in the O site and matches closely with the theoretical band gap calculation using mBJLDA potential within the WIEN2k code [15]. The physical nature of the band bowing upon Te substitution in both the sites is discussed with the help of band structure and density of states (DOS) calculation.We present details of the results below.

3.2 Experimental method

We have attempted to incorporate Te in ZnO film in two different ways; 1) from a target pellet containing ZnO and TeO_2 or ZnTe mixed together and 2) ablating individual ZnO and ZnTe pellets with a certain frequency during deposition of the film. The first approach was accomplished by using two different target pellets, one mixing between ZnO and TeO_2 and another one between ZnO and ZnTe and sintering the cold pressed pellets for four hours at 800 °C. This method was not successful in incorporating Te in the O site rather Te was incorporated in the Zn site. Powder X-ray pattern confirmed the formation of Zn_3TeO_6 as dominating phase in the pellets (figure 3.2 (a)). Mixing ZnO with ZnTe also did not work out retaining Te as anion as after sintering this mixture $Zn_3Te_3O_6$ phase was observed to form (figure 3.2 (a)) and resulted in Te substituting the Zn site in the thin film. In order to overcome this problem and to incorporate Te at the O site, we have sintered ZnTe pellet separately under vacuum (at 10^{-5}Torr pressure at 500 °C in order to avoid oxidation of ZnTe) and ablate alternately ZnO and ZnTe pellets at different frequencies, i.e. 19:1, 9:1, 5:1. 4:1, 3:1, and 2:2, the first digit being the number of shots off ZnO target and second one off ZnTe target in order to gain control over Te concentration during film deposition. We have used KrFexcimer laser with wavelength ~248 nm and energy fluence of ~1.5 Jcm^{-2} to ablate the target pellets. The distance between the pellet and substrate was set at ~ 5 cm. The growth scheme was followed by three step growth already reported in Ref. 4, 5, and 16. For Te_O films, growth was carried out under both low (~10^{-5}Torr) and high (~10^{-1}Torr) oxygen partial pressure. Low p_{O2} helps in more Te incorporation in the film e.g., 5:1 films gives Te concentration of 1.7 and 1% Te for *n*-type and resistive type films respectively. For Te_{Zn} case, higher p_{O2} has been used (~10^{-1}Torr) to minimize the chances for Te occupying the O sites. We have used epitaxial ZnO as buffer layer (~ 50 nm thickness) for the ZnO:Te growth which helps in epitaxial film with high Te content compared to films without buffer layer.

For the growth of ZnO:Te, various temperatures were attempted and a temperature at 400 °C was found to be optimum in order to obtain both epitaxial film as well as higher incorporation of Te at the O site. At temperature above 400 °C, Te content decreases significantly as in the case of S and growth at below 400 °C temperatures (i.e. 300 °C and 200 °C) amorphous films were formed (though Te content is high).

3.3 Theoretical calculation

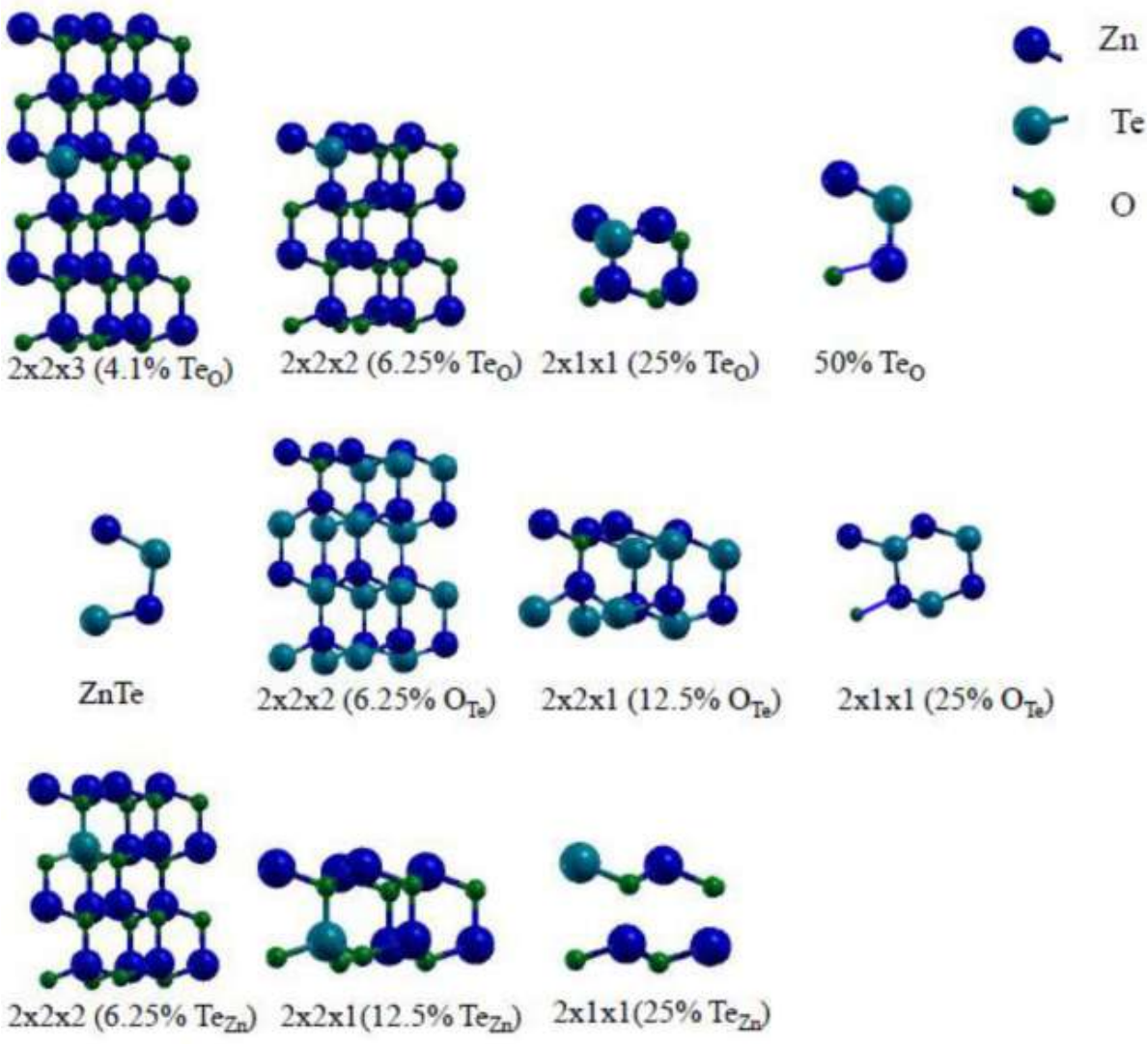

Figure 3.1 Schematic representations of DFT model structures.

The electronic structure of ZnO with different percentage of Te at two different sites in ZnO lattice was calculated using density functional theory based WIEN2k code. Besides, calculation was performed for ZnTe with O substitution at Te site in order to evaluate band

gap data for this end of the composition. Details of various configurations considered for calculations are given in figure 3.1. We have used generalized gradient approximation (GGA) with Perdew-Burke-Ernzenhof (PBE) functional for optimization of lattice parameters and minimization of force. The optimized lattice parameters of ZnO and ZnTe are *a* = 3.2973 & 4.3797 Å and *c* = 5.2824 & 7.0968 Å, respectively. A 12x12x6 k mesh was used for ZnO unit cell and was reduced proportionally to the number of unit cell in each direction for the super cell calculations. For calculating band gaps, we have used modified Becke-Johnson potential (mBJLDA) according to P-semiconductor scheme, which yields accurate band gap values and have already been tested for ZnO based alloys [4, 18].

3.4 Results and Discussion

3.4.1 Epitaxial Growth: XRD & HRTEM

Figure 3.2(b) shows the X-ray data for the four films (i.e. 19:1, 9:1, 5:1 and 4:1) grown at 400 °C. The films color is light reddish brown in this case which indicates that the Te has replaced O site and this is further confirmed by Te $M_{4,5}$ EXELFS spectra (figure 3.6, see later section for description). Peaks corresponding to only (0002) and (0004) of ZnO and (0006) of Al_2O_3 are marked in the X-ray data confirming the epitaxial growth of the films on c-plane sapphire. The '*c*' lattice parameter has been calculated from the symmetric scans and an increase in *c* lattice parameter can be observed with the increased Te incorporation in ZnO (Table 3.1 & figure 3.2).

Samples	at% of Te by EDS	c (Å) by X-ray	0 0 0 2 Rocking curve width (FWHM)
1:19 Te_O	1.27	5.198	–
1:9 Te_O	1.58	5.2034	0.786°
1:5 Te_O	1.68	52178	1.311°
1:4 Te_O	4.04	5.2335	1.351°
1:3 Te_O	17.36	–	–
2:2 Te_O	28.6	–	–
1:4 at 300 °C	14.11	–	–
1:4 at 200 °C	14.46	–	–
Te_{Zn} (5% targeted)	1.41	5.2125	–
Te_{Zn} (10% targeted)	3.38	5.2328	–
Te_{Zn} (15% targeted)	6.37	5.1995	–
Te_{Zn} (20% targeted)	7.13	5.2182	–

Table 3.1 EDS composition & 'c' parameters of ZnO:Te.

.

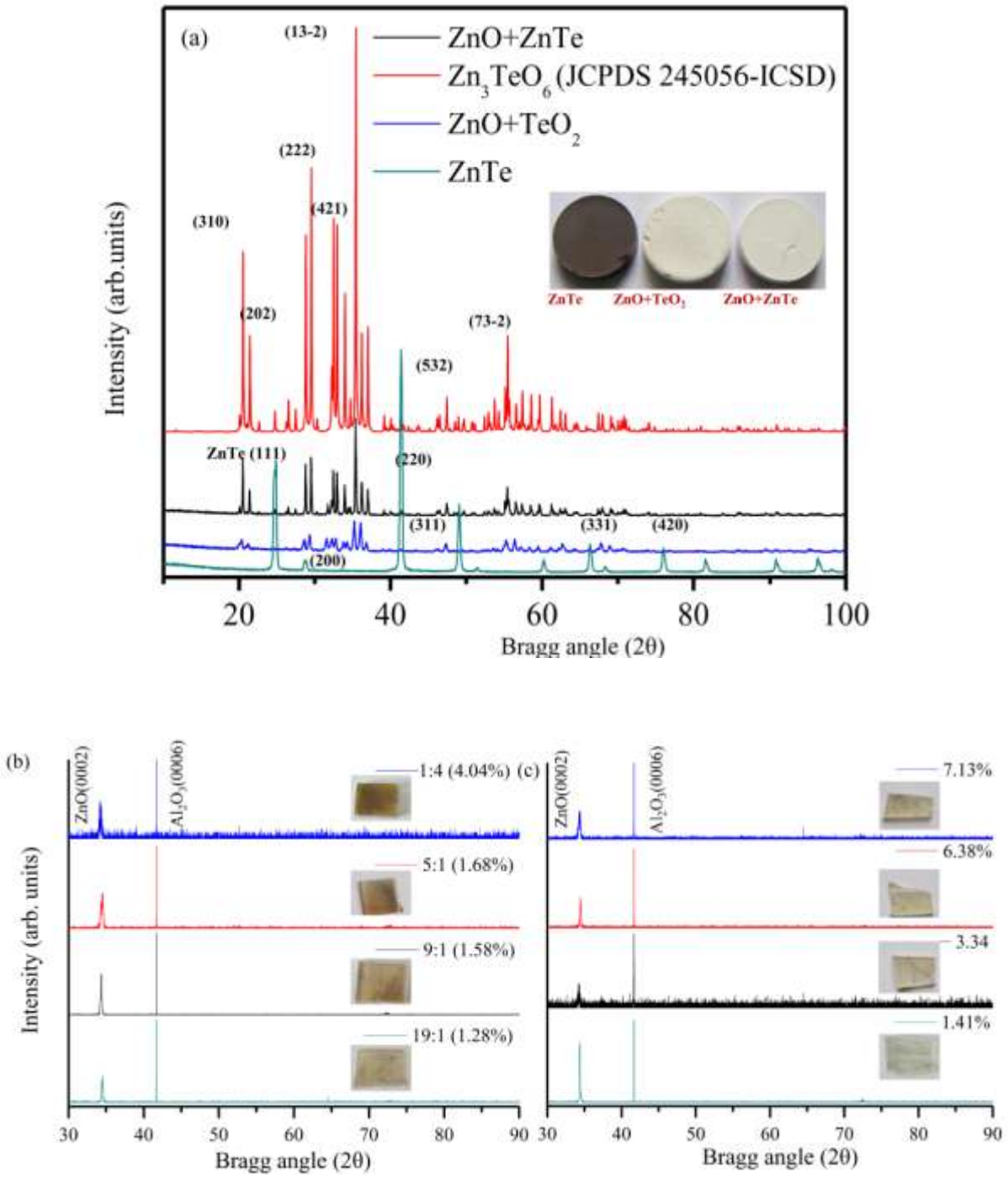

Figure 3.2 (a) Powder XRD data from target pellets after sintering which was composed of ZnTe, ZnO+TeO_2, ZnO+ZnTe as starting material. The peaks resemble with Zn_3TeO_6 phase (red model peaks) for the latter two pellets.(b) and (c) thin film X-ray diffraction for Te_O and Te_{Zn}.

The thickness of the films is in the range of 400-500 nm and thickness of the ZnO buffer layer is ~ 50-80 nm. From the TEM bright field images presence of threading dislocations

can be observed which is originated due to the large lattice mismatch between film and substrate (~ 16% for '*c*' plane sapphire). From the EDX quantification it can be seen that there is a gradual increase in Te concentration from 1.27 to 4 at % as the number of shots on ZnO reduced from 19 to 4 for every ZnTe shot (Table 3.1).

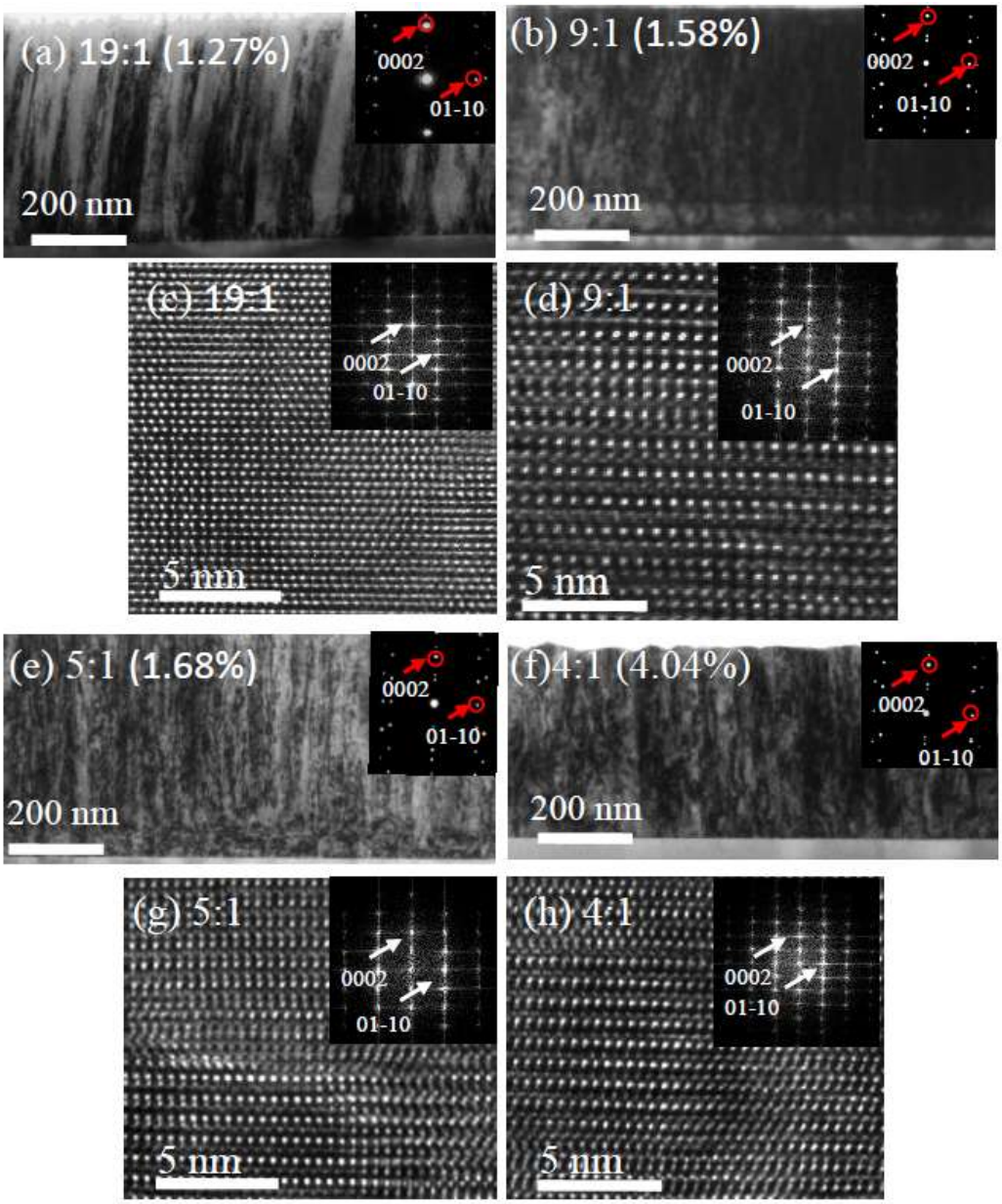

Figure 3.3 (a), (b), (e) and (f) are TEM bright field images and (c), (d), (g) and (h) are high resolution TEM images of Te_O films grown with various ZnO and ZnTe ablation frequency. Frequencies and Te concentrations obtained by EDX are mentioned in the respective figures. Spot patterns confirm the epitaxial nature of the thin film.

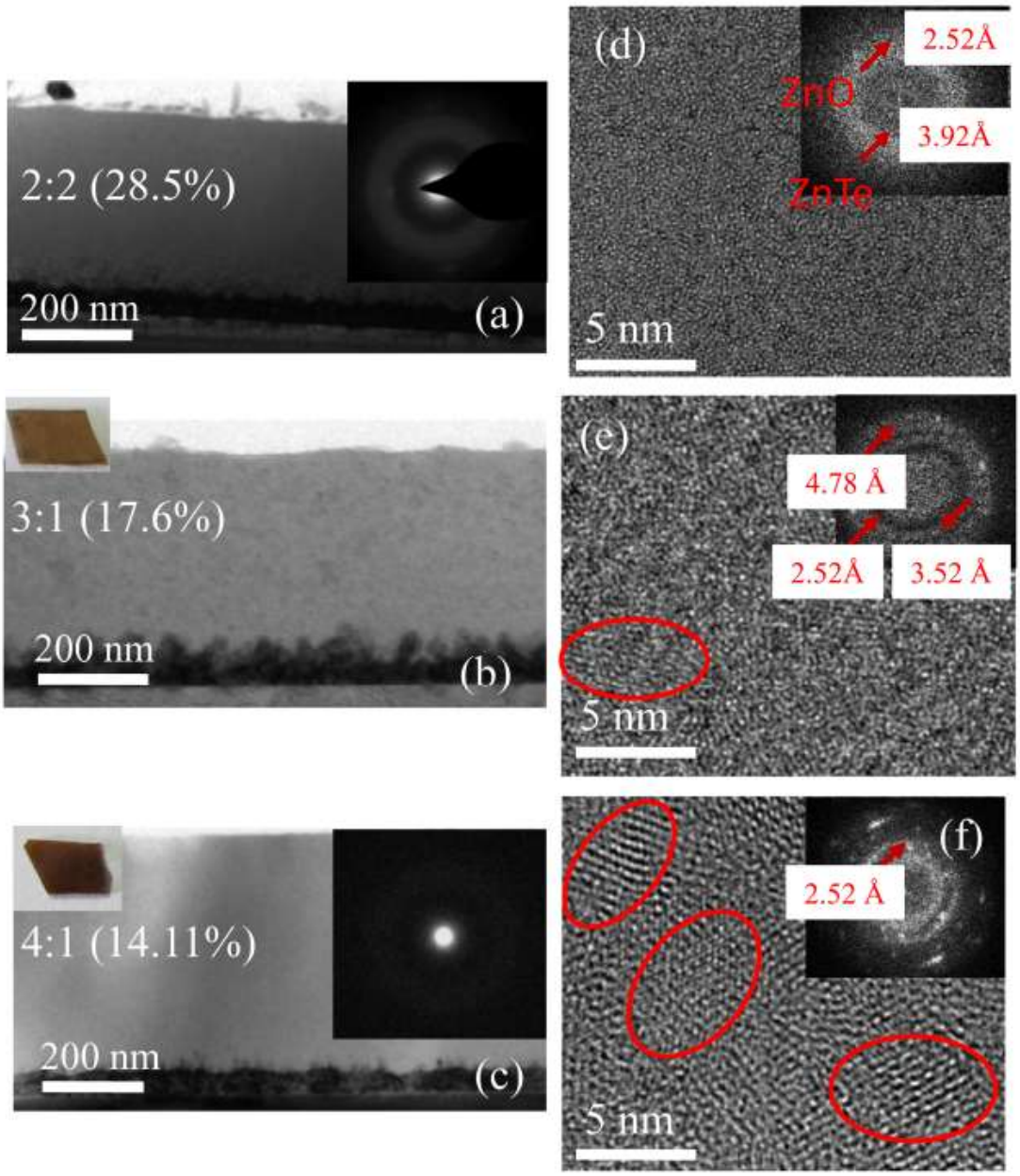

Figure 3.4 (a)-(c) TEM bright field images and (d)-(f) high resolution TEM images from higher Te content films grown using alternate ablation of separate ZnO and ZnTe targets. Formation of amorphous layers with small crystallites can be observed.

However, further decrease in ZnO shots or increase in ZnTe shots at the same temperature (e.g., 3:1 and 2:2) as well as lowering the growth temperature from 400 °C to 300 or 200 °C turns the film amorphous with significant increase in Te content to around 17.6 % for 3:1 (400 °C), 14% for 4:1 (both at 200 and 300 °C) and increasesfurther to 28.5 % for 2:2 (400°C) films (Table 3.1). Thus it can be anticipated that with further increasing the

number of Te shots to every ZnO shots will increase the Te content in the amorphous films and not explored in the present study due to the loss in crystallinity in the film. Figure 3.4 shows TEM cross sectional bright field and HRTEM images from these films showing presence of amorphous layer where indication of such amorphous layer formation cannot be obtained by X-ray measurement which gives peaks corresponding to ZnO buffer layer only. The ZnO buffer layer can be seen clearly in these cases and marked in the images. Further investigation by HRTEM images of amorphous layers it is found that they are not completely amorphous (figure 3.4). Small crystallites are observed to be present along with amorphous matrix for 4:1 and 3:1 films. The crystallites have average '*c*' lattice parameter of 5.04 Å, which is close to ZnO. For 2:2, the film is completely amorphous (figure 3.4). Such conducting amorphous layer can be of interest in many different applications e.g., in nonlinear optical material as a reverse saturation absorption based optical limiter[17]

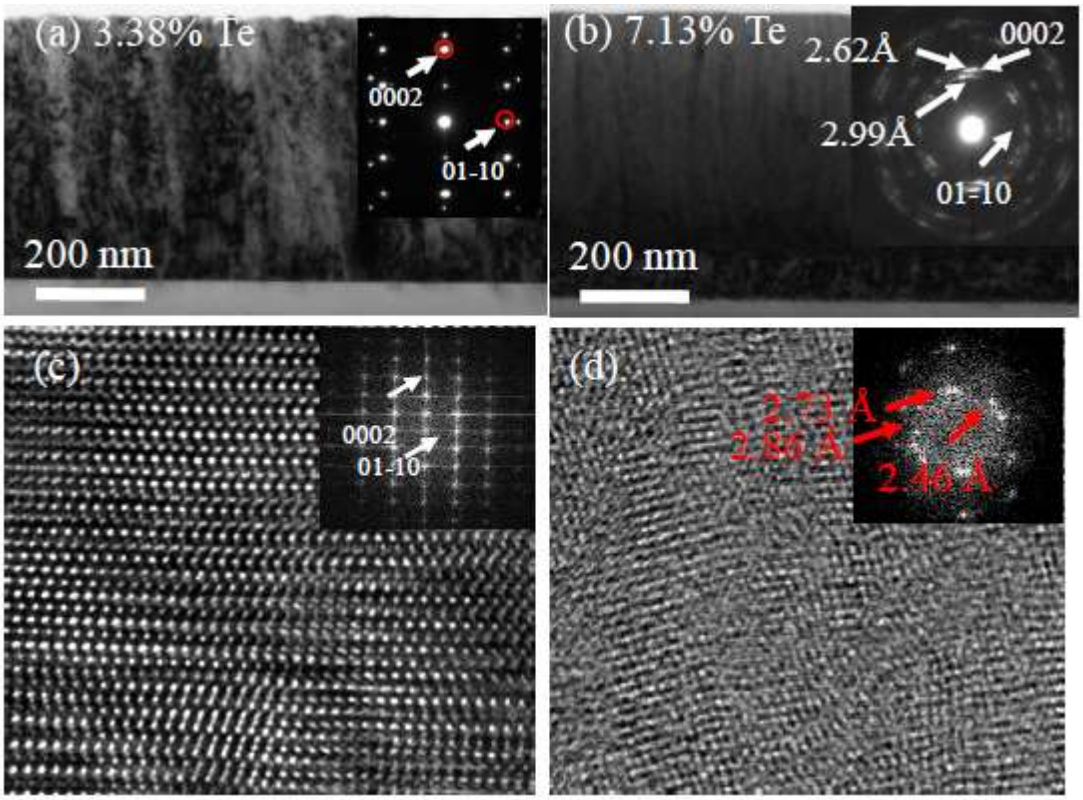

Figure 3.5 (a) and (b) TEM BF and (c) and (d) HRTEM images from Te_{Zn} films for two different Te compositions. 3.38% Te film shows slight tilt and 7.13% Te film shows tilt along with phase separation.

In the case of transparent ZnO:Te films, where Teis found to be in the Zn site (figure 3.6, see description for Te $M_{4,5}$ section). The film is epitaxial for 1.41 % but epitaxial with slight tilt for 3.38 at. % Te as marked in figure 3.5(a). The composition of Te was derived from both SEM & TEM-EDS. Films start showing significant tilt and twist along with two different phases (Te rich and poor) for higher Te contents i.e. 6.37 and 7.13 % (figure 3.5(b)).The diffraction pattern corresponding to two different phases are marked in figure3.5(b). These two phases are Te poor and Te rich with 'c' lattice parameter ~ 5.34 and 5.98 Å respectively. Figure 3.2(c) is the X-ray diffraction pattern from films with Te (1, 3, 6 and 7 at. %, though the Te content in the target was 5, 10, 15 and 20 at. %respectively). The '*c*' lattice parameter is observed to be increasing with Te concentration for the first two films i.e., 5.2125 Å and 5.2328 Å respectively, where films are epitaxial and single phase. For latter two films the signal is recorded only from the Te poor phase '*c'* parameters are 5.1995 Å and 5.2182 Å and no clear peaks are obtained from the high Te content phases.

3.4.2 Atomic position of Te in ZnO: EXELFS & FEFF

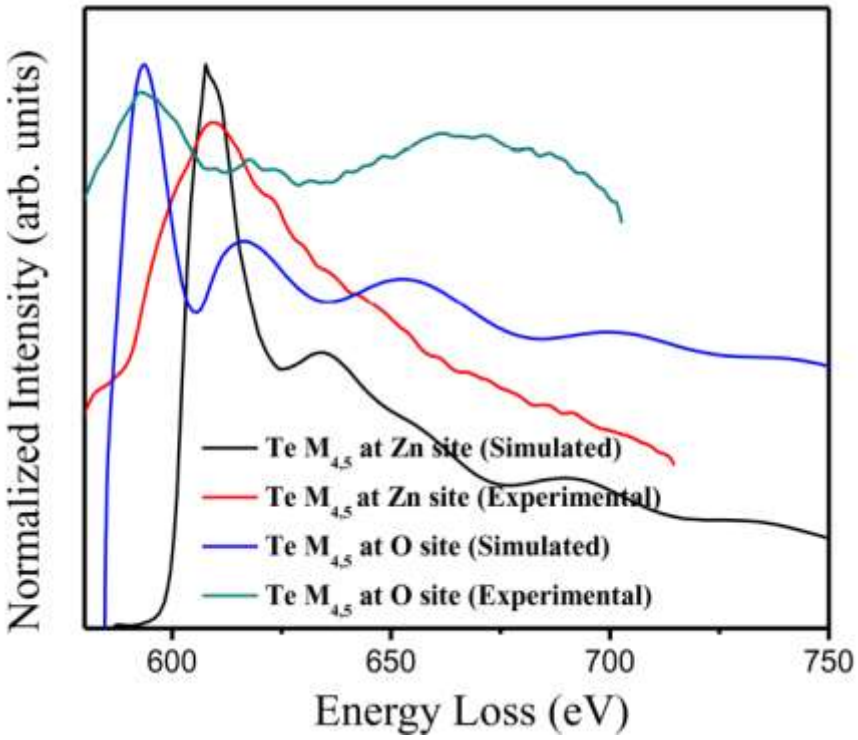

Figure 3.6Te $M_{4,5}$ EXELFS experimental and simulated spectra confirming the substitution of Te in O (for brown films), and Zn site (for transparent films), respectively.

Besides indication from the color of the film (figure 3.2, insets) i.e. reddish brown for Te in the O site and transparent for Te in the Zn site we have further confirmed this by Te $M_{4,5}$ EXELFS. Figure 3.6 is the Te $M_{4,5}$ EXELFS spectra along with FEFF 9.05 code based calculation of theoretical spectra plotted together for comparison. Experimental spectraclosely matches with the theoretical spectra and suggesting that for the brown film Te is in the O site and for transparent film it is in the Zn site.

3.4.3 Band gap: CL& EELS

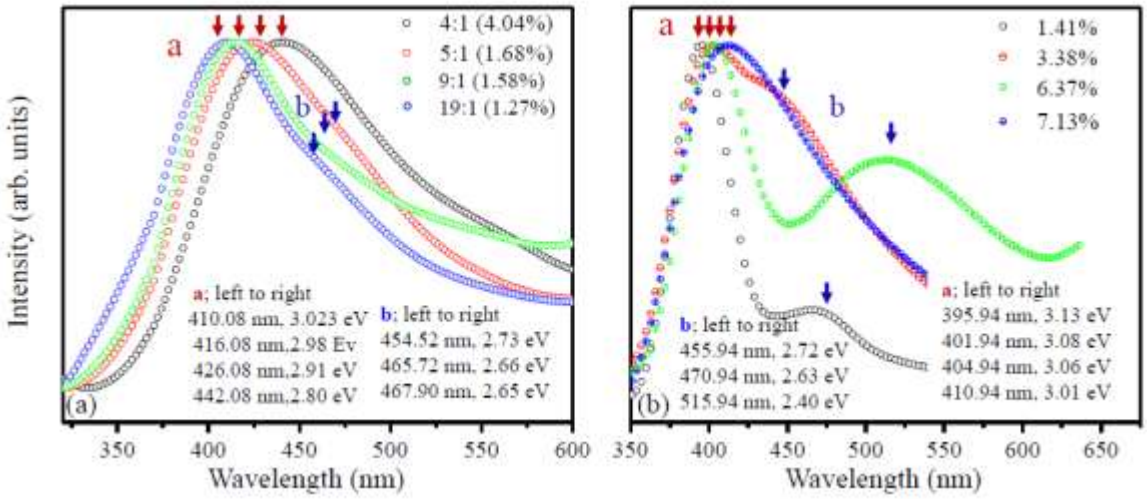

Figure 3.7 Experimental CL spectra of (a) Te_O and (b) Te_{Zn} films. Besides main emission peaks (marked with a), defects peaks are also observed (marked with b). Kindly see text for the probable origin of the defect peaks.

Figure 3.7(a) is the CL spectra showing emission peak (marked with red arrows and '*a*') is broad and band gap decrease from 3 eV to 2.8 eV for Te concentration of 1.27 % and 4.04 at.% respectively for the epitaxial thin film cases. A secondary peak (marked in the figure as '*b*' with blue arrows) is observed as shoulder in the all CL spectra at around 2.65 eV (467.90 nm) – 2.73 eV (454.52 nm). As the samples were grown under low oxygen partial pressure (~10^{-5}Torr), the second peaks could be due to oxygen vacancy defect (V_O) which was shown previously to give indirect band gap around the same value both by theory and experimentation [18].Figure 3.8 is a combination of both area and spot CL for Te_{Zn}.Slight variation in the peak positions may be due to the presence of Te in the lattice which modified

the defect level with respect to the host band gap. For higher Te content films (amorphous along with nano-crystallites and amorphous) band gap further shifts towards the longer wavelength starting from 2.75 eV down to 1.73 eV depending on the temperature and ablation condition of the growth. For the 3:1 film grown at 400 °C there is one intense and broad peak around 2.75 eV. For the 2:2 films grown at 400 °C multiple peaks are observed which starts at 2.64 eV and a second peak at 2.17 eV (figure 3.9(a)). For films where growth temperature was further lowered i.e. 4:1 film with two different growth temperatures, 300 °C and 200 °C, peaks shift further to the right starting at 2.01 eV to 1.73 eV. The multiple peaks at larger wavelength may be presence of amorphous layers with different Zn, Te and O content.

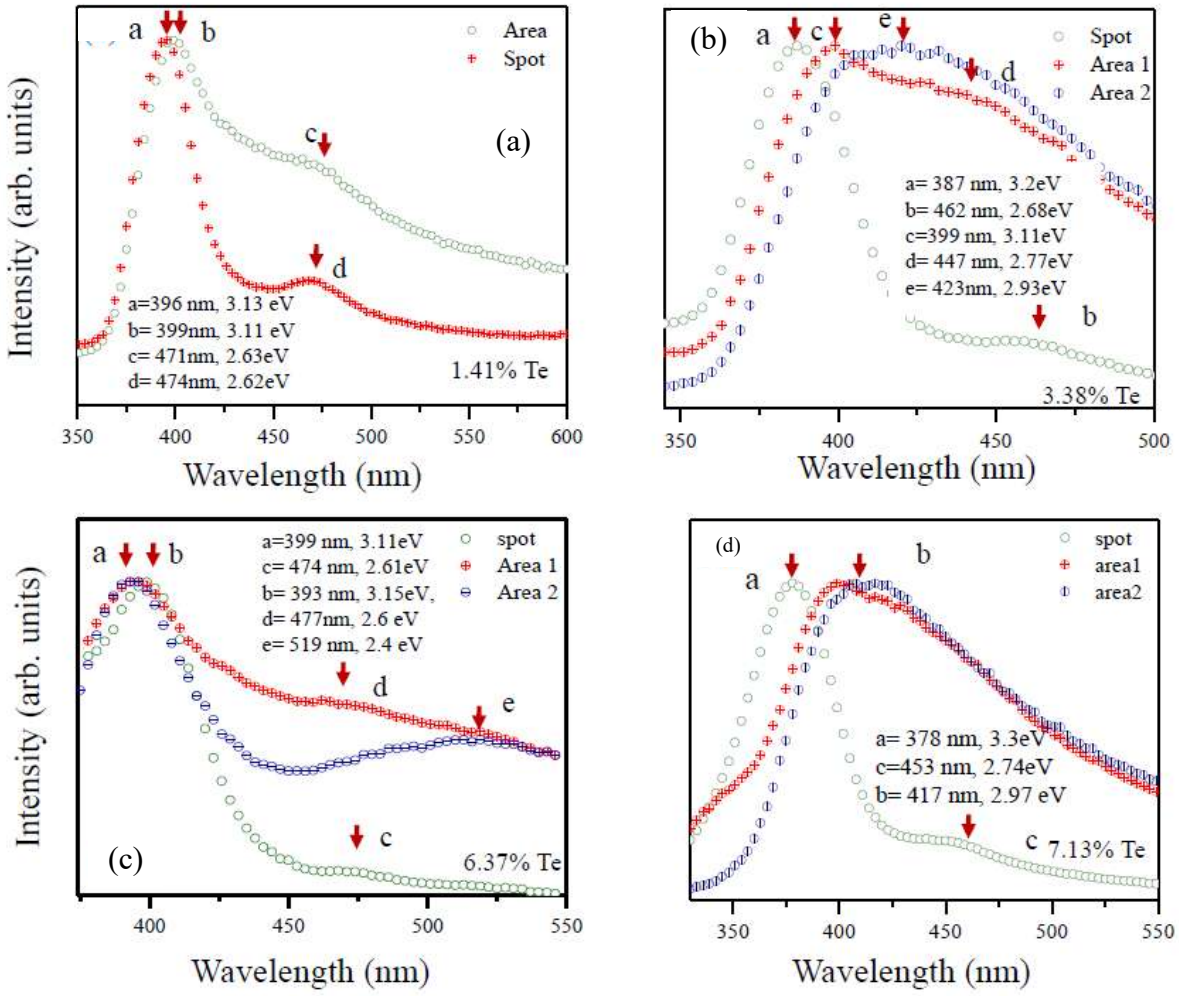

Figure 3.8 Experimental CL spectra from Te_{Zn} films with different Te content (a) 1.41% Te, (b) 3.38% Te, (c) 6.37% Te, and (d) 7.13% Te, showing in homogeneity in the composition along with defect emission peaks.

In the case of Te_{Zn}, variation in CL emission peaks from place to place is observed for samples with 3.38, 6.37 and 7.13 at % unlike Te_O case where consistent CL data is obtained at different regions of the film. Only for 1.4 at.% Te case, the CL data is region independent. Figure3.8 is the summary of CL data from four different transparent films (Te_{Zn}). There are two notable peaks in all the cases; these are around 400 nm (3.1 eV) and 470 nm (2.64 eV). For 1.41 % Te the spot and area CL spectra is the same except for the latter one is broader.There are two peaks, intense peak around 3.13 eV from due to Te doping and a defect peak at 2.62 eV possibly from V_O. For 3.4 % sample, three different CL spectra are observed. Spot scan gives two peaks at 3.2 and 2.7 eV. One type of area has peaks at 3.11 and 2.77 eV and another type of area has broad asymmetric peak at ~ 3 eV, could be the combined effect of Te and some form of defect possible V_{Zn}.

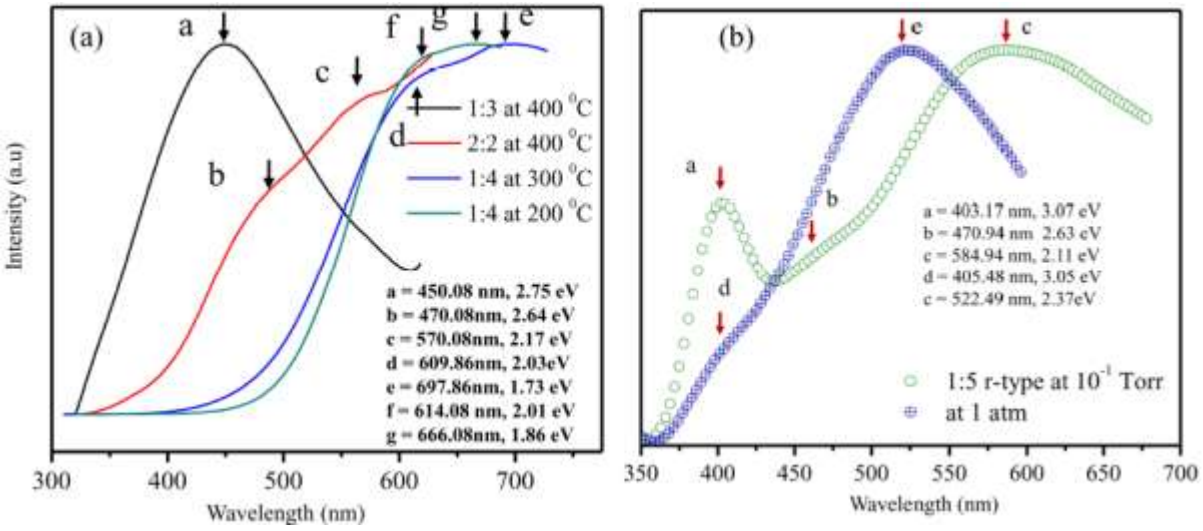

Figure 3.9 Experimental CL spectra of (a) higher % Te at O site and (b) 1:5 Li:ZnO:Te and 1:5 ZnO:Te films after annealing under oxygen at 1 atm and 0.1 Torr pressure.

Te at the Zn site will act as a donor and there is a possibility also for creation of vacancy Zn defects (V_{Zn}) in the presence of Te^{+4} at the Zn site. Therefore, the broad peak around 400 nm from some of the areas could be due to the compounding effect of Te at the Zn site along with V_{Zn}. For 6.37 % film, similar feature is observed except some areas having emission at 2.4 eV which lie in the higher wavelength side compared to other cases, may be because of some other type of point defects involved. For 7.13 % film, due to significant phase separation, Zn rich regions having peaks at 3.3 and 2.74 eV and Te rich regions having peak

around 2.97 eV are observed. Detailed theoretical calculation might shed light in assigning the exact type of point defects involved to explain the defect related emission peaks. Preliminary attempts to activate *p* conductivity in ZnO:Te (1:5 film) along with Li has been carried out through annealing under oxygen atmosphere. What is interesting to see the enhancement in emission at 2.37 eV(522.49 nm) and 2.11 eV (584.94 nm) for samples annealed under oxygen environment at 1atm and 0.1 Torr respectively, irrespective of presence or absence of dopants (Li) and alloying elements (Te) (figure 3.9). Therefore, it is clear that the observed green emission is not from V_O but related to some other origin. As there is a possibility for an equal population of V_O and V_{Zn} existenceupon such annealing (under Zn poor and O rich condition), the green emission could be assigned to this (Schottky type). One theory report also suggested that the green emission is probably due to such Schottky vacancy complex [19].Therefore the need will be to subdue such Shottcky type defects during annealing or in innovation in growth scheme to reduce their number in order to achieve *p*-conductivity in this system.

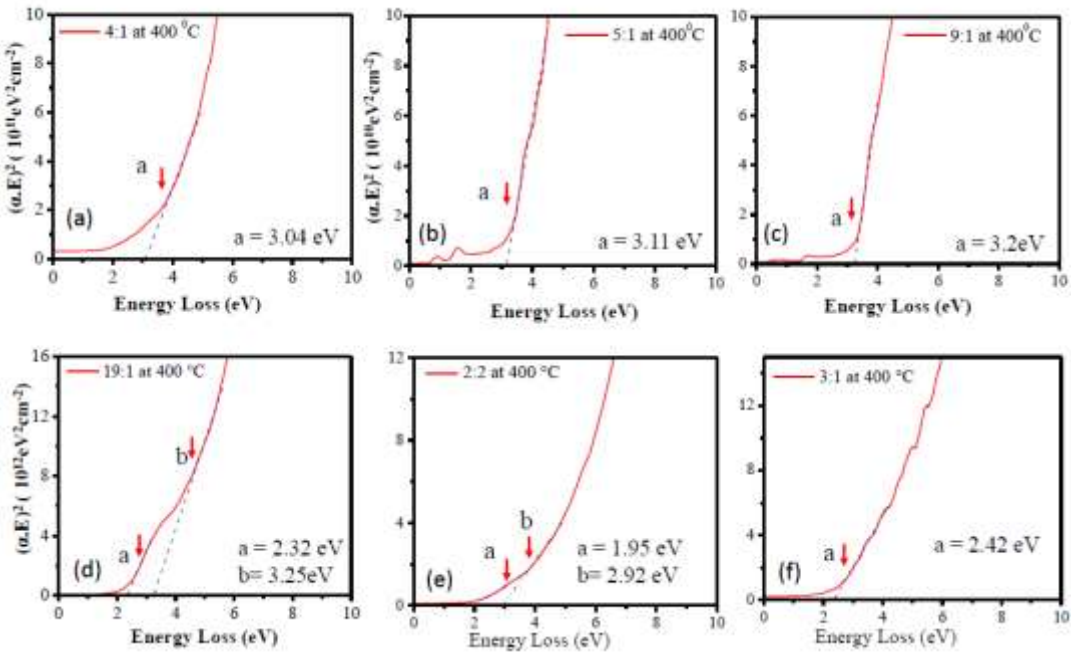

Figure3.10 (a)–(f) Direct band gap by low loss HREELS for ZnO:Te (O site) thin films with different Te concentrations.

It will also be interesting to probe various emission peaks mentioned above either by optical spectroscopy technique or high resolution electron energy loss spectroscopy (HREELS) to obtain clear ideas on the possible defect formation as well as band gap narrowing [20-22]. This can be a prospect for the future work. We have done some preliminary measurement on direct type band gaps by HREELS and obtain good match with the CL spectra (figure 3.10). We have observed similar type of band gap as in case of CL emission.

3.4.4 Band Bowing

A band bowing parameter '*b*' of 5.97 eV is obtained with the end compound being ZnTe. Theoretically, we obtained band bowing parameters of 7.66 eV (figure 3.11). Experimentally bowing parameters are derived without any support from the values near the ZnTe end of the plot. However, for theoretical bowing parameter some end values have been used. The discrepancy between the theory and experimentation for Te_O case is due to absence of values near the ZnTe side in the experimental plot.

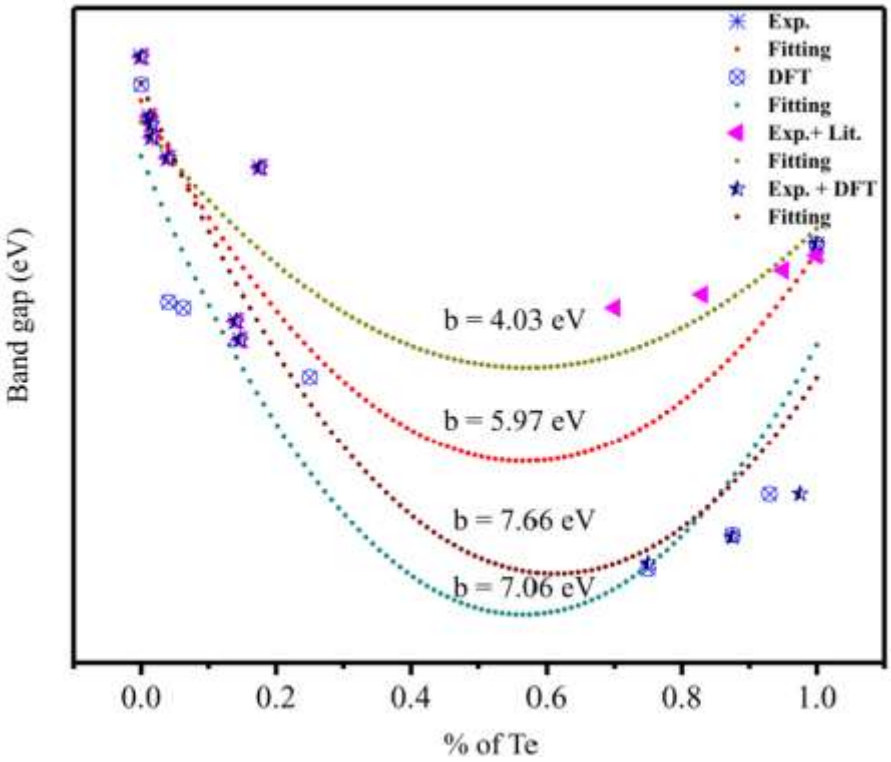

Figure3.11a theoretical band bowing parameter of 7.66 eV for ZnO films with $Te_O$is obtained. Experimentally, the value is 7.06 eV with the help of theory values at the ZnTe side.

Therefore, we have first used the band gap values reported in Ref. 23, but obtained a '*b*' parameter of ~4.03 eV, which is significantly lower than expected. This is because of inaccuracy in oxygen doping concentration in ZnTe film. However, if we utilize the theory data for this side along with the experimental numbers then the composite '*b*' parameter turns out to be 7 eV which is then close to the '*b*' parameter obtained from the theory alone (figure 3.11). The unavailability of data on either side resulted in incorrect band gap bowing reported in this system previously, which should be higher compared to ZnO:S and ZnO:Se, because of larger size of Te atom [24].

3.4.5 Density functional theory

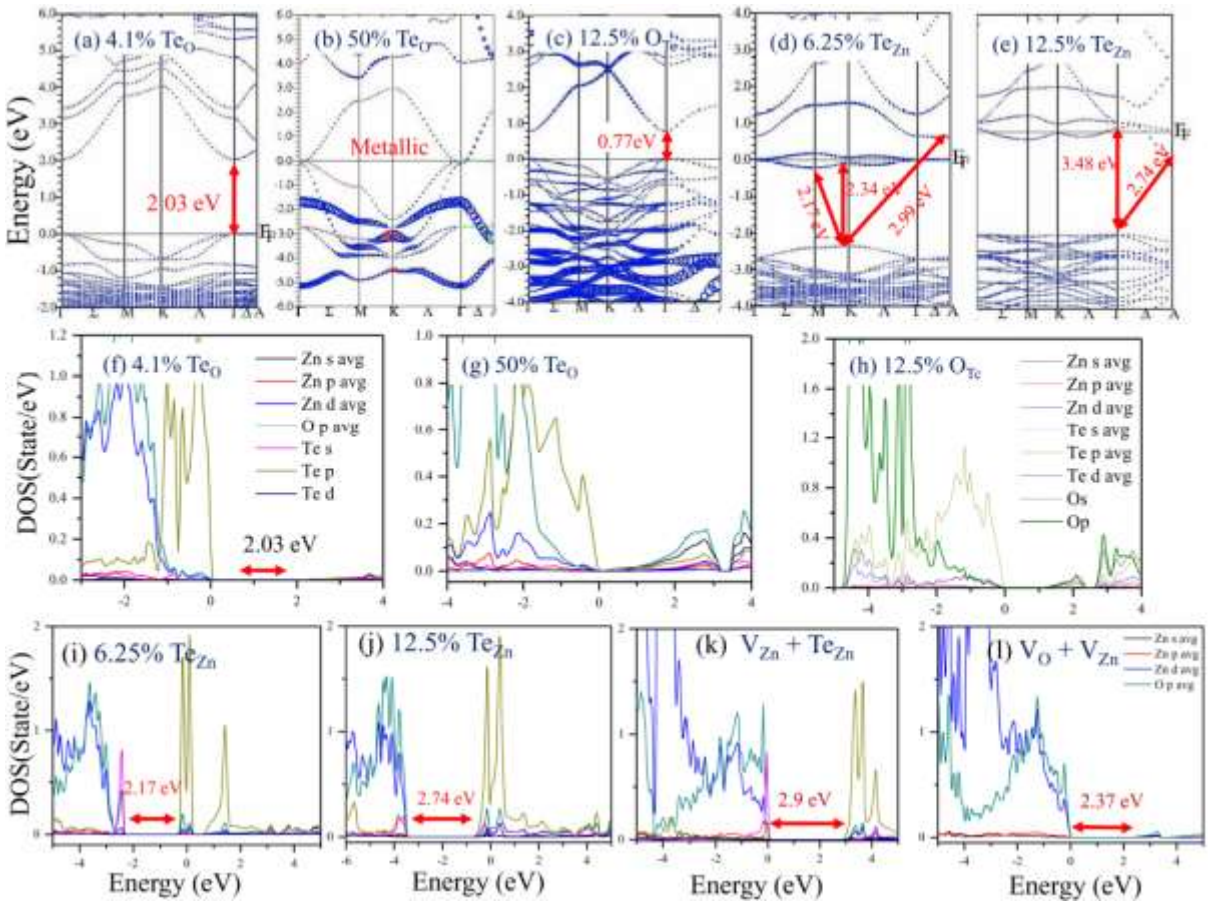

Figure 3.12 Band structure and density of plot calculated by mBJLDA potential within WIEN2k code for (a and f) 4.1% Te_O, (b and g) 50% Te_O, (c and h) 12.5% O_{Te}, (d and i) 6.25% Te_{Zn}, (e and j) 12.5% Te_{Zn}, (k) V_{Zn}+Te_{Zn} (6.25%), and (l) 6.25% Schottky defect (V_{Zn}+V_O).

Band gap, density of states and band structures are calculated by mBJLDA potential for Te_Ocase with different Te concentrations is presented below. Band gap decreases to ~2 eV and stays around the same value for 4.1, 6.25 and 12.5 % Te cases (figure 3.12(a) and figure 3.13(g)). For 25% case the band gap further decreases to 1.63 eV (figure 3.13(b)). For 50% case, conduction and valence band overlap and the super cell becomes *n*-type metallic (figure 3.12(b) & (g)). Calculation from ZnTe side after replacing Te with the O atoms gives band gap values of 1, 0.77 and 0.63 eV for 6.25, 12.5 and 25 % of O respectively (figure 3.13(e), figure 3.12(h) and figure3.13(f)). This results in a theoretical band bowing parameter (b) of 7.66 eV (figure 3.10). We can explain the bowing behavior in this system with the help of partial DOS. Te is less electronegative than O. It was pointed out in this context that in the dilute limit, the substitution of Te in ZnO (at the O site) gives states above the valence band maximum (VBM) and O substitution in ZnTe gives states below the conduction band minima (CBM), resulted in strong band bowing due to the localized impurity nature of these states [6].

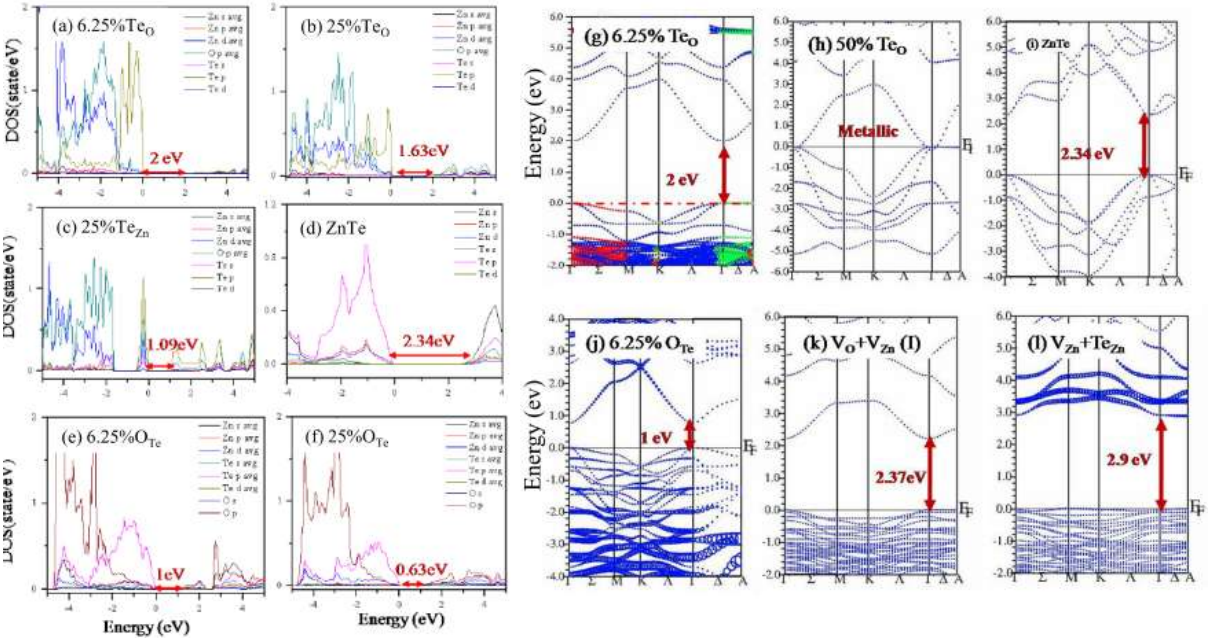

Figure 3.13Band structure and density of plot calculated by mBJLDA potential within WIEN2k code for different percentages of Te in both sides oxygen and zinc are shown in (a) to (f).

However, for higher percentages, the sates start mixing or line up with the host band structures (or band like states) and further decrease in the band gap is weak. From our

calculations, we obtain somewhat similar results, except we see continuous decrease in band gap values on Te substitution. In ZnO, the valence band edge is formed mostly by O *p* and Zn *d* states and the conduction band by Zn *s*. Upon introducing Te at the O sites, new states form just above the valence of band of ZnO, mostly by Te*p* states hybridized weakly with both O *p* and Zn *d* states (up to 12.5% Te) and decreases band gap to around 2 eV (figure 3.13 (a)). For 25% Te replacement (figure 3.13 (b)), the hybridization with Zn *d* and O *p* strengthens and Te *s* start contributing states at the bottom of the conduction band leading to further reduction of band gap to 1.63 eV. With the incorporation of more Te to 50%, Te *p* become more delocalized and the structure becomes *n*-type metallic. In the case of ZnTe (figure 3.13 (d) and (i)), the VBM is formed by Te *p* states and CBM is formed by mostly Zn *s* states. Upon replacing O in the Te site, new states form below the CBM mostly by O *s* and O *p* states, thus lowers the band gap in this system significantly (figure 3.13 (e)). Band gap decreases further with increasing incorporation of O atoms due to delocalization of states (figure 3.13 (f)). All the cases mentioned above, the nature of the band gap remains direct and thus strong band edge emission can be expected. DOS and band structure calculation in case of Te_{Zn} site resulted in *n*-type metallic behavior for 6.25 and 12.5 % Te and turns to semiconducting with a gap of 1.09 eV for 25% Te (figure 3.12(d), (e)&figure 3.13(c)). Two new bands around the Fermi level are formed for 6.25% case (figure 3.12(d)). These two new bands are like impurity band formed deep in the host band gap due to split Te *p* states with weak mixing between O *p* and Zn *d* states. This strong impurity like nature of Te in this case was explained previously as non-alignment of impurity states with the host bands in the case of common anion system [25]. Additionally, states form at the VBM due to Te *s* hybridized with O *p* states. The band gap is 2.99 eV from the VBM to the top of the unoccupied Te *p* band and 2.17 eV to the bottom of the unoccupied host CBM (marked with arrow). With 12.5% Te, the above described bands are observed to be lining up with the conduction bands and shows *n*-type metallic character with a band gap of 2.73 eV as measured between VBM to the bottom of unoccupied CBM. For 25% Te, the super cell becomes semiconducting with a band gap of 1.09 eV (measure between VBM to CBM) with the introduction of a band at the Fermi level mostly composed of Te *p* + O *p* + Zn *d*+ Te *s* states (figure 3.13(c)). Therefore, experimentally observed band gap of around 3 eVupto 7.13 at.%Te for Te_{Zn} case cannot be explained only with Te substitution at Zn site. Therefore, for Te_{Zn} case Te is possibly in Te^{+4} states, may force creation of Zn vacancy (V_{Zn}) in the lattice in order to maintain the charge neutrality. When the calculation is performed with V_{Zn} in the super cell along with Te, mBJLDA calculation yielded band gap at around 2.9 eV (figure 3.12 (k) and 3.13(l)) supports

the experimental observation. Therefore, for Te_{Zn}, the structure contains V_{Zn} which might be beneficial for subsequent attempt to render the film *p*-type(figure 3.12 (k) and 3.13 (l)). Besides emissions as mentioned above defect emission around 470 nm (2.64 eV) are observed in both the films which could be from V_O in the system (figure 3.7). V_O has already been shown to give emission around 2.78 eV both by mBJLDA calculation and experimental observation [18]. The peak at 2.4 eV may be from V_O-V_{Zn}Schottky type defect and is further supported by mBJLDA calculation as well (figure 3.12(l) and 3.13 (k)).

3.5 Conclusions

In conclusion, we have presented results on the control of ambipolar character of Te in ZnO lattice through the starting target pellets during pulsed laser deposition. For Te at the O site a maximum Te concentration of 4 at.% is obtained with the film to be in epitaxial form with a decrease in band gap emission to 2.8 eV. Attempting to incorporate more Te in the structure resulted in amorphous film formation. For Te at the Zn site, epitaxial film can be obtained up to Te concentration close to 3 at.%. Band gap stays almost the same value around ~ 3eV may be the compounding effect due to Te and V_{Zn} in the lattice. It is pointed out that control over Schottky pair (V_{Zn}+V_O) is important to achieve reliable p-doping in this system which require innovation in annealing procedure. Te position in the lattice is confirmed both by the color of the films and Te $M_{4,5}$EXELFS. The decrease in band gap for $Te_O$is strongly dependent on Te content compared to Te_{Zn} case. A band bowing parameter of around 7 eV is obtained for Te_O.

3.6 Bibliography

[1] O. Maksimov, Rev. Adv. Mater. Sci. **24**, 26 (2010).

[2] V. Avrutin, D.J. Silversmith, H. Morkoc, Proc. IEEE **98**, 1269 (2010).

[3] G. Brauer, J. Kuriplach, C.C. Ling, A.B. Djurisic, J. Phys.: Conf. Ser. **265**, 012002 (2011).

[4] K.Dileep, R.Datta, J. All. and Comp. **586**,499 (2014).

[5] K. Dileep,R. Sahu, K. K. Nagraja, R. Datta, J. Crys. Growth**402**, 124-129 (2014).

[6] S.H. Wei, A. Zunger, Phy. Rev. Lett.**76**, 664 (1996).

[7] H. L. Porter, J. F. Muth, J. Narayan, J. V. Foreman, H. O. Everitt, J. Appl. Phys.**100**, 123102 (2006).

[8] H. L. Porter, A. L. Cai, J. F. Muth, J. Narayan, Appl. Phys. Lett.**86**, 211918 (2005).

[9] S. H. Park, T. Minegishi, D. C. Ohb, J. H. Chang, T. Yao, T. Taishi, I. Yonenaga, J. Crys. Growth **363**, 190 (2013).

[10] K. Tang, S. Gu,K. Wu, S. Zhu, J. Ye, R. Zhang,Y. Zheng, Appl. Phy. Lett.**96**, 242101 (2010).

[11] S. Park, T. Minegishi1, D. Oh, D. Kim, J. Chang, T. Yao, T. Taishi, I. Yonenaga, Jpn. J. Appl. Phys. **52**, 055501 (2013).

[12] A. Iribarrena, P. Fern´andez, J. Piqueras, Superlattices and Microstructures **43**,600 (2008).

[13] A. Iribarren, P. Fernández, J. Piqueras, Phys. Status Solidi B **251**,3 (2013).

[14] F. Jamali-Sheini, R. Yousefi, M. R. Mahmoudian, N. AliBakr, A.Sa´aedi, N. Huang, Ceramics International **40**, 6 (2014).

[15] P. Blaha, K. Schwarz, G. K. H. Madsen, D. Kvasnicka, J. Luitz, WIEN2k, Vienna University of Technology, Vienna, Austria, (2001).

[16] B. Loukya, P. Sowjanya, K. Dileep, R. Shipra, S. Kanuri, L. S. Panchakarla, R. Datta, J.Cryst. Growth **329**, 20 (2011).

[17] R. L. Thomas, Vasuja, M. Hari, B. Nithyaja, S. Mathew, I. Rejeena, S. Thomas, V. P. N. ampoori, P. Radhakrishnan, J. Non. Opt. Phys. Mater. **20**, 351 (2011).

[18] R. Sahu, K. Dileep, B. Loukya, and R. Datta, Appl. Phys. Lett. **104**, 051908 (2014).

[19] R. Vidya,P. Ravindran,H. Fjellvag,B. G. Svensson,E. Monakhov,M. Ganchenkova,R. M. Nieminen, Phys. Rev. B **83**, 045206 (2011).

[20]K. Dileep, B. Loukya, P. Silwal, A. Gupta, R. Datta, J. Phys. D: Appl. Phys.**47**,405001 (2014).

[21]K. Dileep, B. Loukya, N. Pachauri, A. Gupta, R. Datta, J. Appl. Phys. **116**, 103505 (2014).

[22]K. Dileep, L.S. Panchakarla, K. Balasubramanian, U.V. Waghmare, R. Datta, J. Appl. Phys. **109**, 063523 (2011).

[23]S. Merita, T. Krämer, B. Mogwitz, B. Franz, A. Polity, B. K. Meyer, Phys. Stat. Sol. (c) **3**, 960 (2006).

[24] C.Y. Moon and S.H.Wei, Y. Z. Zhu, G. D. Chen, Phys. Rev. B **74**, 233202 (2006).

[25] J. Li and S. H. Wei, Phys. Rev. B **73**, 041201 (2006).

Chapter IV

Native defects affecting the Li atom distribution tune the optical emission of $Li_{0.06}Zn_{0.94}O$ epitaxial thin film

This chapter discusses on the possible origin defects and defect complexes related optical emission of Li:ZnO epitaxial thin films grown by Pulsed Laser Deposition. The observed optical emission is explained based on density functional theory based calculations.

This work has been published in Applied Physics Letter ***104,*** *051908 (2014).*

4.1 Introduction

ZnO is a wide band gap (3.3 eV) semiconductor with a large exciton binding energy of ~60 meV and is known to be an outstanding material for optoelectronics devices [1]. However, spontaneous formation of various native point defects and defect complexes upon doping leads to self-compensation depending on the processing conditions and the Fermi level stabilization energy. This phenomenon poses difficulty in obtaining stable *p*-type conductivity in ZnO and thereby hindering its application as a bipolar device [2]. Among various acceptor dopants, Li has been reported to have high solubility with ionization energy 0.09 eV above the valence band of ZnO [3]. Li has also been reported to take up both the substitutional (Li_{Zn}) and octahedral interstitial ($Li_{i(O)}$) positions [4, 5] as well as forming pair complex with native defect species. For example, Li_{Zn}-Li_i-V_{Zn} impurity-defect complex has been shown not only to give rise to *p*-type conductivity but also room temperature ferromagnetism [6]. Theoretically, it has been shown that the Li_{Zn}-Li_i pair complex is more stable than individual species [7-8]. There are reports where band gap increases upon Li doping [9, 10]. However, optical property is not known for Li pair complexes and how the presence of native defect influences the distribution of constituting species. In this article, we demonstrate how the arrangement of Li atoms in ZnO lattice is influenced by native point defect concentrations (oxygen vacancy V_O) and tune the Li related emission states in the system. We also show the local variation of Li arrangement changes the emission wavelength as measured by spatially resolved low loss EELS. We have grown epitaxial Li doped (6 at.%) ZnO films under two different growth conditions to control native defect population via controlling oxygen partial pressure during film deposition, i.e. 10^{-5} Torr (gives *n*-type conduction with carrier concentrations ~ 10^{19} cm^{-3}) and ~ 7×10^{-1} Torr (gives resistive sample with carrier concentrations ~ 10^{17} cm^{-3}) [11, 12]. Additional intense and broad CL emission peaks are observed at 2.99 eV and 2.1 eV in *n*-type and resistive type films respectively besides narrow emission peaks at 3.63 and 3.56 eV, which are higher than usual ZnO band gap. Li has been found to be occupying both the substitutional (Li_{Zn}) and interstitial (Li_i) positions as characterized by experimental Li K electron energy loss near edge spectra (ELNES) which is further supported by theoretical calculation performed using FEFF 9.05 code [13]. From the WIEN2k [14] based density functional theory calculations, we have studied different Li position and Li related complexes in ZnO lattice. Experimental result of CL spectra is well supported by WIEN2k based DFT calculation by considering Li_{Zn}-Li_i pair

complex with separation between the two constituting species at nearest and far positions. The theoretical band gap is calculated utilizing mBJLDA exchange correlation potential.

4.2 Experimental method

Li doped (6 at.%) ZnO pellets were prepared first by mixing and grinding ZnO and Li_2O powders (with 99.999% purity, obtained from Sigma Aldrich) and then sintering at 900 $^{\circ}$C. We have grown epitaxial thin films under two different oxygen partial pressure i.e., *n*-type ($pO_2 \sim 10^{-5}$ Torr, sample S1) and *r*-type ($pO_2 \sim 7\times10^{-1}$ Torr, sample S2) by PLD using KrF excimer laser (~248 nm wavelength) with a laser fluence of 1.5 J cm^2 used to ablate the target pellets. The details regarding the three step growth technique followed can be found in Ref. 11. The distance between the pellet and substrate was kept ~ 5 cm. The background electron carrier concentrations are 10^{17} cm^{-3} and 10^{19} cm^{-3} for *r*-type and *n*-type films respectively.

4.3 Theoretical calculation

The electronic structures of ZnO with different Li atom configurations were calculated using density functional theory (DFT) based WIEN2k code. Four different cases of interest were considered. (i) Substitutional Li (Li_{Zn}) of 6.25%, (ii) $Li_{i(Oct)}$ (octahedral interstitial, 6.25% Li), (iii) $Li_{i(Oct)}$ and Li_{Zn} forming a Li dimer and (iv) $Li_{i(Oct)}$ and Li_{Zn} away from each other. Generalized gradient approximation (GGA) was employed with Perdew-Burke-Ernzenhof (PBE) functional for optimization of lattice parameters and minimization of forces. The optimized ZnO lattice parameters were a = 3.2973 Å and c = 5.2824 Å. For the Li doped cases a 2×2×2 super cell was created. 12×12×6 k-mesh was used for ZnO unit cell and was reduced proportionally to the number of unit cell in each direction for the super cell calculations. Each super cell structure is optimized and the a and c lattice parameters changed by -0.72 % and -0.3% (%ΔV ~ -1.52)for case (i), + 1.43 % and -1.13 % (%ΔV ~ + 1.71) for case (ii), -0.2 % and +0.1 % (%ΔV ~ -0.27) for case (iii) and -0.2 % and +0.2 % (%ΔV ~ -0.16) for case (iv) respectively relative to un-doped ZnO. For the calculation of band gaps the modified Becke-Johnson potential (mBJ) was used. mBJLDA yields accurate band gap values and have already been tested for ZnO based alloys (doped with S) system [15-16].

We calculated Li K edge ELNES spectra using FEFF code which is a multiple scattering theory based calculation utilizing Green's function. The GGA optimized ZnO lattice

parameters from the WIEN2k calculation were used for FEFF calculations. The Hedin-Lundquist (HL) exchange correlation potential was used. The core hole was treated according to the 'final state rule'. A spherical cluster of 10 Å radius was used for the calculations with absorbing atom at the center. Two different cases where considered i.e. (i) Li_{Zn} and (ii) $Li_{i(Oct)}$ as the absorbing atoms.

4.4 Results & Discussion

4.4.1 Epitaxial growth & % Li quantification from EELS

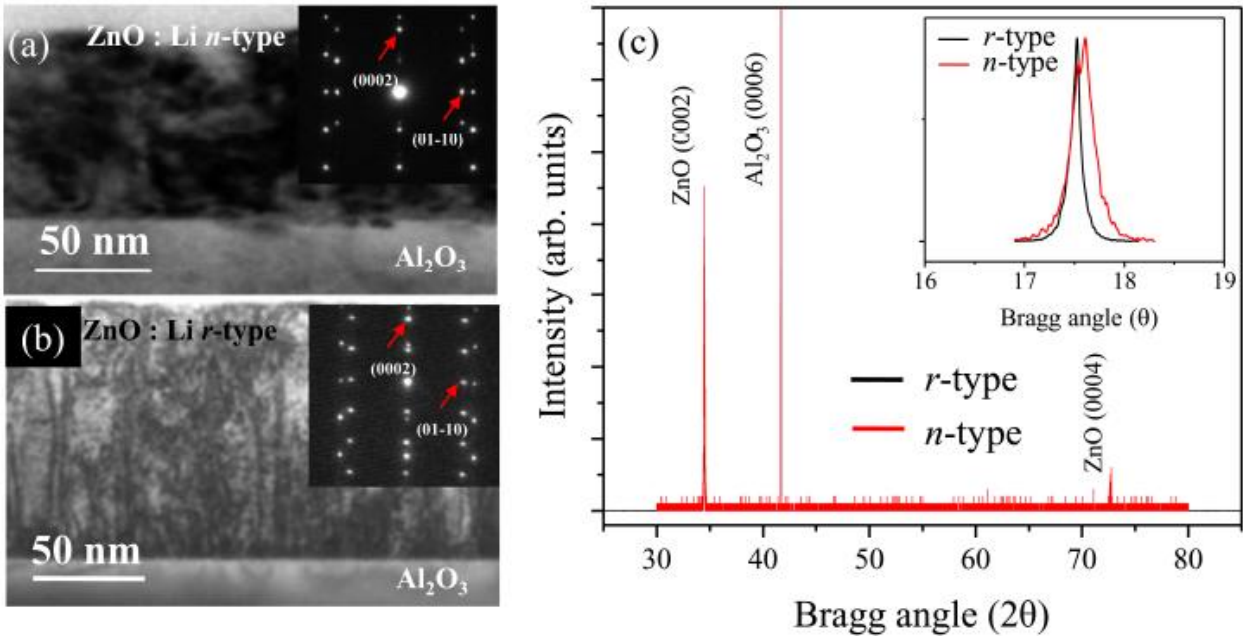

Figure 4.1 TEM bright field images with g = <0002> for (a) n-type and (b) r-type samples respectively. Diffraction pattern in the inset shows the film is epitaxial. (c) X-ray diffraction data showing slightly different lattice parameters for n and r-type films.

The TEM bright field image with g = 0002 and diffraction pattern along <01-10> zone axis of sapphire for sample S1 and S2 are shown in figure 4.1(a) & (b) respectively. The surface of the samples is smooth as can be seen in the cross sectional TEM images. The diffraction pattern confirms epitaxial (single crystalline) nature of the films. From X-ray diffraction measurement, the lattice parameter is found to be *a* = 3.2647 Å & 3.2491 Å (from

the asymmetric peak 101) and c = 5.099 Å & 5.2018 Å (from symmetric peak 002) for *n* type and *r*-type samples respectively (figure 4.1(c)).

We have quantified Li atom concentration in ZnO by EELS. Li K and O K EELS spectra are used for the quantification shown in the figure 4.2 (by fitting the experimental integrated energy loss intensity using Hartree-Slater atomic cross section model using Gatan Digital Micrograph EELS analysis software) [17]. The process of the quantification method we adopted involves the following steps. First step involves the splicing of the Li K and O K edge spectra that are acquired separately with 0.1 eV/ch and 1 mm aperture at 115 kX magnifications and calibrating the edge onset energy positions. The second step involves the background subtraction by extrapolating a power-law function which is fitted to the preceding excited edge region. The third steps involves the selection of Li K and O K edge and integrate the number of counts in the selected edge energy range under the cross-section. We used Hartee-Slater model to select the cross-section. The relative atomic ratio of Li and O is directly calculated from the absolute integrated areal density or the selected cross-section.

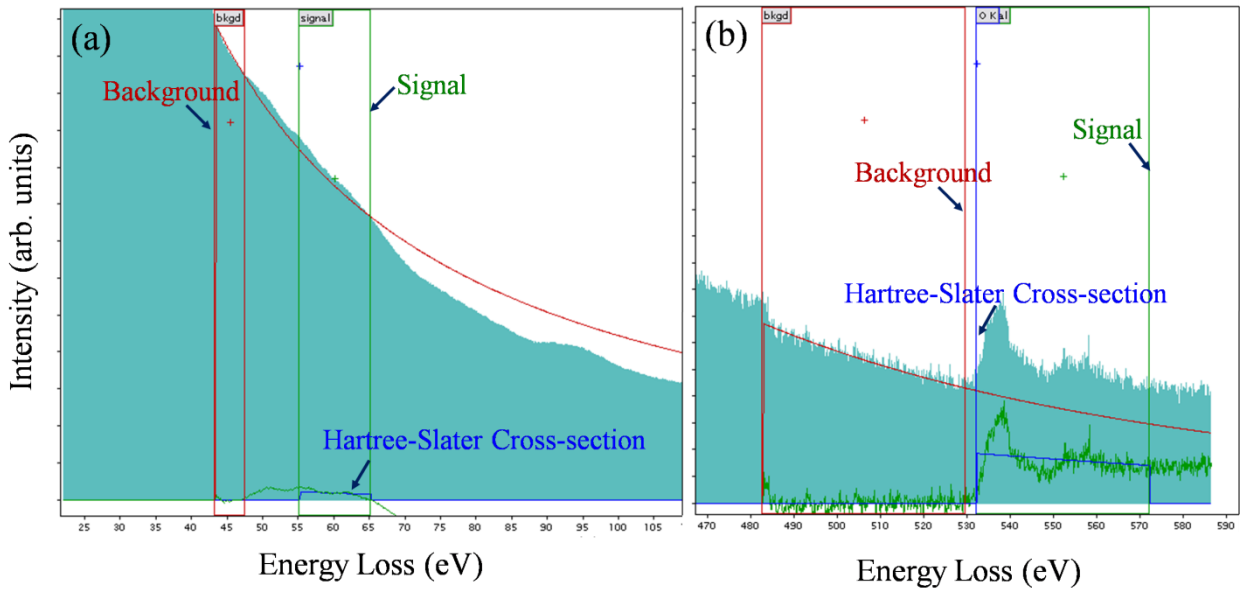

Figure 4.2 (a) Li K edge selected for quantification. (b) O K edge selected for quantification.

We have obtained almost the same Li concentration in both types of films i.e. 5.21±1.53% for *n*-type and 5.38±1.66 % *r*-type films. This quantification results is the average of that from at least four different regions of the sample.

4.4.2 Atomic position identification

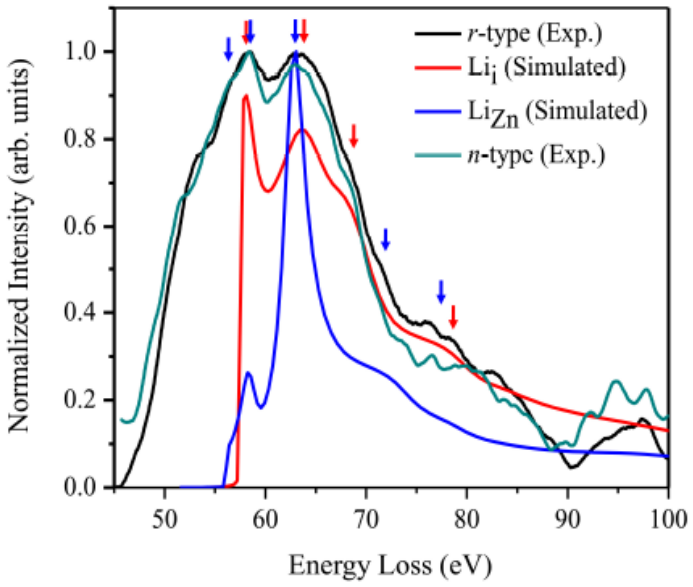

Figure 4.3 Li K ELNES of both experimental and FEFF code based simulated spectra suggesting that Li atoms have occupied both the substitutional and interstitial sites.

Figure 4.3 is the comparison of experimental and FEFF code based theoretical Li K ELNES spectra. From this comparison it is clear that the Li atoms have taken up both the substitutional and interstitial sites in ZnO lattice. The characteristic peaks corresponding to both the positions are reflected in the experimental spectra as marked with the arrows.

4.4.3 Band gap: CL & EELS

The most interesting observation in these two samples was done by CL emission spectra. Figure 4.4 shows the cross sectional CL spectra of the two samples. The *n*-type film is found to have broad emission at ~2.99 eV (414.6 nm) and a narrower emission at 3.63 eV (341.5 nm) (figure 4.4(a)), whereas the film grown with higher oxygen partial pressure (resistive) has broad emission at ~2.1 eV (590.4 nm) and a narrower emission at 3.56 eV (348.3 nm) (figure 4.4(b)) for almost the same amount of Li incorporation in the structure. Band emission at 3.63 eV and 3.56 eV are higher than the usual 3.3 eV across the ZnO band gap. There are reports where Li incorporation in ZnO increases the band gap [9, 10] and this

is due to the increase in cohesive energy (4.43 eV/atom compared to 3.5 eV/atom of ZnO) associated with the stronger Li-O bond.

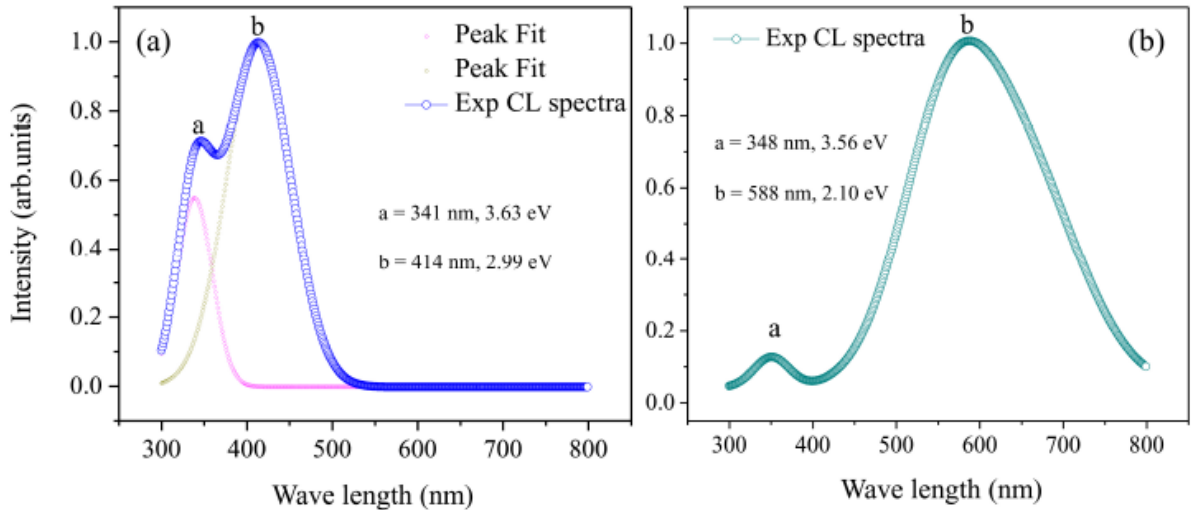

Figure 4.4 CL emission peaks for (a) n-type and (b) r-type samples showing Li complex related strong emissions at 2.1 and 2.99 eV respectively.

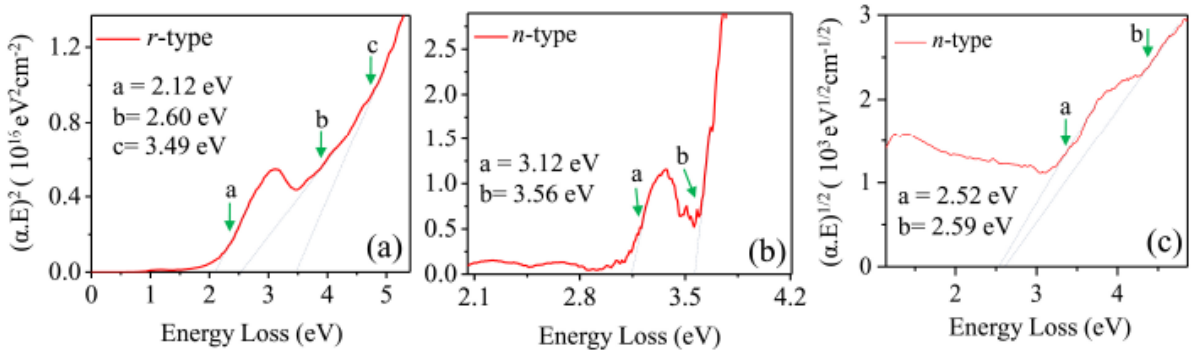

Figure 4.5 Direct band gap for (a) r-type (b) n-type sample and indirect band gap for (c) n-type samples determined by low loss EELS.

The intense and broad emissions at 3.03 and 2.16 eV are related with the different Li atom distribution which is influenced by oxygen vacancy defects which is supported in later section with theoretical simulation. Similar strong emission is not observed in *n* and *r*-type samples without Li doping [18]. CL data provides the average band gap information from the sample. As one can see the variation in Li atom concentration from the EELS quantification data, we thought to probe the band gap by high resolution EELS (obtained using a gun monochromator with energy resolution better than 0.18 eV) at different locations in the

sample in the nano-meter length scale. We indeed observed the variation in the band gap values in the samples at different locations and only representative information are given in figure 4.5.

The method of analyzing band gap from low loss EELS spectra through Kramers-Kronig analysis can be found in Ref. 16 & 18. We see typically two direct band gaps for *n*-type sample and three in some places for *r*-type samples. From Kramers –Kronig analysis it is found that the *n*-type sample has two band gaps at 3.12 eV and 3.56 eV (with some distribution from this value) and *r*-type sample has three band gaps 2.12 eV, 2.60 eV and 3.49 eV (with some distribution from this value). The values at 3.56 eV of *n*-type and 3.49 eV of *r*-type are the main band edge emission which are higher than usual ZnO band gap and are in agreement with CL measurement. Other band gap values at e.g., 3.12, 2.12 and 2.60 eV for both the samples is due to Li pair complexes and the variation in separation between complex species due to oxygen point defects.

4.4.4 Density functional theory

The cohesive energy for various super cell configurations has been calculated. We have found that the Li_{Zn} is energetically most favorable system having a cohesive energy of 4.43 eV/atom The Li_{Zn}-Li_i [configuration (iii)] complex has cohesive energy almost the same value i.e. 4.40 eV/atom. This shows that the Li_{Zn}–Li_i [configuration (iii)] and Li_{Zn} can coexist in the structure under thermodynamic equilibrium condition. $Li_{i(Oct)}$ alone is unlikely with a cohesive energy of 3.43 eV. Li_{Zn}-Li_i [configuration (iv)] system, with a cohesive energy of 4.27 eV/atom can also become a dominant dopant complex in the system under certain thermodynamic condition. Using mBJLDA exchange correlation potential we have calculated the band gaps for four different configurations. The calculated band structure and density of states (DOS) for Li_{Zn} shows Fermi level inside the valence band and results in a *p*-type semiconductor (figure 4.7). The calculated band gap for Li_{Zn}–Li_i [configuration (iii)] system is 3.03 eV (figure 4.6 (a)), which has an excellent matching of experimentally observed emission at 2.99 eV for the *n*-type sample suggesting that the low oxygen partial pressure assisted the Li_{Zn}–Li_i dimer formation. Interestingly, the Li_{Zn}–Li_i [configuration (iv)] dopant complex system shows a reduced mBJLDA band gap of 2.16 eV (figure. 4.6 (b)) which is matching well with the emission observed at 2.1 eV for the *r*-type sample. We propose that the higher oxygen partial pressure in the *r*-type growth condition has replenished the oxygen

vacancies in the system and thus energetically favoring the formation of Li_{Zn}–Li_i [configuration (iv)] system over Li_{Zn}-Li_i [configuration (iii)] system. One additional absorption peak at 2.60 eV observed by low loss EELS for *r*-type sample could be due to intermediate separation between Li_{Zn} and Li_i species considered in the calculations, emission energy is observed to be increasing when the individual species closing in. The contributions from Li atoms from various positions in the lattice in the band structure can be obtained by comparing the band structure with the DOS plot (figure 4.6 (a)-(c) and figure 4.7).

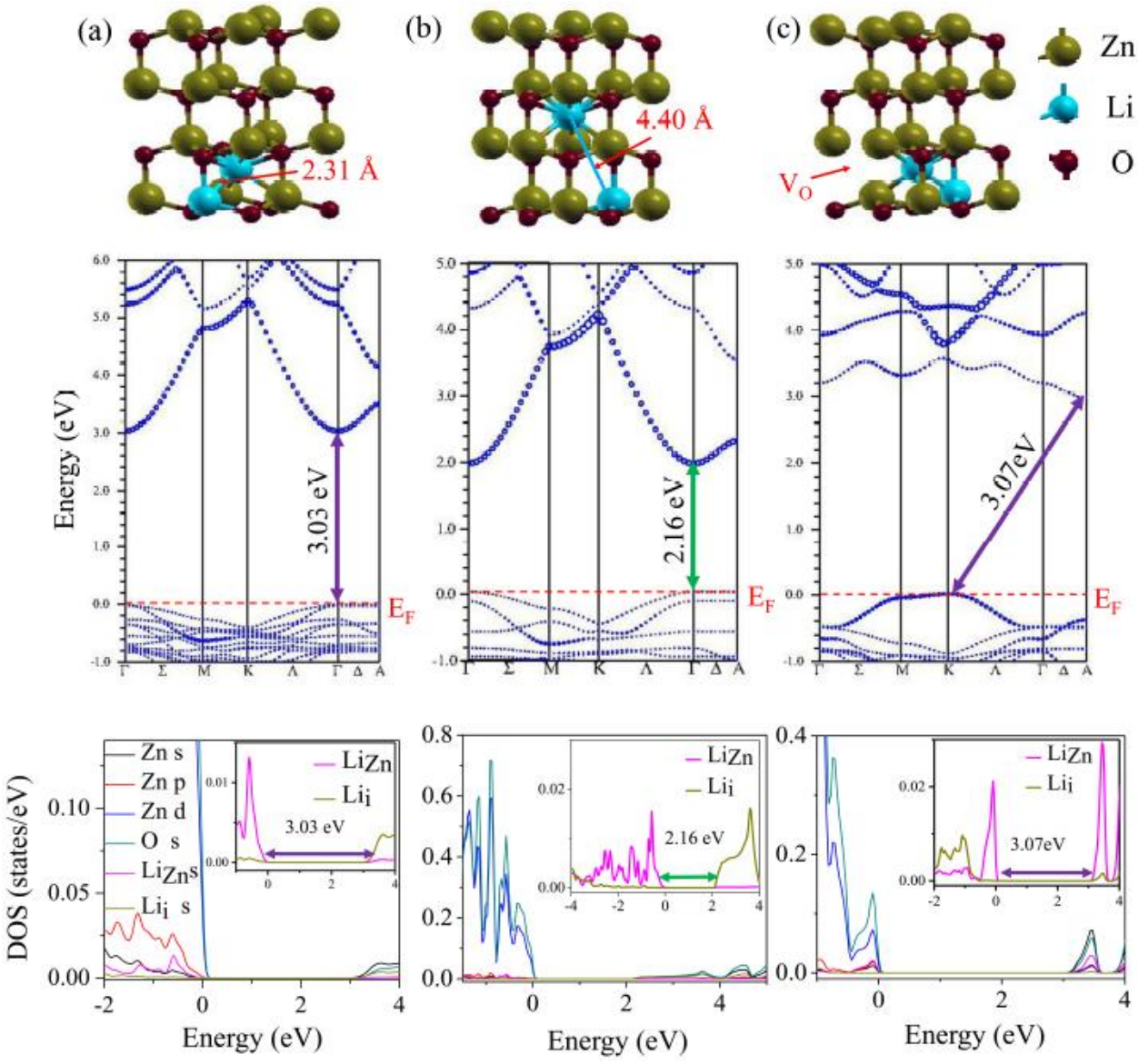

Figure 4.6 Model structure, DOS and band structure of Li complex configurations with individual species at (a) nearest and (b) away from each other considered for DFT calculation. Band gaps are marked in the figures. Li complex along with V_O is given in (c).

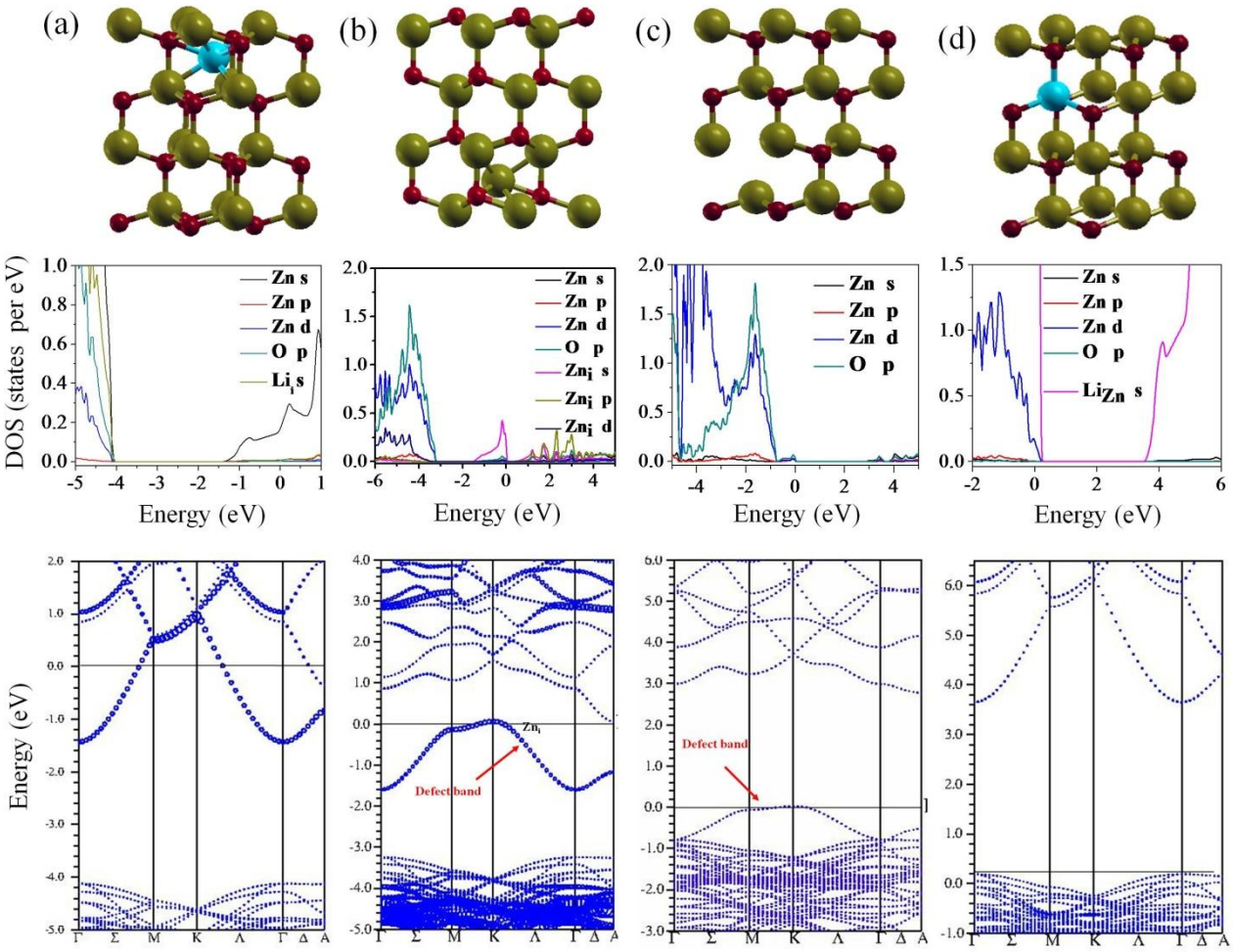

Figure 4.7 Li s orbital shows contribution in conduction band for Li_i and in valance band for Li_{Zn} system. In figure (b), defect band is hybridized of s, p, and d orbital of Zn_i. The distance between defect band and conduction band is 0.6 eV. In figure (a) and (d) the distance between valance band and conduction band are 2.69 eV and 3.46 eV for Li_i and Li_{Zn} respectively.

Another interesting feature from the low loss EELS spectra is the observation of indirect band gap at 2.52 and 2.59 eV for Li doped *n*-type sample (figure. 4.5 (c)). Further DFT calculation (with mBJLDA potential) with V_O and [Li_{Zn}-Li_i complex + V_O] system also shows indirect band gap at 2.78 and 3.07 eV (figure. 4.6 (c)). Green emission is believed to be due to V_O in ZnO [19]. However, the observation of indirect band gap associated with oxygen vacancy defects may not be responsible for the n-type conduction in the film as controversy still existing in the literature in its origin [20-24].Resistive type sample did not show any experimental indirect band gap due to low concentrations of V_O.

4.5 Conclusions

In conclusion, the role of oxygen vacancy defects in the separation of individual species in Li_{Zn}-Li_i complex system is presented. The separation influences the complex related emission in the ZnO system as shown experimentally by CL and low loss EELS and is supported theoretically by mBJLDA first principle based band gap calculation. It will be further interesting to see whether this emission in the visible range has any application in converting solar energy into electricity.

4.6 Bibliography

[1] Ü. Özgür, Ya. I. Alivov, C. Liu, A. Teke, M. A. Reshchikov, S. Doğan, V. Avrutin, S. J. Cho, H. Morkoc, J. Appl. Phys. **98**, 041301 (2005).

[2] V. Avrutin, H. Morkoe, Proc. IEEE **98**, 1269 (2010).

[3] C. H. Park, S. B. Zhang, S. Wei, Phys. Rev. B **66**, 073202 (2002).

[4] Z. Zhang, K. E. Knutsen, T. Merz, A. Y. Kuznetsov, B. G. Svensson, L. J. Brillson, Appl. Phys. Lett. **100**, 042107 (2012).

[5] G. Srinivasan, R. T. R. Kumar, J. Kumar, J. Sol-Gel. Sci. Technol. **43**, 171 (2007).

[6] J. B. Yi, C. C. Lim, G. Z. Xing, H. M. Fan, L. H. Van, S. L. Huang, K. S. Yang, X. L. Huang, X. B. Qin, B. Y. Wang, T. Wu, L. Wang, H. T. Zhang, X. Y. Gao, T. Liu, A. T. S. Wee, Y. P. Feng, J. Ding, Phys. Rev. Lett. **104**, 137201 (2010).

[7] M. G. Wardle, J. P. Goss, P. R. Briddon, Phys. Rev. B **71**, 155205 (2005).

[8] X. Sun, Y. Gu, X. Wang, Y. Zhang, Chinese J. Chem. Phys. **25**, 261 (2012).

[9] G. Li, S. Sambasivam, S. B. Kim, S. W. Park, B. C. Choi, J. H. Jeong, B. E. Jun, J. Korean Phys. Soc. **59**, 2770 (2011).

[10] G. A. Mohamed, E. Mohamed, A. A. El-Fadl, Physica B **949**, 308-310 (2001).

[11] B. Loukya, P. Sowjanya, K. Dileep, R. Shipra, S. Kanuri, L. S. Panchakarla, R. Datta, J. Cryst. Growth **329**, 20 (2011).

[12] D. S. Negi, B. Loukya, K. Dileep, M. Kesaria, N. Kumar, R. Datta, Superlatt. Microstruct. **63**, 289 (2013).

[13] J. J. Rehr, J. J. Kas, F. D. Vila, M. P. Prange, K. Jorissen, Phys. Chem. Chem. Phys. **12**, 5503 (2010).

[14] P. Blaha, K. Schwarz, G. K. H. Madsen, D. Kvasnicka, and J. Luitz, WIEN2k, Vienna University of Technology, Vienna, Austria (2001).

[15] D. Koller, F. Tran, P. Blaha, Phys. Rev. B **85**, 155109 (2012).

[16] K. Dileep, R. Datta. J. All. and Comp. **586**, 499 (2014).

[17] B. Loulya, D. S. Negi, K. Dileep, N. Kumar, J. Ghatak, R. Datta, J. Magn. Magn. Mater. **345**, 159 (2013).

[18] Q. Sun, H. Sims, D. Mazumdar, J. X. Ma, B. S. Holinsworth, K. R. O'Neal, G. Ki, W. H. Butler, A. Gupta, J. L. Musfeldt Phys. Rev. B **86**, 205106 (2012).

[19] K. Dileep, L. S. Panchakarla, K. Balasubramanian, U. V. Waghmare, R. Datta, J. Appl. Phys. **109**, 063523 (2011).

[20] S. B. Zhang, S. H. Wei, A. Zunger, Phy. Rev. B **63**, 075205 (2001).

[21] P. Agoston, K. Albe, R. M. Nieminen, M. J. Puska, Phys. Rev. Lett. **103**, 245501 (2009).

[22] A. Janotti, C. G. Van de Walle, Phy. Rev. B **76**, 165202 (2007).

[23] C. G. Van de Walle, J. Phys.: Condens. Matter **20**, 064230 (2008).

[24] A. Janotti, C. G. Van de Walle, Rep. Prog. Phys. **72**, 126501 (2009).

Chapter V

Stable *p*-type conductivity in B and N co-doped ZnO epitaxial thin film

This chapter discusses on the observation of stable p-type conductivity in B and N co-doped epitaxial ZnO thin films grown by pulsed laser deposition. This p-type conductivity is associated with the significant decrease in defect emission peaks due to the vacancy oxygen (V_O) and Schottky type-I native defects compared to films grown at low oxygen partial pressure (~10^{-5} Torr). The p-type conductivity is explained with the help of density functional theory calculation considering off-stoichiometric BN_{1+x} in the ZnO lattice.

This work has been published in physica status solidi (b), ***253 (3),*** *504-508 (2016).*

5.1 Introduction

ZnO is a wide band gap semiconductor with a band gap of ~3.4 eV and a strong exciton binding energy of 60 meV at room temperature [1, 2]. ZnO offers itself as an alternative candidate for the expensive GaN based LEDs and various other bipolar junction based device technologies [3-8]. However, *p*-type doping remains elusive in this system. Spontaneous formation of native defects upon doping or alloying depending on the position of Fermi energy compensates the effects of any attempt to render the film *p*-conducting [9, 10]. Among various approaches to overcome the issue, valence band engineering [11, 12], synthesizing various defect complex systems in the host ZnO lattice has been reported [13-15]. Valence band engineering is generally performed by alloying with S, Se or Te substitution at the O site which raises the valence band of ZnO up in the energy with respect to the vacuum level, thus reduces the ionization energy gap between the acceptor dopants and the host valence band. Among various defect complexes which gave rise to *p*-type conductivity in ZnO, V_{Zn}-N_O-H^+ shallow acceptor complex with ionization energy of 130 meV exhibit strong (carrier concentration ~ 10^{18} cm^{-3}) room temperature *p*-type behavior [13]. This defect complex was stabilized by following an elaborate process flow starting from the formation of V_O-N_O to V_{Zn}-N_O-H^+ complex with post growth annealing as a final step to remove interstitial H^+ which otherwise would act as a donor. Theoretical calculation also suggested that V_{Zn}-N_O complex can give rise to stable *p*-doping via transformation from an initial metastable *p*-type N_{Zn}-V_O complex and this can help reducing the compensation effect during the film growth [14]. From these reports, it is clear that many different possibilities exist in obtaining *p*-conductivity in this system. Among various dopants, N has been one of the favorite choices because of its low ionization energy (0.2-0.4 eV); however, its low solubility has been reported to be an issue. Ionization energy of N in ZnO of 0.2 and 0.4 eV have been reported by experimentation and theory calculation, respectively [16, 17]. Co-doping has been proposed as an alternative to increase the solubility of dopant e.g., N in ZnO using BN as a source for N [18, 19]. However, equal percentage of donor and acceptor atoms will not render ZnO *p*-conducting. There are already reports where BN incorporation gave *p*-type conductivity in this system, however not stable over the period of time. In the present report, we describe obtaining a stable *p*-type conductivity in ZnO epitaxial thin films grown by pulsed laser deposition (PLD) through N substitution at the O site using BN for the source of N along with higher oxygen partial pressure (10^{-1} Torr) to minimize the formation of native defects particularly vacancy oxygen (V_O) and Schottky type-I native defects.

Cathodoluminescence (CL) spectra shows significant drop in emission intensity related to V_O and Schottky type defects in films grown under high oxygen partial pressure (10^{-1}Torr) compared to films grown under low oxygen partial pressure (10^{-5} Torr). The reduction of such defects along with substitution of N at the O site is responsible for the observation of *p*-type conductivity in the present case. The *p*-conductivity is robust even after eight to nine months unlike other reports where demise of *p*-type conductivity over a time period has been reported. With the help of first principle based calculation it is understood that the off-stoichiometric BN_{1+x} incorporation in ZnO by chance is responsible for the *p*-conductivity in this system which is in agreement with previous calculation of formation energy based on such BN_{1+x} clusters in ZnO lattice [20]. The carrier concentration (~3×10^{16} cm^{-3}) and mobility (10 cm^2/V.s) are still not optimum for any practical device application but the results in general contribute to the knowledge of doping, acceptor complexes and role of native defects in ZnO.

5.2 Experimental method

BN (1 at. %) doped ZnO thin films were grown using pulsed laser deposition technique. The pellet was prepared by mixing and grinding ZnO and BN powder (with 99.9% purity, obtained from Sigma Aldrich) and then sintering at 900 °C for 8 hours in a closed box furnace under atmospheric condition. We have grown epitaxial thin films on '*c*' plane sapphire under two different oxygen partial pressure, we will call them *n*-type (pO_2 ~ 10^{-5} Torr, sample) and *r*-type (pO_2 ~ 7×10^{-1} Torr,) by PLD using KrF excimer laser (~248 nm wavelength) with a laser fluence of 1.5 J cm^2 used to ablate the target pellets. Two different strategies were used, with and without 50-80 nm thick ZnO buffer layer on '*c*' plane sapphire substrate prior to the growth of BN:ZnO films. The use of buffer layer helps in achieving epitaxial and smooth films or flat morphology. We have found that small islands are formed without ZnO buffer for the present case. The films growth was followed according to the three step growth technique already reported previously [15, 21]. The distance between the pellet and the substrate was kept ~ 5 cm. The background electron carrier concentrations are 10^{16} cm^{-3} and 10^{19} cm^{-3} for *r*-type and *n*-type films, respectively. Carrier concentration and mobility at room temperature were calculated from Hall measurements performed with the physical property measurement system (PPMS, Quantum Design).

5.3 Theoretical calculation

The electronic structures of ZnO with BN doping with different atomic configurations were calculated using density functional theory (DFT) within WIEN2k code which uses full potential linear augmented plane waves (LAPW) as basis [22]. For the B and N doped cases 2×2×2 supercells were created (6.25 % of B and N). 12×12×6 k-mesh was used for the ZnO unit cell and was reduced proportionally to the number of unit cells in each direction for the supercell calculations. Seven different cases of interest were considered. (i) $B_{Zn}+N_O$, (ii) $N_O+B_{i(Oct)}$, (iii) $B_{i(Oct)}$ (iv) B_{Zn}, (v) N_O, (vi) $B_{Zn}+B_{i(oct)}$, and (vii) $N_O+N_{i(oct)}$. We have used generalized gradient approximation (GGA) with Perdew-Burke-Ernzenhof (PBE) functional for optimization of lattice parameters and minimization of forces. The forces were minimized below1 Ry/a.u. Energy of separation between core and valence states were -6 Ry. The muffin tin radii were chosen such that they do not overlap. The K_{max} value for plane wave basis was equal to $7.00/R_{MT(min)}$ ($R_{MT(min)}$ is the Muffin tin radius of the smallest atom). Each supercell structure is optimized and the *a* and *c* lattice parameters changed -1 % and + 1.25% (%ΔV ~ -3.2)for case (i), + 0.08 % and +1.4 % (%ΔV ~ + 1.24) for case (ii), -6.44 % and +16.94 % (%ΔV ~ +2.37) for case (iii), -5.49 % and +9.64 % (%ΔV ~ -2.06) for case (iv), – 1.03% and + 1.52% (%ΔV ~ -0.56%)for case (v), +0.33% and 0.36% (%ΔV~ +1.02%) for case (vi), and +0.29% and +0.74% ((%ΔV ~ +1.33%) for case (vii), respectively, relative to undoped ZnO. GGA approximation does not provide an accurate description of excited electronic states and thus predicts incorrect band gap values. To study the band gap with various doping configurations, a modified Becke–Johnson (mBJ) potential was used as proposed by F. Tran and P. Blaha also known as mBJLDA, we have performed mBJ calculation after GGA, so it should be called mBJGGA in our case [22]. This method gives band gap close to GWA (GW approximation; G stands for Green function and W stands for coulomb interaction) but computationally not expensive. It yields band gaps accurately for strongly correlated p–d semiconductor systems [7, 23 and 24].

5.4 Results and Discussion

5.4.1 SEM imaging

It is found that using a thin 50-80 nm ZnO buffer layer is very important to ensure wetting and subsequent growth of epitaxial and smooth thin film of BN:ZnO. SEM images in figure 5.1 compare the surface quality of two different films grown with and without ZnO buffer layer. Film grown without buffer layer shows uniform distribution of distinct rough or

3-dimensional (3D) crystal morphology approximately 100-200 nm in size other than 2-dimensional (2D) film areas. Point EDS confirmed that both the areas are composed of ZnO. Whereas, the film grown with the buffer layer consist of only 2D films because of improved wetting.

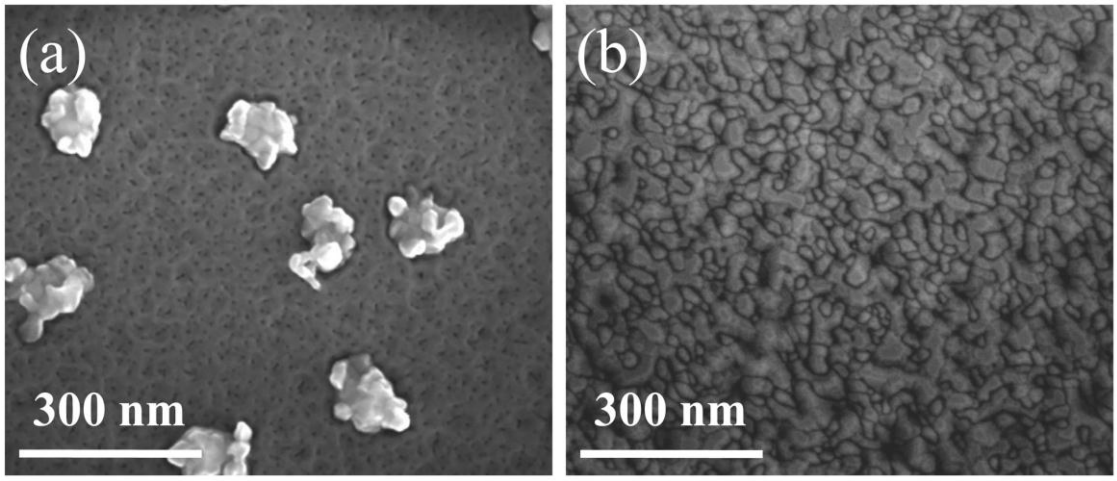

Figure 5.1 SEM images of BN:ZnO film (a) without and (b) with ZnO buffer.

This is unlike the previous report where we used such a buffer layer in order to incorporate higher atomic concentrations of S and Te in ZnO epitaxial films [11, 12]. The appearance of 3D crystal morphology in films without buffer layer may be related with the presence of BN and its non-uniform distribution in ZnO as well as lattice mismatch with sapphire substrate is responsible for two different types of growth of seed crystals.

5.4.2 Epitaxial growth: XRD & HRTEM

Thin film XRD shows epitaxial relationship between substrate and doped ZnO. It is confirmed that no other phases are present showing (0001) ZnO || (0001) Al_2O_3 and [11-20] ZnO || [01-10] Al_2O_3 in the figure 5.2.

Example TEM, HRTEM and diffraction pattern from BN:ZnO films with high oxygen partial pressure are shown in figure 5.3. From the diffraction pattern it can be seen that the films are epitaxial and presence of threading dislocations can be observed. The epitaxial relationship between the film and sapphire is [11-20] ZnO || [01-10] Al_2O_3 and [0001] ZnO || [0001] Al_2O_3.

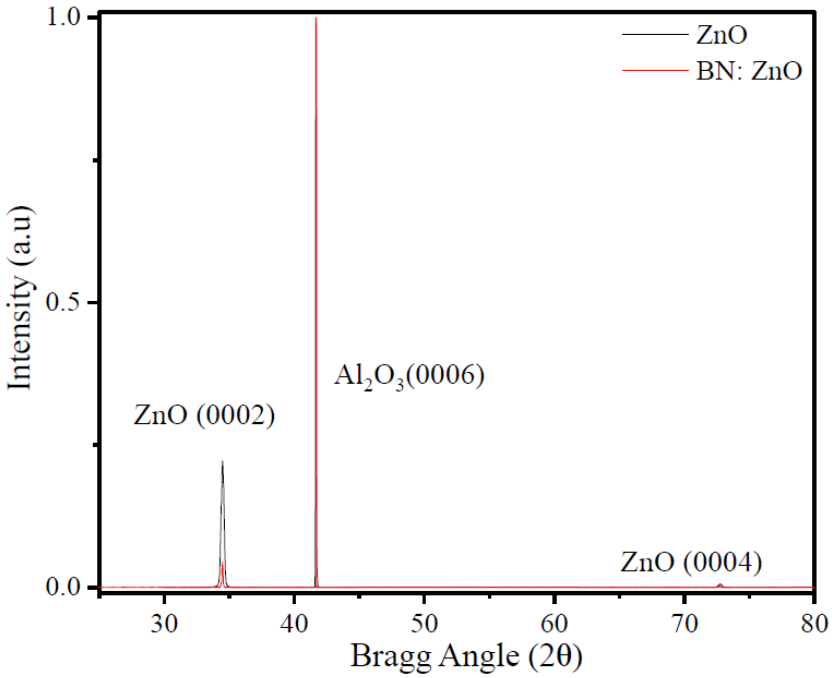

Figure 5.2 Thin film XRD shows epitaxial growth of BN:ZnO.

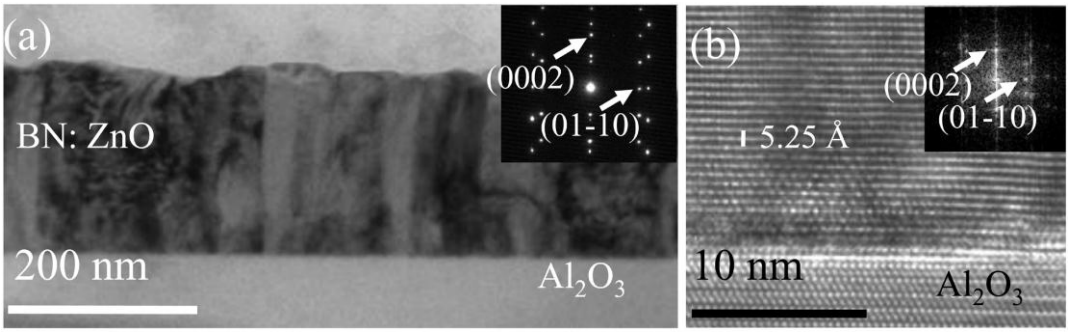

Figure 5.3 TEM bright field images with g = <0002> for (a) p-type samples and (b) HRTEM image along <11-20> Z.A. Diffraction pattern in the inset shows the film is epitaxial.

No poly-crystallinity due to randomly orienting grains is observed from the TEM or HRTEM images.

5.4.3 CL & Hall measurement

Figure 5.4(a) shows the resistivity *vs.* magnetic field data for thin grown with high oxygen partial pressure i.e. 10^{-1} Torr. The slope of the plot is positive and confirms the *p*-type conductivity. The mobility and carrier concentrations are calculated to be 10 $cm^2/V.s$ and 3×10^{16} cm^{-3}, respectively. The films which are grown under low oxygen partial pressures i.e. 10^{-5} Torr show *n*-type conductivity and the details are given in the figure 5.4 (d). Figure 5.4 (c) shows measurement after nine months to retain *p*-type conductivity with same carrier concentration and mobility.

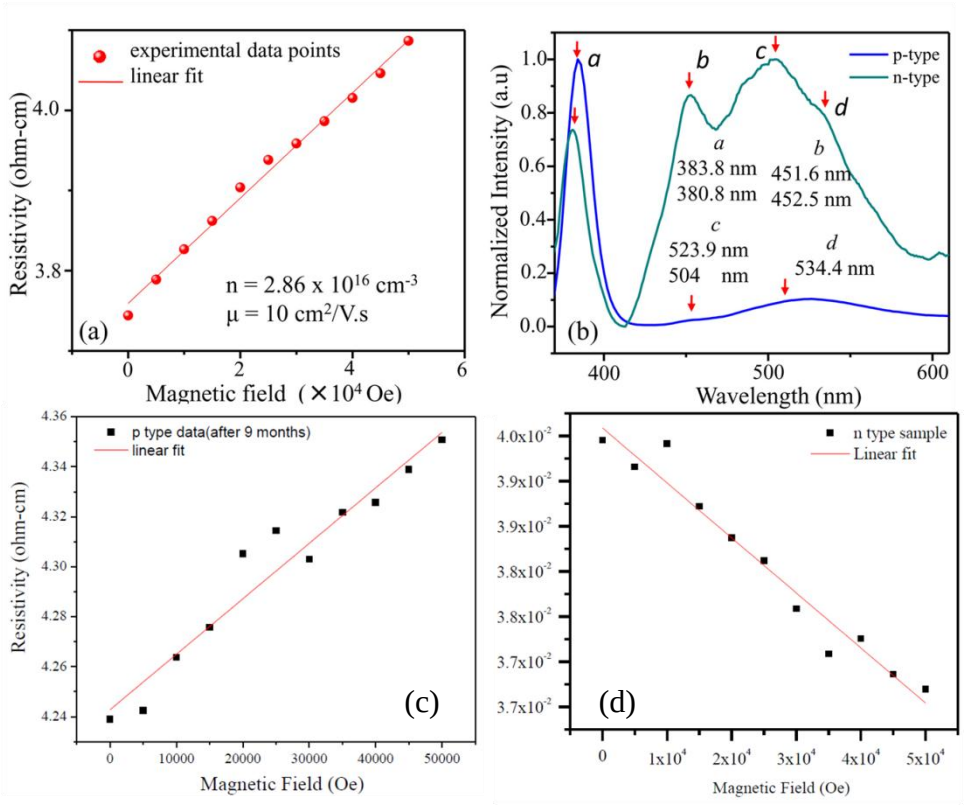

Figure 5.4 (a) Resistivity vs. Magnetic field plot shows the p-type conductivity of the film with carrier concentration and mobility are 3×10^{16} cm^{-3} and 10 $cm^2/V.s$, respectively. (b) CL emission peak for p-type and n-type samples showing significant reduction in defect emission peaks for the p-conducting sample. (c) Resistivity vs. Magnetic field measurement after 9 months and (d) is for n- type sample.

Figure 5.4 (b) shows the CL spectra from films grown under two different oxygen partial pressures i.e. *n*-type and *r*-type growth conditions. Other than emission around 3.25 eV

(381.5 nm) across the band gap of ZnO, there are two prominent defect related emissions at 2.73 eV (454.15 nm) and 2.45 eV (506.1 nm) can be observed. These emissions are due to V_O and Schottky type-I defects, respectively. Previous mbJGGA based band gap calculation already suggested that the emission at 2.73 eV is due to V_O and the present calculation suggests that the emission at 2.45 eV is due to Schottky type-I defects [8, 25]. The Schottky type of defects forms spontaneously upon annealing of ZnO with the attempt of rendering the film *p*-type by reducing V_O concentration and thus kills the prospect to turn the film *p*-type [12]. However, in the present case BN doping in ZnO under *n*-type growth condition led to the formation of V_O other than Schottky type defects and under *r*-type growth condition these two defect emission peaks are suppressed significantly without any post annealing procedure. The suppression of these two defect related peaks might be responsible for the observation of *p*-type conductivity in the present film. Another peak around 2.3 eV is also observed in the present case and this could be due to BN_{1+x} cluster formation and we support and discuss this with the help of mbJGGA calculated band gap values in the subsequent paragraphs.

5.4.4 Density functional theory

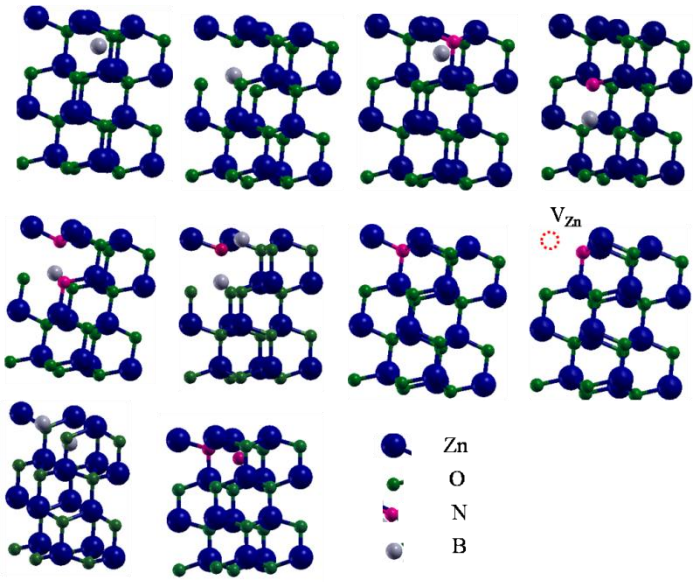

Figure 5.5 Schematic representation on model structures in DFT.

We have been actively investigating on *p*-doping problem in ZnO for last few years and attempted various routes e.g. through mono atomic acceptor doping of ZnO with Li [15], valence band engineering of ZnO by S and Te along with mono (Li) [11, 12] and co-acceptor doping (Li and Ag) at the Zn site [7] but none of the approaches succeeded except the present case of co-doping with BN. Therefore, we have carried out first principle based calculation for some possible combinations of dopants, dopant complexes, and dopant defect complexes in this system.

Dopant/ dopant complex	Cohesive energy (eV)	Band gap (eV)
Li_i	3.43	2.69
Li_{Zn}	4.43	3.46
Li_i-Li_{Zn} (far)	4.4	2.16
Li_i-Li_{Zn} (near)	4.27	3.03
B_{Zn}	4.38	2.65
B_i	4.23	-
B_{Zn}–$N_{2\,(O)}$	4.55	2.62
N_O	4.39	2.86

Table 5.1 Cohesive energy and band gap for various dopants and dopant-complex configurations obtained by GGA and mBJGGA calculations are listed here.

Table 5.1 summarizes the cohesive energy values for some configurations and for the remaining is given in figure 5.6. Our previous calculation carried out on Li_{Zn}:ZnO system shows that the energy difference between Li_{Zn} (4.43 eV/atom) and Li_{Zn}+Li_i (far configuration) (4.4 eV/atom) is only 0.03 eV/atom [15]. Therefore, Li is likely to take up both types of positions i.e. substitutional and interstitial positions in the ZnO lattice and the prospect for *p*-type conductivity will be restricted. Whereas, in the case of BN doped ZnO i.e. B_{Zn}+N_O the cohesive energy is relatively much higher (4.57 eV/atom) compared to individual substitution of species i.e. B_{Zn} (4.38 eV/atom) and N_O (4.39 eV/atom) as shown in the Table 5.1. For the band structure and DOS for various calculated combinations are given in figure

5.7 along with the prediction on the type of conductivity for each case. However, stoichiometric BN incorporation will not give rise to *p*-type conductivity in ZnO (figure 5.6 (a)). Therefore, what is required is the imbalance in atomic percentage in B and N while incorporating in the ZnO lattice. Our calculation shows that BN_2 cluster has almost the same stability (4.55 eV/atom) as BN (4.57 eV/atom) and slight distribution in terms of separation between B and N atoms can increase the cohesive energy value or stability further as in the case of Li where Li_{Zn}+Li_i (far configuration) has higher stability (4.4 eV/atom) than Li_{Zn}+Li_i (near configuration) (4.27 eV/atom) [15].

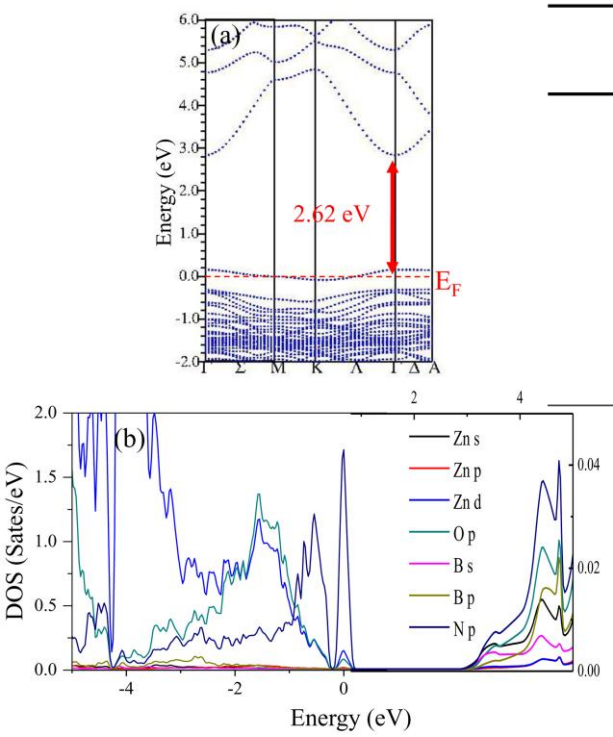

Dopants, defects and complexes	Cohesive energy (eV)
N_O	4.39
$B_{2(Zn)}$_N_O	4.76
B_i-BZ_n	4.3
B_{Zn}-N_O	4.57
B_i-N_O	4.27
$N_{(O)}$-V_{Zn}	4.33
$N_{(i)}$-$N_{(O)}$	4.21

Figure 5.6 (a) & (b) show the band structure and density of states for p type BN_2. Cohesive energies of different structures are listed in the table.

The band structure and DOS for BN_2 cluster for the present calculation is shown in figure 5.6(b) where one can see that the Fermi level is in the valence band and the ZnO will be *p*-type conducting. In this context, Cui *et al.* carried out various BN_x and molecular $N_{2(O)}$ configurations and found out that it is the higher atomic ratio of N to B and the most suitable one is the BN_3 cluster for giving rise to p-conductivity in ZnO [20]. N_2 molecule at the O site ($N_{2(O)}$) is responsible for killing the prospect of *p*-conductivity in ZnO and this mechanism

was proposed for the demise of *p*-conductivity in ZnO over a period of time say, within few weeks or months or during post growth annealing. This explained the observed *p*-conductivity reported in this system by Sui *et al.* [18, 19]. However, in our case *p*-conductivity in robust and still persistent even after 8-9 months measured on the same sample. We have preserved this sample for any further future measurement. One more difficulty under this proposition is that how to control such an off-stoichiometric composition of BN_{1+x} experimentally. The experimental result by Sui *et al.* as well as in the present case suggests that by chance we are getting such off-stoichiometric BN_{1+x} during film growth. This is not surprising during PLD growth where it was shown previously that Co metal can be grown from the starring pellet of Co:ZnO pellets and the composition of the target pellet is not reliably transferred to the growing film [26]. The experimental methods have been serendipitous because calculation for B_2N shows more stability (4.76 eV/atom) compared to BN_2 case (4.55 eV/tom) which if formed would give rise to *n*-type conductivity (figure 5.6).

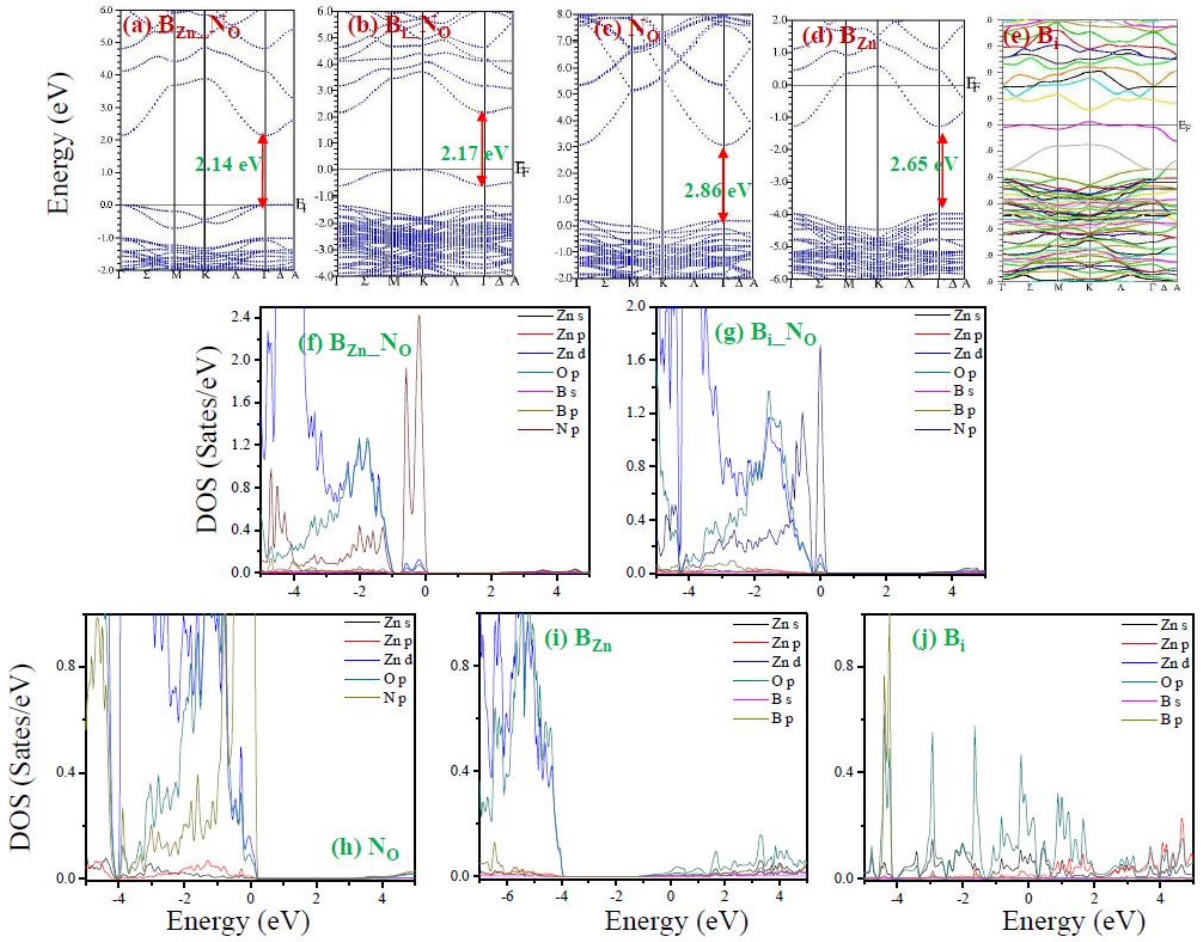

Figure 5.7 (a) - (j) are the band structures and density of states of different combination of B and N in ZnO to understand their conductivity.

We have carried out band gap calculation with various doping and doping complexes using mbJLDA potential. This method gives accurate band gap values in ZnO and for Li dopant and doping complexes the prediction was in close agreement with previous experimental measurements [15]. The theory calculation provides an excellent guide to get a feedback on what is happening with the optical emission spectra with different types of dopants, defects and complex possibilities. CL spectra in figure 5.4(b) show three prominent peaks: *a* = 383 nm (3.23 eV) due to ZnO band gap, *b* = 451 nm (2.75 eV) due to V_O, *c* = 524 nm (2.37 eV) due to $V_O + V_{Zn}$ type I Schottky and *d* = 540 nm (2.3 eV) possibly due to BN_{1+x} cluster. The band gap due to BN and BN_2 substitution in ZnO is 2.14 eV and 2.62 eV respectively (figure 5.7). Any values of numbers of N atom between 1 and 2 will reduce the band gap and can give a value of 2.3 eV as observed experimentally. Additionally, our calculation yields band gap values for N_O and B_{Zn} to be 2.86 and 2.65 eV, respectively.

5.5 Conclusions

In conclusion, we have shown experimentally that *p*-type conductivity in ZnO epitaxial film can be obtained with off-stoichiometric doping of BN_{1+x} cluster during PLD growth. Experimental condition serendipitously favored the formation of off-stoichiometric BN_{1+x} cluster without any prior strategy and post growth processing and annealing. *p*-type conductivity is associated with significant reduction of defect and doping cluster emission peaks compared to the main emission peak across ZnO band gap. *p*-type conductivity is robust and still persisting even after 8-9 months while preparing this report. The result shows one more way to incorporate and stabilize N atoms in the ZnO lattice to achieve *p*-type conductivity.

5.6 Bibliography

[1] Ü. Özgür, Ya. I. Alivov, C. Liu, A. Teke, M. A. Reshchikov, S. Doğan, V. Avrutin, S. J. Cho, H. Morkoc, J. Appl. Phys. **98**, 041301 (2005).

[2] V. Avrutin, H. Morkoe, Proc. IEEE **98**, 1269 (2010).

[3] C. J. Humphreys, MRS BULLETIN **33**, 459-470 (2008).

[4] S. Nakamura, G. Fasol, The Blue Laser Diode (1997).

[5] A. Tsukazaki, A. Ohtomo, T. Onuma, M. Ohtani, T. Makino, M. Sumiya, K. Ohtani, S. F. Chichibu, S. Fuke, Y. Segawa, H. Ohno, H. Koinuma, M. Kawasaki, Nat. Mater. **4**, 42 (2005).

[6] Y. S. Choi, J. W. Kang, D. K. Hwang, S. J. Park, IEEE Trans. Electron. Devices **57**, 26 (2010).

[7] K. Dileep, R. Datta, J. All. and Comp. **586**, 499 (2014).

[8] R. Sahu, K. Dileep, D. S. Negi, K. K. Nagaraja, R. Datta, Phys. Stat. Sol. (b) **252**, 1743–1748 (2014).

[9] O. Maksimov, Rev. Adv. Mater. Sci. **24** , 26 (2010).

[10] W. Walukiewicz, Physica B **302-303**, 123 (2001).

[11] K. Dileep, R. Sahu, K. K. Nagaraja, R. Datta, J. Crys. Growth **402**, 124 (2014).

[12] R. Sahu, K. Dileep, D. S. Negi, K. K. Nagaraja, S. Shetty, R. Datta, J. Crys. Growth **410**, 69 (2015).

[13] J. G. Reynolds, C. L. Reynolds, Jr. A. Mohanta, J. F. Muth, J. E. Rowe, H. O. Everitt, D. E. Aspnes, Appl. Phys. Lett. **102**, 152114 (2013).

[14] L. Liu, J. Xu, D. Wang, M. Jiang, S. Wang, B. Li, Z. Zhang, D. Zhao, C. Shan, B. Yao, D. Z. Shen, Phy. Rev. Lett. **108**, 215501 (2012).

[15] R. Sahu, K. Dileep, B. Loukya, R. Datta, Appl. Phys. Lett. **104**, 051908 (2014).

[16] L. Wang, N. C. Giles, Appl. Phys. Lett. **84**, 3049 (2004).

[17] C. H. Park, S. B. Zhang, Su-Huai. Wei, Phy. Rev. B **66**, 073202 (2002).

[18] Y. R. Sui, B. Yao, J. H. Yang, L. L. Gao, T. Yang, R. Deng, M. Ding, T. T. Zhao, X. M. Huang, H. L. Pan, D. Z. Shen, J. Lumin. **130**, 1101 (2010).

[19] Y. R. Sui, B. Yao, Z. Hua, G. Z. Xing, X. M. Huang, T. Yang, L. L Gao, T. T Zhao, H. L Pan, H. Zhu, W. W. Liu, T. Wu, J. Phys. D: Appl. Phys. **42**, 065101 (2009).

[20] Y. Cui, F. Bruneval, Appl. Phys. Lett. **97**, 042108 (2010).

[21] B. Loukya, P. Sowjanya, K. Dileep, R. Shipra, S. Kanuri, L. S. Panchakarla, R. Datta, J. Cryst. Growth **329**, 20 (2011).

[22] P. Blaha, K. Schwarz, G. K. H. Madsen, D. Kvasnicka, J. Luitz, WIEN2k: an Augmented Plane Wave + Local Orbital Program for Calculating Crystal Properties: http://www.wien2k.at/index.html (2001).

[23] K. Dileep, B. Loukya, N. Pachauri, A. Gupta, R. Datta, J. App. Phys. **116**, 103505 (2014).

[24] K. Dileep, B. Loukya, P. Silwal, A. Gupta, R. Datta, J. Phys. D: Appl. Phys., **47**, 405001 (2014).

[25] R. Vidya, P. Ravindran, H. Fjellv°ag, B. G. Svensson, E. Monakhov, M. Ganchenkova, R. M. Nieminen, Phys. Rev B, **83**, 045206 (2011).

[26] D. S. Negi, A. Roy, B. Loukya, K. Dileep, S. Shetty, N. Kumar, P. S. Anil Kumar, R. Datta, J. Cryst. Growth **394**, 112 (2014).

Part II

Chapter VI

Large scale epitaxial growth and $1T_d$ phase stability of MoS_2 and WS_2

This chapter from second part of the thesis describes large scale epitaxial thin film of transition metal dichalcogenides (MoS_2 and WS_2) on highly lattice mismatched sapphire (α-Al_2O_3) substrate in low cost PLD system and it also gives a brief introduction about poly-type phase transition.

6.1 Transition metal dichalcogenides

The journey of two dimensional materials starts with Graphene. Due to having lack of band gap, research community shifted their attention to other layered materials particularly MoS_2, WS_2, ReS_2 based inorganic transitional metal dichalcogenides (TMDs).TMDs for example MoS_2, WS_2 etc are three atoms thick where the cationic plane is sandwich between two anionic plane (figure 6.3) [1].These TMDs reveals many unique physical and chemical phenomena. Most of them exhibit indirect to direct band gap crossover from bulk to monolayer form [2] and promising for extremely thinnest transistors [3], exploring fundamental physics, and energy related applications. TMDs also show unique properties in terms of its excition and valley properties of electron [4-10] which can be used to fabricate novel devices. But the device industry is mainly dependent on CVD [11, 12] growth which is costly and suffers from large scale growth. We have addressed two ultimate problems in this part, firstly we have discussed about majors drawbacks and their solutions to grow epitaxial thin film of TMDs (MoS_2 & WS_2) at low cost by PLD. In second problem we deal with 1T phase stability of TMDs because they shows interesting feature through their qualitative phase transition. This metal semiconductor state makes them proper candidates for switchable device applications.

6.2 Epitaxial thin film growth of MoS_2 and WS_2 on highly lattice mismatched substrate of *c*-plane sapphire substrate

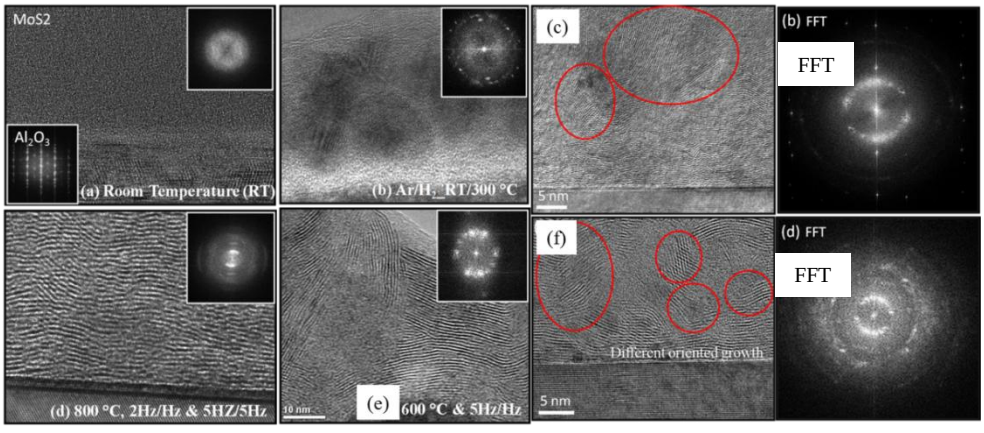

Figure 6.1 (a) and (b) are amorphous growth at room temperature and Ar/H_2 cleaned substrate at 300°C temperature. (d) and (e) are polycrystalline growth at 800°C and 600°C with 2Hz/2Hz, 5Hz/5Hz and 5Hz/5Hz. (c) and (f) rotated grain at 1Hz/1Hz, 5Hz/5Hz and 2Hz/2Hz laser frequency.

We have followed our three step method referred in section 1.2 for the epitaxial thin film growth of MoS_2 and WS_2 on highly lattice mismatched substrate (16%) of the *c*-plane sapphire substrate. This strategy did not work well. It is found that the films appeared as amorphous. We have changed our conditions and understood due to van der Waal forces between the layers, epitaxial growth condition needs more relaxation time compared to ZnO thin film. Figure 6.1 describes different conditions like; i) room temperature growth, ii) Ar/H_2 cleaned substrate at 300°C growth and iii) different temperatures with different laser frequency, where only amorphous, polycrystalline and rotated grain are found. We have found reduced rotated grain when 1Hz laser frequency is used at nucleation temperature and 5Hz is used at final temperature at 800°C (figure 6.1 (c) and (f)).

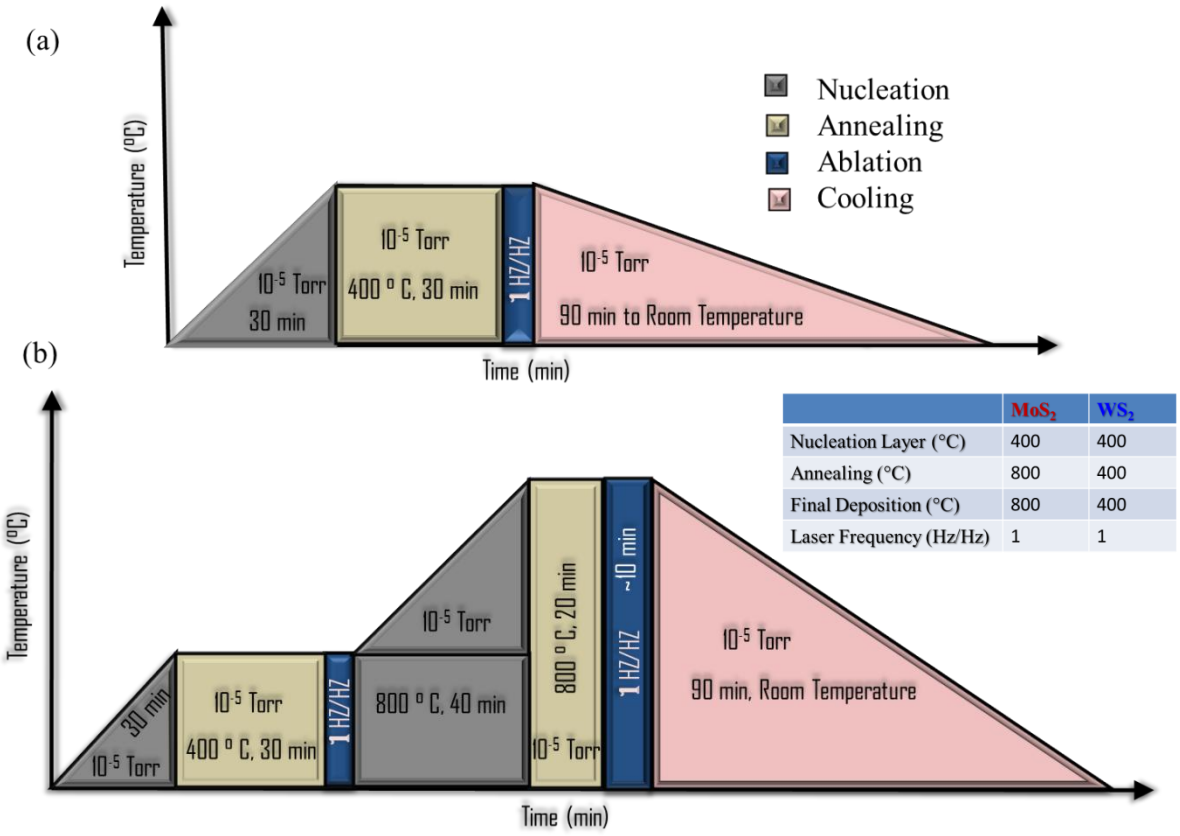

	MoS_2	WS_2
Nucleation Layer (°C)	400	400
Annealing (°C)	800	400
Final Deposition (°C)	800	400
Laser Frequency (Hz/Hz)	1	1

Figure 6.2 (a) & (b) schematic diagram shows PLD growth schedule for WS_2 and MoS_2. The final temperature for WS_2 is 400°C whereas for MoS_2 800°C. The laser ablation frequency in both MoS_2 and WS_2 is 1Hz/Hz.

The modified three step growth for 2D transition metal dichalcogenides are schematically shown in the figure 6.2. We have changed the laser ablation frequency from 2Hz to 1Hz in both at nucleation and final stage of the growth for more relaxation of van der Waal layers. It is interesting to observe that the final temperature for both MoS_2 and WS_2 are not equal. We have discussed our experiences and understanding about the epitaxial growth of transition metal dichalcogenides like MoS_2 and WS_2 in chapter VII.

6.3 Poly-type phase transition

TMDs like MoS_2 and WS_2 undergo a qualitative phase transition from semiconducting state to metallic state which makes them an appropriate monolithic candidate for switchable device applications. The electronic structure of both 2H MoS_2 and 1T MoS_2 undergo ligand field splitting experienced by Mo 4d in the trigonal-prismatic and octahedral environment, respectively (figure 6.3(e) & (f)) [13]. 1T phase is metallic and 2H shows semiconducting state.

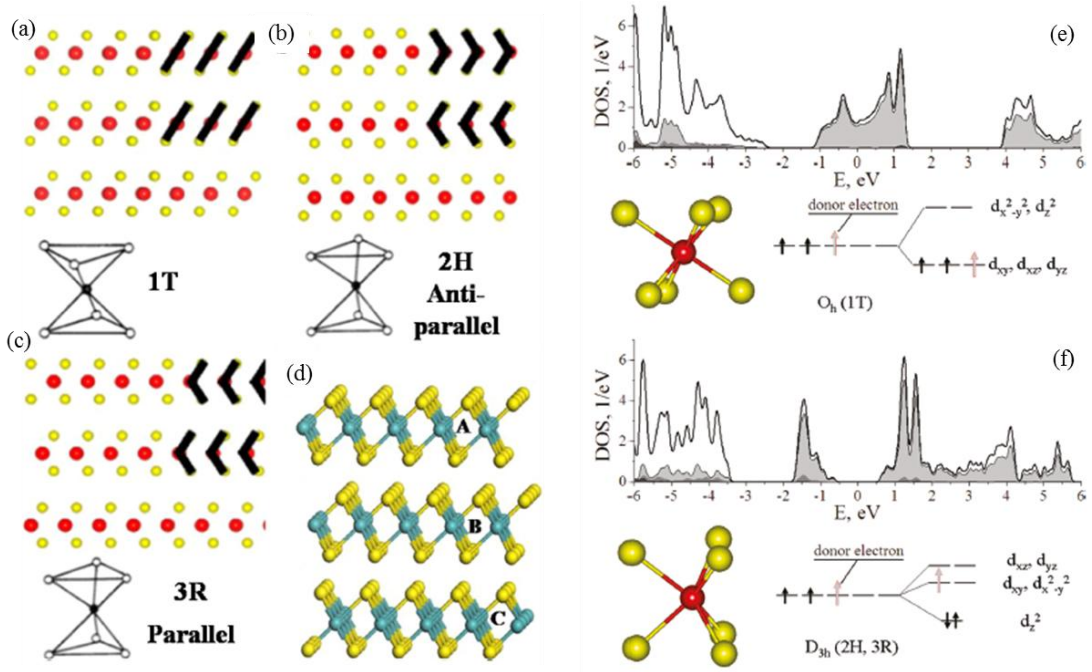

Figure 6.3 (a)-(d) Schematic presentation of 1T, 2H and 3R phases of MoS_2. Copyright (2011) by American Chemical Society [13]. (e) and (f) show crystal field splitting of Mo d in octahedral (1T) and trigonal – prismatic (2H), and change in density of states from semiconducting 2H phase to metallic 1T phase. Copyright (2016) by Elsevier [14].

There are many attempts by different research groups all over the world to make complete control over this poly-type phase transition through alkali metal intercalation (Li/K) [14, 15-17], e – beam charging [18, 19] etc. but the drawback of these methods are instability at ambient condition. First of all, for device application one needs stable large scale materials which can't be possible in those methods. We have addressed this issue in a different way. In nature, ReS_2 is known to be in 2D Peierls distorted $1T_d$ structure and forms a chain like superstructure [20-22]. From theoretical prediction we have found incorporation of Mo and W atoms in the ReS_2 lattice modifies the metal-metal hybridization between the cations and influences the structural modulation and electronic property of the system described in the chapter VIII.

6.4 Over view of the thesis based on Part II

Chapter VII describes substrate induced tuning of compressive strain and phonon modes in large area MoS_2 and WS_2 van der Waals epitaxial thin films. The optimized growth conditions for epitaxial thin film growth of MoS_2 and WS_2 on c plane sapphire substrate are briefly described. Substrate induced strain is measured by both Raman spectroscopy and HRTEM. The change in the optical band gap of monolayer measured from PL due to strain and compared with density functional theory calculation.

Chapter VIII describes nature of low dimensional structural modulations and relative phase stability in $Re_xMo(W)_{1-x}S_2$ transition metal dichalcogenides alloys. Density functional theory calculation predicts a poly-type phase transition cross over at ~50 at.% of Mo and W in ReS_2 in both monolayer and bulk form, respectively. Experimentally three types of structural modulation ($1T_d$) observed for $Re_xMo_{1-x}S_2$ and only one type of modulation is observed for $Re_xW_{1-x}S_2$ alloy system. The 50% alloy system, i.e. $Re_{0.5}Mo_{0.5}S_2$ and $Re_{0.5}W_{0.5}S_2$ are found to be a suitable monolithic candidate for metal semiconductor transition with minute external perturbation.

6.5 Bibliography

[1] A. K. Geim, I. V. Grigorieva, Nature **499**, 419–425(2013).

[2] K. F. Mak, C. Lee, J. Hone, J. Shan, T. F. Heinz, Phys. Rev. Lett. **105**, 136805 (2010).

[3] B. Radisavljevic, A. Radenovic, J. Brivio, V. Giacometti, A. Kis, Nat. Nanotech. **6**, 147-150 (2011).

[4] W. Liu, B. Lee, C. H. Naylor, H. Ee, J. Park, A. T. C. Johnson, R. Agarwal, Nano Lett. **16**, 1262-1269 (2016).

[5] Y. N. Gartstein, X. Li, C. Zhang, Phys. Rev. Lett. **92**, 075445 (2015).

[6] K. F. Mark, J. Shan, Nat. Photonics **10**, 216-226 (2016).

[7] A. M Jones, H. Yu, N. J Ghimire, S. Wu, G. Aivazian, J. S Ross, B. Zhao, J. Yan, D. G Mandrus, Di Xiao, W. Yao, X. Xu, Nat. Nanotech. **8**, 634-638 (2013).

[8] K. F. Mak , K. He, J. Shan, T. F. Heinz, Nat. Nanotech. **7**, 494-498 (2012).

[9] H. Zeng, J. Dai, W. Yao D. Xiao, X. Cui, Nat. Nanotech. **7**, 490-493 (2012).

[10] F. Rose, M. O. Goerbig, F. Pi ´ echon ´, Phys. Rev. Lett. **88**, 125438 (2013).

[11] J. Jeon, S. K. Jang, S. M. Jeon, G. Yoo, Y. H. Jang, J. H. Park, S. Lee, Nanoscale **7**, 1688-1695 (2015).

[12] Y. H. Lee, X. Q. Zhang, W. Zhang, M. T. Chang, C. T. Lin, K. D. Chang, Y. C. Yu, J. T. W. Wang, C. S. Chang, L. J. Li, T. W. Lin, Adv. Mater. **24**, 2320 (2012).

[13] L. Houben, A. N. Enyashin, Y. Feldman, R. Rosentsveig, D. G. Stroppa, M. Bar-Sadan, J. phys. Chem. C **116**, 24350-24357 (2012).

[14] Z. He, W. Que, Appl. Mater. Today **3**, 23-56 (2016).

[15] A. Andersen, S. M. Kathmann, M. A. Lilga, K. O. Albrecht, R. T. Hallen, D. Mei, J. Phys. Chem. C **116**, 1826–1832 (2012).

[16] X. Rocquefelte, F. Boucher, P. Gressier, G. Ouvrard, P. Blaha, K. Schwarz, Phys. Rev. B **62**, 2397 (2000).

[17] L. Wang, Z. Xu, W. Wang, X. Bai, J. Am. Chem. Soc. **136**, 6693–6697 (2014).

[18] E. Sutter, Y. Huang, H. P. Komsa, M. Ghorbani-Asl, A.V. Krasheninnikov, P. Sutter, Nano Lett. **16**, 4410−4416 (2016).

[19] S. Han, Y. Park, Y. H. Hwang, S. Jekal, M. Kang, W. G. Lee, W. Yang, G. Lee, S. Hong, Sci. Rep. **6**, 38730 (2016).

[20] S. Tongay, H. Sahin, C. Ko, A. Luce, W. Fan, K. Liu, J. Zhou, Ying-Sheng Huang, Ching-Hwa Ho, J. Yan, D. F. Ogletree, S. Aloni, J. Ji, S. Li , J. Li , F. M. Peeters, J. Wu, Nat. Comm. **5**, 353 (2014).

[21] Z. G. Yu, Y. Cai, Y. Zhang, Sci. Rep. 5, 13783 (2015).

[22] Y. Lin, H. Komsa, C. Yeh, T. BjÖrkman, Z. Liang, C. Ho, Y. Huang, P. Chiu, A. V. Krasheninnikov, K. Suenaga, ACS Nano **9**, 11249–11257 (2015).

Chapter VII

Substrate induced tuning of compressive strain and phonon modes in large area MoS_2 and WS_2 van der Waals epitaxial thin films

Large area MoS_2 and WS_2 van der Waals epitaxial thin films with complete control over number of layers including monolayer is grown by pulsed laser deposition utilizing slower growth kinetics. The films grown on c-plane sapphire show stiffening of A_{1g} and E^1_{2g} phonon modes with decreasing number of layers for both MoS_2 and WS_2. The observed stiffening translate into the compressive strain of 0.52 % & 0.53 % with accompanying increase in fundamental direct band gap to 1.74 and 1.68 eV for monolayer MoS_2 and WS_2, respectively. The strain decays with the number of layers. HRTEM imaging directly reveals the nature of atomic registry of van der Waals layers with the substrate and the associated compressive strain. The results demonstrate a practical route to stabilize and engineer strain for this class of material over large area device fabrication.

This work has been published in Journal of Crystal Growth ***121,*** *105101 (2017).*

7.1 Introduction

Atomically thick two dimensional layer materials generated immense research interest since the discovery of graphene [1-6]. Graphene revealed many unique physical phenomena e.g., linear band structure with momentum, ballistic transport [7-10] and superior chemical catalytic activities etc. [11, 12]. However, graphene is a zero band gap material and the need to open a band gap for practical device application shifted the attention towards MoS_2, WS_2 and similar materials belonging to the family of layered transition metal dichalcogenides (TMDs) [13, 14]. Most of them exhibit indirect to direct band gap crossover from bulk to monolayer form and promising for extremely thin transistors, exploring fundamental physics, and energy related applications. Most of the fundamental properties based on this system are investigated primarily on mechanically exfoliated and chemically synthesized materials [15-19] that are not suitable for large area practical device fabrication. There have been many attempts to grow such van der Waals materials epitaxially over large area and explore the tuning of electronic structure through the application of strain [16-27]. Most of the epitaxial layer growth reported was only in the na-no or micrometer length scale along with special treatment of substrate and the application of strain was performed by external means. For example, large area CVD growth of MoS_2 thin films was reported on SiO_2 substrate [18, 28]. Control over the number of layers was achieved by the duration of oxygen plasma treatment of SiO_2 substrate. Oxygen plasma treatment was believed to increase the interaction between the MoS_2 and SiO_2 substrate and helps in further growth of subsequent layers [28]. The characteristics Raman mode are different for the thin films grown on the substrate compared to the bulk suggesting the substrate induced van der Waals and long range Coulomb interaction. Most of the reports show softening of the Raman modes upon decreasing the number of layers grown on the widely used SiO_2 substrate. Among various reports on the tuning of electronic structure by strain is one where externally applied uniaxial tensile strain on a fabricated MoS_2 bending device resulted in phonon mode softening. This phonon mode softening was associated with the decrease in band gap by ~45 meV and ~120 meV for every 1% of strain for monolayer and bi-layers, respectively. Direct to indirect crossover occurs for monolayer MoS_2 with applied strain of 1% [29]. On the other hand, application of bi-axial compressive strain was shown to increase the band gap of MoS_2 monolayer and the change in band gap is within 100 meV for every 1% of strain [30]. Nevertheless, from practical point of view it is important to grow such layered compounds epitaxially over large area with complete control over the layer thickness and at the same time inducing strain through the substrate in order to retain the modification in the electronic structure. Both the aspects of large area (we have grown on maximum 8×8 mm^2 size substrate) epitaxial

film growth and retaining strained state are demanding and challenging. With this goal, in the present report we first demonstrate that it is possible to grow epitaxial MoS_2 and WS_2 thin films by pulsed laser deposition (PLD) under slow kinetic condition on '*c*' plane sapphire substrate [31], which has some advantages over the CVD counterpart. Moreover, complete control over layer thickness is possible by this method including the growth of monolayer without requiring any special substrate treatment. An important second part of the results is that the sapphire substrate significantly influences the two important Raman modes i.e. A_{1g} and E^1_{2g} in MoS_2 and WS_2 epitaxial thin film grown by PLD. We have observed significant stiffening of two Raman active modes i.e. A_{1g} and E^1_{2g} for MoS_2 thin film and mostly A_{1g} for WS_2 and the two modes stiffens further with decreasing layer thickness. This translates to a maximum compressive strain of 0.52 % & 0.53 %, increases the band gap to 1.73 eV and 1.68 eV for monolayer MoS_2 and WS_2, respectively, and falls off with increasing the layer thickness. The HRTEM imaging from the interface directly reveals the nature of atomic registry and strain between the films and substrate. The overall results are extremely encouraging and show a practical route to engineer the phonon modes and retain the strain in such van der Waals compounds, which can be exploited to tune the opto-electronic properties and fabrication of large area practical devices.

7.2 Experimental method

Thin films of MoS_2 and WS_2 are grown by pulsed laser deposition (PLD) on '*c*' plane sapphire. We have used 8 sq. mm size of substrate for the present study but little bigger substrate can also be used in our system. MoS_2 and WS_2 target pellets were prepared from powders obtained from Sigma Aldrich (99.9%) by first cold pressing and then sintering at 500 °C for 5 hours in a vacuum chamber (~10^{-5} Torr). The sintering under large vacuum chambers with continuously running pumps prevents oxidation of compounds as well as re-deposition of vapor species back on the pellet surface compared to sintering performed in a sealed quartz tube. This was a successful method for system containing highly volatile elements [32, 33]. The growth was followed by three-step process originally developed for ZnO but with a different temperature and kinetic settings [31]. The temperature for nucleation layer was 400 °C with a laser ablation rate of 1 Hz. The temperature for final growth was 800 °C and at 1Hz laser ablation rate. Both the nucleation layer and slower laser frequency rate are important to obtain epitaxial large area film as we found that faster laser ablation rate leads to formation of polycrystalline MoS_2 films. As already explained, previously this slow laser ablation rate allows sufficient time for kinetic relaxation of the nucleation layer in order to establish epitaxial

relationship with the substrate thus removing misaligned crystallites. This is even more important for van der Waals compounds because the 2D-nucleations do not have any strong attachment with the underlying substrate and is relatively more mobile during the deposition compared to non-layered or three-dimensional covalently bonded materials. The method described above was successful for the epitaxial growth of ZnO alloyed with Co, Mn, S and Te on sapphire [31-34]. The pressure was kept constant at ~10^{-5} Torr throughout the growth schedule. There are few recent reports on using sapphire substrate for growing TMDs films [35-37].

The PLD method of growth has some benefits over chemical vapor deposition (CVD) or physical vapor deposition (PVD) counterparts in the sense that the films will be free from any parasitic deposition. Moreover, the technique is economical and scalable even on a larger substrate than mentioned here in the present study [38, 39].

The epitaxial quality of thin films are confirmed by X-ray diffraction, high-resolution transmission electron microscopy and electron diffraction techniques. TEM cross sectional samples were prepared by, first mechanical polishing and then Ar^+ ion milling to perforation in order to generate large electron transparent thin area. Special care was taken during the sample preparation as it was found that van der Waals layers could easily be detached from the substrate. The relative movement between two cross sectional pieces was made almost absent to ensure their presence on the substrate until the end of sample preparation. Raman spectra were recorded using a custom-built Raman spectrometer using a 532 nm laser excitation and a grating of 1800 lines/mm at room temperature [40]. The laser power at the sample was approximately 1 mW. Micro PL (photoluminescence) measurement was performed in a state of the art LabRAM HR (UV) system.

7.3 Theoretical calculation

We have used density functional theory calculation based on WIEN2k code [41] to evaluate the change in electronic structure and band gap of both MoS_2 and WS_2 monolayer corresponding to the experimentally observed in-plane compressive strain. Generalized gradient approximation (GGA) was performed with Perdew-Burke-Ernzerhof (PBE) functional for optimization of lattice parameters and minimization of forces. The optimized lattice parameters are a = 3.192 & 3.168 Å for MoS_2 and WS_2 monolayer, respectively. A k-mesh of 19×19×2 for the integration of Brillouin zone and spin orbit coupling was incorporated in this calculation.

7.4 Results and Discussion

7.4.1 Epitaxial growth of MoS_2 and WS_2 thin films: HRTEM & thin film XRD

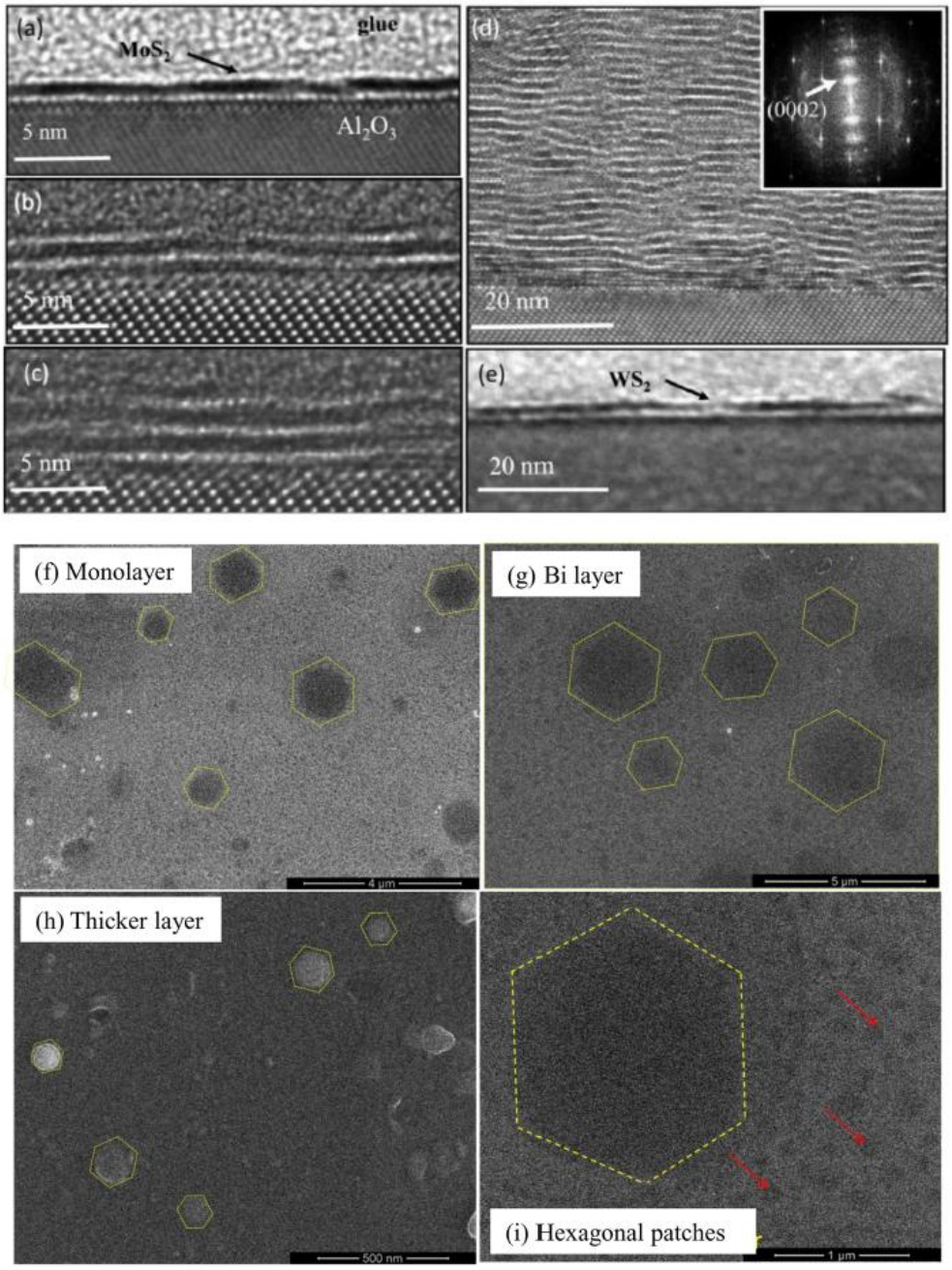

Figure 7.1 HRTEM images showing (a) monolayer, (b) bi-layers, (c) few layers, and (d) thick epitaxial films of MoS_2 on 'c' plane sapphire. Epitaxial monolayer WS_2 on 'c' plane sapphire is shown in (e). Both the electron diffraction and X-ray spectra confirm the formation of large area epitaxial thin film on sapphire. X-ray spectra are shown in figure 7.2. (f)-(g) are SEM images of hexagonal geometry of TMDs.

We have used HRTEM imaging to confirm the formation of epitaxial film, number of layers and stacking information in addition to routinely practiced Raman spectroscopy. On the other hand, X-ray signal does not show up from such one or two layers of films, while spectra from the thick films confirms the formation of large area epitaxial film on sapphire substrate. Hexagonal domains are clearly visible in SEM images shown in 7.1. TEM is extremely powerful technique and can provide information from 40-50 µm length scale considering four quadrants of the thin areas in a cross sectional TEM specimen. As already mentioned in the TEM sample preparation method, special care must be undertaken during sample preparation in order to retain the weakly held van der Waals layers on the substrate until the end. Figure 7.1(a)-(e) displays the example HRTEM images with various numbers of layers for MoS_2 films and monolayer WS_2 film. Both the electron diffraction pattern and FFT of HRTEM images are placed in the inset for the thick films. From SEM images (figure 7.1 (f)-(g)), it is clearly visible that the hexagonal geometry is preferable depending on chemical potential of sulpher. Diffraction pattern shows <0002> spots parallel to the growth direction. Aberration corrected negative C_S imaging at the interface regions is carried out to probe the nature of layer bonding with the substrate, strain and interlayer stacking information (figure 7.5) [42, 43].

X-ray spectra confirming the formation of large area epitaxial MoS_2 thin film on '*c*' plane sapphire. (0002) and (0006) peaks corresponding to MoS_2 and Al_2O_3 are marked. For monolayer and bi-layers, it was not possible to obtain a clear signal by X-ray. The reason for this is that for coherent Bragg X-ray diffraction at least few numbers of layers is required to obtain any out of plane peaks.

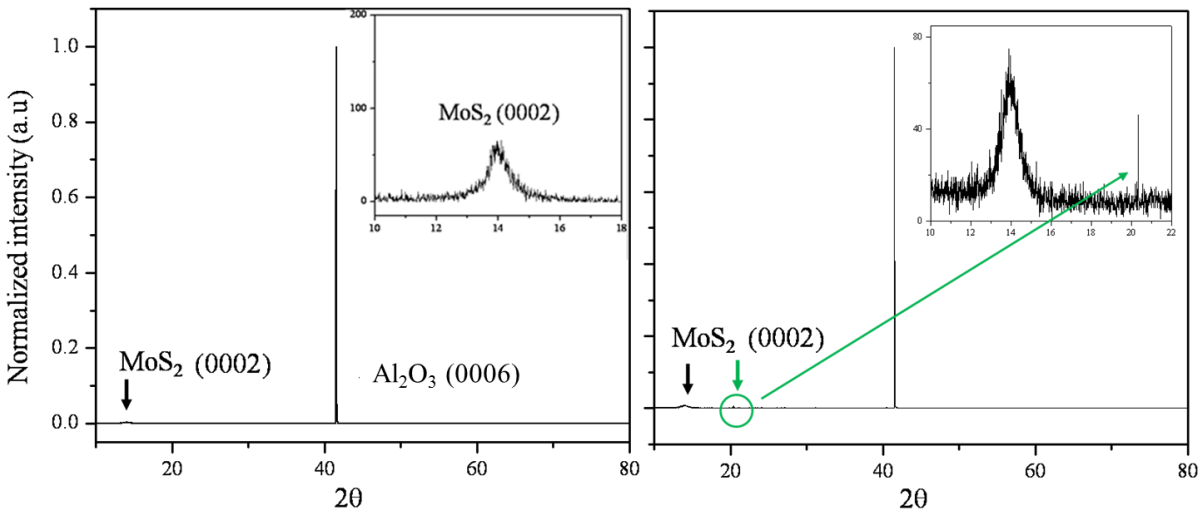

Figure 7.2 Thin film X-ray diffraction shows (a) epitaxial and (b) Polly crystalline thin film.

We have observed X-ray diffraction for faster laser ablation (right panel) and found extra peaks besides (0002). Example extra peak is marked in green circle in the right figure. This peak might be for different orientation grain. The FWHM of (0002) for slower rate was 0.93135 and for faster rate is 0.96315.

For the thick film the stacking structure of MoS_2 and WS_2 are of 2H poly-type. It can be seen that the sapphire substrate is Al terminated and at the end it will be explained that the interaction between the periodic dangling bonds at Al atoms and bottom S layers of MoS_2/WS_2 is responsible for the substrate induced compressive strain and associated phonon mode hardening. Extended lattice defects are observed for the thick films and their nature and influence on the physical properties will be the topic of a separate paper.

7.4.2 Substrate induced layer specific stiffening in E^1_{2g} and A_{1g} Raman modes

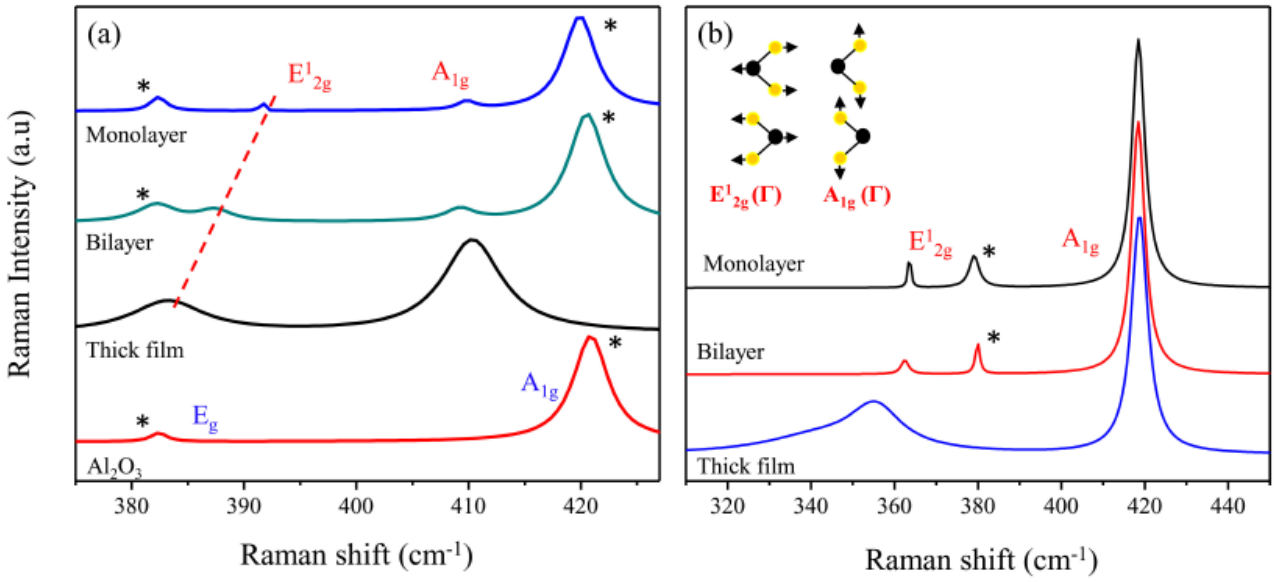

Figure 7.3 The A_{1g} and E^1_{2g} Raman modes for monolayer, bi-layer and thick films for (a) MoS_2, and (b) WS_2. For comparison the Raman modes of bare sapphire is also shown in (a). Raman shift for bulk powder from literature is shown in figure 7.4. The inset of (b) shows the atomic displacements of the Raman modes. Peaks marked with the asterisks are from sapphire substrate.

Figure 7.3 shows E^1_{2g} and A_{1g} Raman modes of both MoS_2 and WS_2 for different layer thickness. Hardening of E^1_{2g} and A_{1g} Raman modes indicates the presence of compressive strain

[44]. We have observed substrate induced compressive strain in both MoS_2 and WS_2 layers with the maximum strain present for the monolayer and the strain decreases with increasing the number of layers. Other than stiffening, systematic anomalous shift in the Raman modes are also observed as the number of layers is decreased which is consistent with the earlier reports [26]. Figure 7.4 summarizes the shift in E^1_{2g} and A_{1g} Raman modes of MoS_2 and WS_2 as a function of film thickness grown on '*c*' plane sapphire and further information are tabulated. The frequency of these two phonon modes for bulk starting powder samples used to grow films in our case and the values from the literature are also listed for the comparison purpose [26]. The Raman shifts of these two modes are slightly different for the powder sample (379.93and 405.71 cm^{-1}, Sigma Aldrich) used for the present investigation in comparison to the literature values (379.21 and 404.71 cm^{-1}) [26].

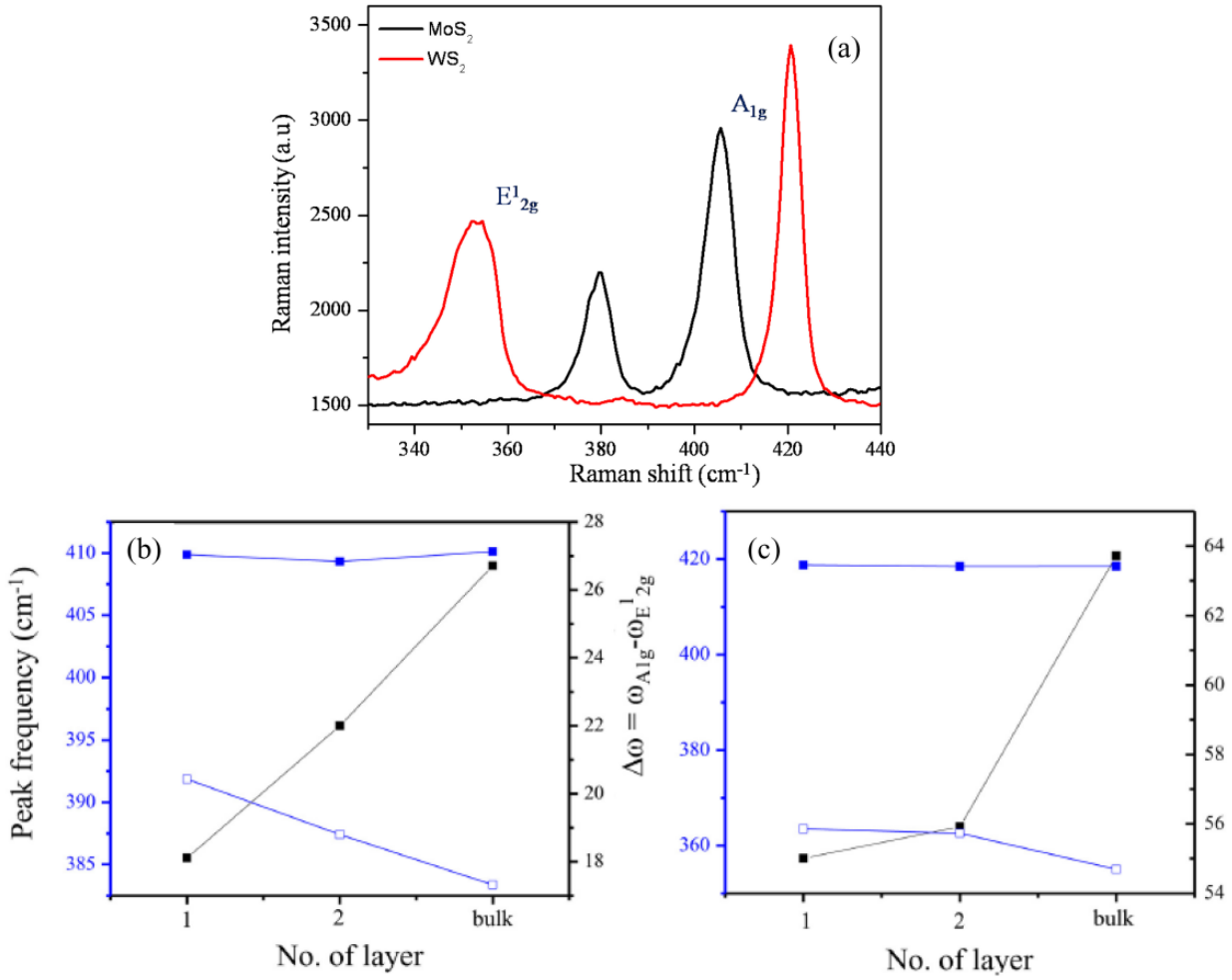

Figure 7.4 (a) Shows Raman peaks for bulk powder. Raman shifts of A_{1g} and E^1_{2g} modes for monolayer, bi-layers and thick films for (b) MoS_2 and (c) WS_2, showing stiffening due to compressive strain with decreasing number of layers. The difference between the A_{1g} and E^1_{2g} peaks showing anomalous peak shift with decreasing number of layers is also plotted (blue).

The difference between the two modes ($\Delta = A_{1g}$-E_{2g}) for the above mentioned two different samples are 25.78 and 25.5 cm^{-1}, respectively, and almost close to each other. The difference in absolute values of these two modes between the present powder and the bulk samples may be due to the morphological effect, as powders are composed of particles, which are hundreds of microns in size compared to the flat finite size few layer bulk samples reported in the literature. The thicker MoS_2 film grown in our case (~ 100 nm or ~ 140-150 number of layers) has the E^1_{2g} and A_{1g} values as 383.37 and 410.13 cm^{-1} with $\Delta = 26.76$. The absolute values are almost close to the literature [26] reported multilayer values except slightly larger Δ may be because of large number of layers over large areas (at least 8×8 sq. mm) compared to the previous reports (figure 7.4).

This possibly introduces stronger long range Coulomb force compared to the micrometer sized bulk powder, softens the E^1_{2g} mode further, and consequently increases the band gap. The frequency values shifts to the higher wave numbers or stiffens with decreasing the number of layers as seen for the Raman shift of E and A modes in MoS_2 with shifts for monolayer/bi-layer being 391.77/387.32 and 409.88/409.32 cm^{-1} (figure 7.3 (a)). The difference between the Raman shifts of the two modes, Δ is 18.11 and 21.9 compared to the reported values of 17.18 and 21.4 cm^{-1}, respectively for monolayer and bi-layer [26]. All these Raman modes are listed in the table 7.1.

(a)

MoS_2	E^1_{2g}	A_{1g}	Δ	Comp.strain w.r.t literature	Comp.strain w.r.t thick film	Band gap (eV)
Thick Film	383.37	410.13	26.71			
Bi layer	387.42	409.32	22	0.27%	0.28%	1.4
Mono layer	391.77	409.88	18.11	0.51%	0.52%	1.736
Literature (bulk)	383.48	408.23	24.75			

(b)

WS_2	E^1_{2g}	A_{1g}	Δ	Comp.strain w.r.t literature	Comp.strain w.r.t thick film	Band gap (eV)
Thick Film	355.04	418.76	63.72			
Bi layer	362.56	418.48	55.92	0.44%	0.47%	
Mono layer	363.39	418.5	56.11	0.49%	0.53%	1.678
Literature (bulk)	355.5	420.5	65			

Table 7.1 (a) and (b) show Raman peak frequency, strain and theoretical band gap of MoS_2 and WS_2.

Thus, Raman spectroscopy also confirms the formation of monolayer and bi-layers MoS_2 large area epitaxial thin film in the present case in addition to TEM imaging. We also observe anomaly in the

shifts in two Raman modes for MoS_2 films on sapphire substrate with number of layers as reported earlier except E^1_{2g} mode. In our case stiffens significantly from 383.37 in the thick film to 387.32 and 391.77 cm^{-1} for the bi-layers and monolayer, respectively whereas A_{1g} mode softens from 410.13 for the thick film to 409.88 for the monolayer. For monolayer, the difference in the two Raman modes between literature and the present case is 3.92 and 2.49 for the E^1_{2g} and A_{1g} modes, respectively [26]. This difference in Raman modes translates into equivalent compressive strain of 0.52 % in the monolayer film on sapphire substrate.

7.4.3 Band gap: PL & DFT

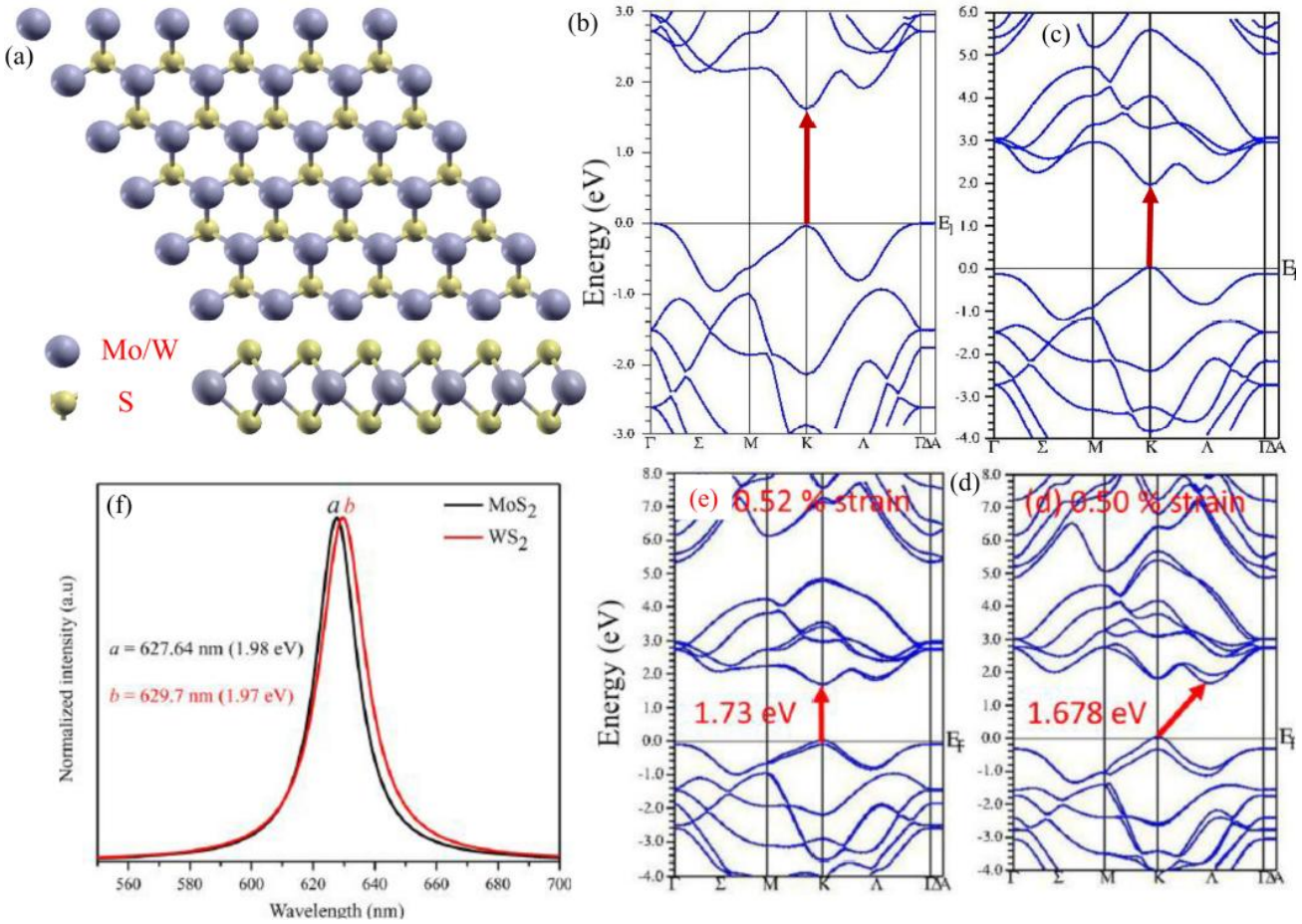

Figure 7.5 (a) Schematic of monolayer of MoS_2/WS_2. (b)& (c) are calculated band structure monolayer of MoS_2 and WS_2. (d) & (e) are the calculated band structure corresponding to the experimentally observed strain. The direct band gap of MoS_2 increases and remains fundamental, but for similar magnitude of compressive strain WS_2 shows emergence of cross over from direct to indirect band gap. (f) Photoluminescence spectra of monolayer MoS_2 and WS_2 epitaxial thin film on 'c' plane sapphire.

To best of our knowledge, this is the only report on the substrate-induced strain and its retention and this is important for tuning of optoelectronic property of such material in an effective and efficient way. It has already been predicted that introducing compressive stress will increase the band gap of the system. The change in band gap is expected to be 1.73 eV (1.68 eV without strain in PBE-GGA) for the monolayer MoS_2 (figure 7.5). The corresponding indirect band gap also increases from 1.88 eV to 1.93 eV. The origin of strain based on HRTEM imaging is discussed in the subsequent section.

PL spectra shows clear emission at 1.98 eV from monolayer film but no clear signal is obtained from bi-layer and thick films suggesting that monolayer property is retained on sapphire substrate but crossover takes place after depositing subsequent layers on top of monolayer (figure 6.5 (g)).

For WS_2 it is already reported that the A_{1g} (Γ) mode stiffens with increasing the number of layers which is similar to the behavior of MoS_2. This stiffening of A_{1g} mode is due to the increase in restoring force caused by band renormalization through interlayer Coulomb coupling and van der Waals interaction [45]. On the other hand, the E^1_{2g} phonon mode shows only subtle changes with the number of layers. The bulk WS_2 micron size powders used in our case shows frequency corresponding to E^1_{2g} and A_{1g} as 352.63 and 420.5 cm^{-1}, respectively and the values reported in the literature are 355.5 and 420.5 cm^{-1} [46] with Δ being 67.87 and 65 cm^{-1}, respectively. WS_2 thin films grown on sapphire substrate do not show any significant changes in the frequency of A_{1g} mode, but E^1_{2g} mode is observed to harden significantly on decreasing the number of layers with the shifts being 363.5 and 362.56 cm^{-1} with Δ = 55 and 55.92 for monolayer and bi-layer, respectively. This is significantly different from reported values for monolayer i.e. 355.9 and 417.5 cm^{-1}, with a frequency difference 61.6 cm^{-1}. This shows the significant influence of sapphire substrate on the WS_2 layer. This difference in Raman modes translates into an equivalent compressive strain of 0.53 % in the monolayer film on sapphire substrate. The band gaps of monolayer WS_2 are 1.68 for direct. However, with 0.53 % compressive strain it is at the edge of cross over from direct (1.682 eV) to indirect (1.678 eV) band gaps (figure 6.5). Clear PL emission peak at 1.97 eV is obtained in the case of monolayer WS_2 as well and the state of the material at the edge of crossover did not disturb the probability of emission across the direct band gap. The situation is different from the case of MoS_2 where crossover is expected to take place at a compressive strain of ~ 2% [47]. This is because the rate of change of both types of band gaps with compressive strain is different for WS_2 and MoS_2. The band gap modification in both the cases can be understood in terms of coupling between various S and Mo valence orbital [47].

Few reports exist on the stiffening of the Raman modes and associated increase in compressive strain [22, 27, and 29]. In previous reports, strain was applied by external means. However, in our case the strain is induced by substrate and can be retained which will be useful for practical device engineering of this material. The origin and nature of this substrate-induced strain is discussed next.

7.4.4 Nature of substrate induced strain and interlayer stacking

It is interesting that though both MoS_2 and WS_2 are van der Waals compounds, sapphire substrate is capable of inducing compressive strain in this material. Generally, van der Waals interaction is comparatively very weak compared to usual ionic or covalent chemical bonding and for this force, it may seem difficult to sustain the strain. However, the theoretical calculation for 0.52% compressive strain corresponding to monolayer MoS_2 shows that the strain energy cost is only 10 meV, which is much lower compared to interlayer van der Waals force of 460 meV for MoS_2. This increases the band gap to 1.74 eV from 1.68 eV obtained using PBE-GGA potential based calculation and a value of 1.98 eV obtained by PL measurement. This implies that, there must be weak interaction existing between MoS_2 and the underlying substrate. Negative C_s HRTEM imaging directly reveals the interfacial structure of both MoS_2 and sapphire. We present only results based on MoS_2 and similar result can be expected for WS_2. Figure 7.6 shows the atomic resolution interface image of MoS_2 on '*c*' plane sapphire. MoS_2 has following orientation relationship with sapphire substrate i.e. $\underline{<11\text{-}20>Al_2O_3}$ || $\underline{<01\text{-}10>\ MoS_2}$. The schematic model is shown in Figure 7.5 (d) and a strain of 1.11±0.43 and 0.74±0.33 % can be derived for the first and second layer, respectively from the image. From the HRTEM images, layer specific variation of compressive strain has been estimated averaging over 15 atoms at different regions. The strain derived from HRTEM images are different from the strain derived from the Raman spectra i.e. 0.52 and 0.25 % for monolayer and bi-layers, respectively. The possible discrepancy between Raman and HRTEM could be very small area (nanometers) information probed by HRTEM compared to large area (microns) probed by Raman spectroscopy.

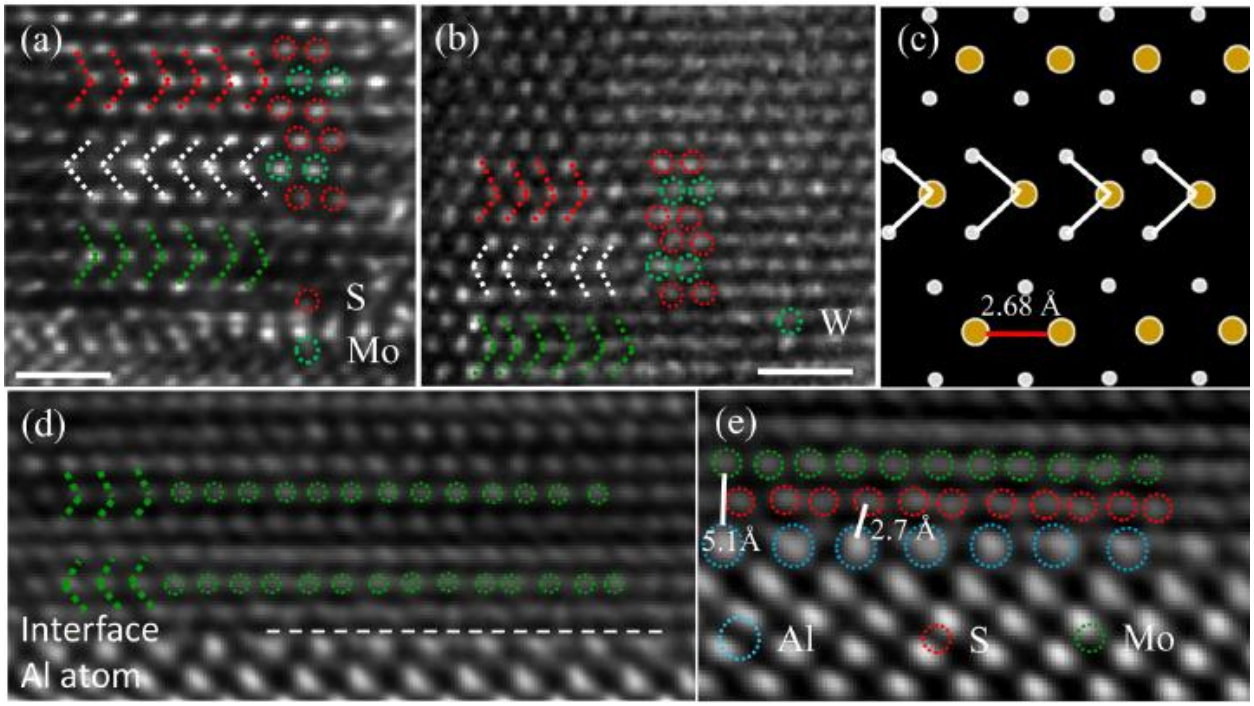

Figure 7.6 HRTEM imaging from the interface regions of epitaxial MoS_2 and WS_2 films along <11-20> Z.A. of sapphire. (a) & (b) showing the 2H poly-type interlayer stacking for MoS2 and WS_2, respectively. (d) Example image from MoS_2/sapphire interface markings atoms over a distance from place to place to derive strain information from such images. (e) Close up interface image showing that substrate is Al terminated and the typical distance between Al and S is ~ 2.7 Å. A modulated in plane S-S (marked with red dotted circle) inter-atomic distance over Al (marked turquoise dotted circle) atoms can be observed.

Strain can also be in-homogenously distributed in the films. Strain fades gradually as one goes away from the film-substrate interface along the '*c*' direction. From the HRTEM imaging it is found that this interaction also translates to the third layer and beyond and reduces with the thickness of the film. The interlayer stacking is found to be Bernal stacking (2H poly-type, figure 7.6(a)-(c)). Earlier reports mentioned about wide range of miss-oriented domains of MoS_2 grown epitaxially on a substrate and this was explained based on subtle difference in energies between different orientations [35, 36]. However, in our case both by HRTEM and X-ray only one type of oriented grains are observed probably due to the slower kinetics employed [31]. Nevertheless, question remains regarding the role of substrate and its polarity on the band gap of such material. In this context, it was already

shown theoretically that O dangling bond affects most among various dangling bonds in MoS_2 thin films on SiO_2 substrate [48]. O dangling bonds reduces the indirect band gap for both the monolayer and multi layers films significantly compared to direct band gap but for Si- terminated surface or H-passivated surface, changes are subtle and direct band gap remains fundamental. Thus, as it is clear from the HRTEM imaging that in the present case the substrate is Al- terminated and it is the interaction between Al dangling bonds and S, which introduces the strain in these films. Based on the recent theoretical results in Ref. 49, Al terminated sapphire substrate influences the electronic structure of MoS_2 only weakly. The experimental Al-S distance is found to be ~2.7 Å that is almost close to 2.6 Å predicted by theory [49].

The theoretical calculation also shows that MoS_2 can grow on sapphire with different degree of misorientation due to small energy difference between them. From our HRTEM imaging at the interface it is clearly visible that pairing of two S atoms around the Al atoms due to strain (figure 6.6 (e)). Therefore, in the presence of compressive strain the difference between the direct and indirect gaps will increase as expected and remain suitable for practical device exploration and application.

7.5 Conclusions

In summary, we have grown large area epitaxial thin films of van der Waals compounds MoS_2 and WS_2 on '*c*' plane sapphire by pulsed laser deposition with control over the number of layers. Substrates induced compressive strain is responsible for the stiffening of both the Raman modes with implication in increase in the direct band gap of these materials and their retention. The results demonstrate a practical way to engineer the optoelectronic property of such materials for large area device fabrication and application.

7.6 Bibliography

[1] A. K. Geim, K. S. Novoselov, Nat. Mater. **6**, 183−191 (2007).

[2] A. K. Geim, I. V. Grigorieva, Nature **499**, 420 (2013).

[3] C. N. R. Rao, A. K. Sood, R. Voggu, K. S. Subrahmanyam, J. Phys. Chem. Lett. **1**, 572–580 (2010).

[4] P. Vogt, P. De Padova, C. Quaresima, J. Avila, E. Frantzeskakis, M. C. Asensio, A. Resta, B. D. Ealet, G. L. Lay, Phys. Rev. Lett. **108**, 155501 (2012).

[5] Y. Xu, B. Yan, H. Zhang, J. Wang, G. Xu, P. Tang, W. Duan, S. Zhang, Phys. Rev. Lett. **111**, 136804 (2013).

[6] E. Bianco, S. Butler, S. Jiang, O. D. Restrepo, W. Windl, J. D. Goldberger, ACS Nano **7**, 4414-4421 (2013).

[7] K. S. Novoselov, A. K. Geim, S. V. Morozov, D. Jiang, M. I. Katsnelson, I. V. Grigorieva, S. V. Dubonos. A. A. Firsov. Nature **483**, 197- 200 (2005).

[8] S. D. Sarma, S. Adam, E. H. Hwang, E. Rossi, Rev. Mod. Phys. **83,** 407-470 (2011).

[9] K. S. Novoselov, A. K. Geim, S.V. Morozov, D. Jiang, Y. Zhang, S. V. Dubonos, I. V. Grigorieva, A. A. Firsov, Science **306**, 666-669 (2004).

[10] Y. Zhang, Y. Tan, H. Stormer, P. Kim, Nat. Lett. **438**, 201-203 (2005).

[11] L. Qu, Y. Liu, J. Baek, L. Dai, ACS Nano **4**, 1321-1326 (2010).

[12] K. S. Kim, Y. Zhao, H. Jang, S. Y. Lee, J. M. Kim, K. S. Kim, J. Ahn, P. Y. Jae-Young Choi, B. H. Hong, Nature **457**, 706-710 (2009).

[13] K. Fai Mak, C. Lee, J. Hone, J. Shan, T. F. Heinz, Phys. Rev. Lett. 105, 136805(4) (2010).

[14] M. Xu, T. Liang, M. Shi, H. Chen, Chem. Rev. **113**, 3766-3798 (2013).

[15] H. S. S. Ramakrishna Matte, A. Gomathi, Arun K. Manna, Dattatray J. Late, Ranjan Datta,Swapan K. Pati, C. N. R. Rao, Angew. Chem. **122**, 4153 –4156 (2010).

[16] Y. Zhan, Z. Liu, S. Najmaei, P. M. Ajayan, J. Lou, Small **8**, 966 (2012).

[17] N. Liu, P. Kim, J. H. Kim, J. H. Ye, S. Kim, C. J. Lee, ACS Nano **8**, 6902-6910 (2014).

[18] Y. H. Lee, X. Q. Zhang, W. Zhang, M. T. Chang, C. T. Lin, K. D. Chang, Y. C. Yu, J. T. W. Wang, C. S. Chang, L. J. Li, T. W. Lin, Adv. Mater. **24**, 2320 (2012).

[19] M. Okada, T. Sawazaki, K. Watanabe, T. Taniguch, H. Hibino, H. Shinohara, R. Kitaura, ACS Nano **8**, 273-8277 (2014).

[20] R. Browning, P. Padigi, R. Solanki, D. J. Tweet, P. Schuele, D. Evans, Mater. Res. Express 2, 0355006 (2015).

[21] K. He, C. Poole, K. F. Mak, J. Shan, Nano Lett. **13**, 2931 (2013).

[22] A. C. Gomez, R. Roldán, E. Cappelluti, M. Buscema, F. Guinea, H. S. J. van der Zant, G. A. Steele, Nano Lett. **13**, 5361 (2013).

[23] H. Pan, and Y. W. Zhang, J. Phys. Chem. C **116**, 11752 (2012).

[24] C. H. Chang, X. Fan, S. H. Lin, J. L. Kuo, Phys. Rev. B **88**, 195420 (2013).

[25] W. S. Yun, S. W. Han, S. C. Hong, I. G. Kim, J. D. Lee, Phys. Rev. B **85**, 033305 (2013).

[26] C. Rice, R. J. Young, R. Zan, and U. Bangert, D. Wolverson, T. Georgiou, R. Jalil, K. S. Novoselov Phys. Rev. B **87**, 081307(R) (2013).

[27] C. R. Zhu, G. Wang, B. L. Liu, X. Marie, X. F. Qiao, X. Zhang, X. X. Wu, H. Fan, P. H. Tan,T. Amand, B. Urbaszek, Phys. Rev. B **88**, 121301(R) (2013).

[28] J. Jeon, S. K. Jang, S. M. Jeon, G. Yoo, Y. H. Jang, J. H. Park, S. Lee, Nanoscale **7**, 1688-1695 (2015).

[29] H. J. Conley, B. Wng, J. I. Ziegler, R. F. Haglund, S. T. Pantelides, K. I. Bolotin, Nano Lett. **13**, 3626-3630 (2013).

[30] Y. Y. Hui, X. Liu, W. Jie, N. Y. Chan, J. Hao, Y. T. Hsu, L. J. Li, W. Guo, S. P. Lau, ACS Nano **8**, 7126-7131 (2013).

[31] B. Loukya, P. Sowjanya, K. Dileep, R. Shipra, S. Kanuri, L. S. Panchakarla, R. Datta, J. Crys. Growth **329**, 20-26 (2011).

[32] K. Dileep, R. Sahu, K. K. Nagaraja, R. Datta, J. Crys. Growth **402**, 124-129(2014).

[33] R. Sahu, K. Dileep, D. S. Negi, K. K. Nagaraja, S. Shetty, R. Datta, J. Crys. Growth **410**, 69-76 (2015).

[34] D. S. Negi, B. Loukya, K. Dileep, M. Kesaria, N. Kumar, R. Datta, Superlatt. Microstruct. **63**, 289-297 (2013).

[35] Q. Ji, M. Kan, Y. Zhang, Y. Guo, D. Ma, J. Shi, Q. Sun, Q. Chen, Y. Zhang, Z. Liu, Nano Lett. **15**, 198-205 (2015).

[36] D. Dumcenco, D. Ovchinnikov, K. Marinov, P. Lazi_c, M. Gibertini, N. Marzari, O. L. Sanchez, Y. Kung, D. Krasnozhon, M. Chen, S. Bertolazzi, P. Gillet, A. F. Morral, A. Radenovic, A. Kis, ACS Nano **4**, 4611-4620 (2015).

[37] C. R. Serrao, A. M. Diamond, S. Hsu, L. You, S. Gadgil, J. Clarkson, C. Carraro, R. Maboudian, R.; C. Hu, S. Salahuddin, Appl. Phys. Lett. **106**, 052101 (2015).

[38] J. A. Greera, M. D. Tabat, J. Vac. Sci. Technol. A **13**, 1175 (1995).

[39] M. Lorenz, H. Hochmuth, D. Natusch, H. Börner, G. Lippold, K. Kreher, W. Schmitz, Appl. Phys. Lett. **68,** 3332 (1996).

[40] G. V. P. Kumar, C. Narayana, Current Science. **93**, 778-781 (2007).

[41] P. Blaha, K. Schwarz, G. H. K. Madsen, D. Kvasnicka, J. Luitz, WIEN2k: *An Augmented Plane Wave + Local Orbitals Program for Calculating Crystal Properties* (Karlheinz Schwarz, Techn. Universität Wien, Austria, 2001).

[42] C. L. Jia, M. Lentzen, K. Urban, Science 299, 870 (2007).

[43] R. Datta, S. Kanuri, V. Karthik, D. Mazumdar, J. X. Ma, A. Gupta, Appl. Phys. Lett. **97**, 071907 (2010).

[44] Y. Yu Hui, X. Liu, W. Jie, N. Yui Chan, J. Hao, Y. Hsu, H. Li, W. Guo, S. P. Lau, ACS Nano **7,** 7126-7131 (2013).

[45] H. Zhong, S. Gao, J. Shi, L. Yang, Phys. Rev. B **92**, 115438 (2015).

[46] H. R. Gutiérrez, N. Perea-López, A. L. Elías, A. Berkdemir, B. Wang, R. Lv, F. López-Urías, V. H. Crespi, H. Terrones, M. Terrones, Nano Lett. **13**, 3447-3454 (2013).

[47] B. Amin, T. P. Kaloni, U. SchwingenschlÖgl, RSC Adv. **4**, 34561–34565 (2014).

[48] H. Sung, D. Choe, K. J. Chang, New J. Phys. **16**, 113055 (2014).

[49] A. K. Singh, R. G. Hennig, A. V. Davydov, A. Tavazza. Appl. Phys. Lett. **107**, 053106 (2015).

Chapter VIII

Nature of low dimensional structural modulations and relative phase stability in $Re_xMo(W)_{1-x}S_2$ transition metal dichalcogenide alloys

We report on the various types of Peierls like two dimensional structural modulations and relative phase stability of 2H and 1T poly-types in $Re_xMo_{1-x}S_2$ and $Re_xW_{1-x}S_2$ alloy system. Theoretical calculation predicts a poly-type phase transition cross over at ~50 at.% of Mo and W in ReS_2 in both monolayer and bulk form, respectively. Experimentally, two different types of structural modulations at 50% and a modulation corresponding to trimerization at 75% alloy composition is observed for $Re_xMo_{1-x}S_2$ and only one type of modulation is observed at 50% $Re_xW_{1-x}S_2$ alloy system. The 50% alloy system is found to be a suitable monolithic candidate for metal semiconductor transition with minute external perturbation.

This work has been published in Journal of Applied Physics ***121,*** *105101 (2017) (Featured article & front cover page).*

8.1 Introduction

Atomically thin transition metal dichalcogenides (TMDs) is considered to be the next generation platform for future electronics and offers numerous novel device applications based on its unique excitons, spin, and valley properties [1-11]. The most explored members in the family i.e. MoS_2 and WS_2 possess direct band gap in the monolayer form but undergoes transition to undesirable indirect band gap material for number of layers two and more [5, 12-13]. The stable crystal structure of MoS_2 and WS_2 is 2H (space group 194: $P6_3/mmc$) with a direct band gap of 1.88 and 1.9 eV, respectively for the monolayer. On the other hand for ReS_2, the band gap remains direct even in the bulk form due to weak interlayer van der Waals and electronic coupling [14]. The stable crystal structure of ReS_2 is 2D-Peierls distorted $1T_d$ (space group 2:$P\bar{1}$) where chains made of Re_4 clusters form the quasi two dimensional superstructures with a band gap of 1.55 eV for the monolayer. The metastable unmodulated 1T phase of MoS_2 is demanding due to its metallicity which is indispensable for carrier transport, injection and in the modulated $1T_d$ form shows excellent hydrogen evolution activity (HER) [15]. The most stable configuration in the modulated 1T form of MoS_2 and WS_2 is $2a\times a$ superstructure as in the case of ReS_2 [15-17]. These superstructures reported to have band gap of 0.1-0.2 eV and 0.14 eV, for MoS_2 and WS_2, respectively [15, 17]. Throughout the text '$1T_d$' is used to represent the chains like superstructure in all cases.

As already mentioned above, the 1T and modulated $1T_d$ poly-types of both MoS_2 and WS_2 are metastable. However, due to their useful properties various attempts have been made to stabilize these poly-type structural forms [18-21]. Most of the reports are based on intercalation method using alkali metals e.g., Li, and K where structural transitions between various poly-types take place during loading of alkali metals at the interlayer spacing with the end application as rechargeable batteries. Among various reports, Li and alkali metal intercalation was reported to stabilize the $1T_d$ form of both MoS_2 and WS_2 through hybridization between metals forming quasi 2D chain. Li intercalation of MoS_2 powders in water formed $2a\times2a$ superstructure as confirmed by X-ray diffraction [22]. On the other hand, K intercalation stabilizes two different form of modulated structure of MoS_2 depending on the K concentration i.e. trimerization of Mo with superstructure $(a\sqrt{3}\times a\sqrt{3})$ ($x \approx 0.3$) and tetramerization of Mo with superstructure $2a\times2a$ ($x \leq 0.3$) [23]. The presence of two different superstructures in this case was confirmed by scanning tunneling microscopy (STM) technique. Relative stability of various types of superstructure modulation in Li intercalated

MoS_2 i.e. $LiMoS_2$ was previously investigated by first principle calculations [24]. It was found that the ($2a\times2a$) superstructure formed by tetramerization of cations was more stable (by 0.5 eV) compared to trimerized ($a\sqrt{3} \times a\sqrt{3}$) structural modulation. This opened a band gap of about 1 eV. However, later studies based on both experimentation and theory revealed that it is $2a\times a$ type periodicity forming chains like structure the most stable modulated form of MoS_2 [16]. It was also pointed out that a charge density wave (CDW) phenomenon was at the origin of such structural modulation which was associated with a partially nested Fermi surface and the stabilization is localized around the Fermi level. The destabilization due to strain occurs mainly in the 3*p* of sulphur part which is compensated by electronic stabilization in the 3*d* of Molybdenum part. Though energetically least stable, however, the trimerized modulated structure was predicted to be the thinnest ferroelectric material [25]. There is a lot of interest in the community to understand and control various structural poly-types of monolayer TMDs by different means for their efficient utilization in energy, optoelectronics, and novel devices apart from immense interest in fundamental science [3-8, 26-29]. Among recent reports, intermediate steps of structural transition from trigonal prismatic 2H to octahedral 1T phase have been studied by electron microscopy [20]. Three different types of distortions or sub-superstructures are observed by HRTEM as transient states involving a shear mechanism. These are (2×1), (2×2) and ($\sqrt{3} \times 1$) and the combinations between them. The *d* electron system for various superstructures changes as follows, d^2 for 2×1 (zigzag clustering), $d^{3/4}$ for ($\sqrt{3} \times 1$) (ribbon chain clustering) and d^3 for 2×2 (diamond chain clustering). In another report, Li intercalated MoS_2 shows the presence of bi-phase structure i.e. both 2H and combination of 1T and $1T_d$ (2×1) [1]. Different structural phases form coherent interface at the boundary. The structure changes from $1T_d$ to 1T by e^- beam exposure. The transition from $1T_d$ to 2H is a multi step process and goes via different metastable structures. In the case of WS_2, 1T is found to be more stable than MoS_2. After annealing at different temperature the structure does not transform to 2H phase completely and defects are believed to stabilize the residues of 1T phase.

Formation of metastable tetramer diamond unit along with zigzag chains with a new orientation formed by e^- beam irradiation of zigzag 1T phase of Li intercalated WS_2 has been reported [17]. In the 1T zigzag starting phase both tetramer and triangular clusters were present. The presence of triangular cluster in K intercalated 2H-MoS_2 has already been predicted theoretically [18] and experimentally confirmed [30]. Theoretically the energy difference between the two meta-stable structures is found to be 0.1 eV per formula unit. The

stabilization of the local tetramer in the present case is due to electronic charging effect. It was argued that the observed distortion is not a charge density wave (CDW) phenomena but rather Jahn Teller (JT) type introduced by a weakening of the W-S bonds leading to electronic instability. However, ReS_2 is not a Jahn Teller type as argued before because the gap opens in the *d* bands at the Fermi level as confirmed by modern first principle calculations [10, 30, and 13].

Thus, in the present report, stabilization of $1T_d$ structural form of $Re_xMo_{1-x}S_2$ and $Re_xW_{1-x}S_2$alloys has been explored by both theory and experiment. Theoretically, a structural cross over is observed at approximately 50% alloy composition in both monolayer and bulk form. In this context, the stability of metallic 1T phase of MoS_2 upon 25% Sn substitution was predicted theoretically [31]. There are some reports where Re incorporation in MoS_2 forms nanotube, fullerene, and nanoparticles which forms reported to show beneficial effects on HER activity [32-37].Taking theory as a guide experimentally only 50% alloy composition is synthesized in both the cases. However, for $Re_xMo_{1-x}S_2$ alloy two different compositions i.e. 50 and 75% and for $Re_xW_{1-x}S_2$ case mostly homogeneous 50% alloy composition was obtained after the synthesis procedure. In the case of $Re_xMo_{1-x}S_2$ alloy, two different types of modulations i.e. tetramer (type I) and trapezoid like modulations (type II) or two different modulations between two different cations for 50% and a trimmer modulation is observed for 75% alloy composition. The observation of stable trimerized structural modulation is important as this could be useful as a thinnest platform for ferroelectric devices [25]. On the other hand in $Re_xW_{1-x}S_2$, the alloy formation is homogeneous and only one type i.e. tetramer modulation (type I) is observed along with some areas with different modulation vectors probably due to slightly varying composition in these areas. The energy difference between the metallic and semiconducting ground states with a slightly differing structural parameters is found to be very small; 90 and 40 meV for the 50% $Re_xMo_{1-x}S_2$ and $Re_xW_{1-x}S_2$alloys, respectively. This could be an excellent monolithic candidate for the metal-semiconductor transition with minute external perturbation suitable for application as a nanoscale switching device. Overall, the results show that the alloy can be formed between these important materials system with a differing stable structural form of the terminal compounds i.e. 2H and $1T_d$ and the various structural modulations observed offers yet another way to controlling the electronic structure of this system other than intercalation, strain, and vertical stacking arrangement. While high resolution electron microscopy revealed the details of such modulated structures, the density functional theory based calculations throw light on the implications on the electronic properties of such alloy system.

8.2 Experimental method

$Re_{0.5}X_{0.5}S_2$ (X = Mo and W) alloys were synthesized following a similar synthetic procedure reported earlier for ReS_2 [13]. In short, rhenium (wire, 1.0 mm diameter, 99.97%, Alfa Aesar), molybdenum/tungsten (powder, 99.9%, Sigma Aldrich / powder, 99.8%, Sigma Aldrich) and sulfur (powder, -325 mesh, 99.5%, Alfa Aesar) were taken in the stoichiometric ratio (1:1:4) and sealed in an evacuated (10^{-5} mbar pressure) quartz tube. The tube was then heated to 200 °C at the rate of 10 °C/h followed by annealing at that temperature for 2 h in order to avoid any possible explosion due to the high vapor pressure of sulfur. Next, the temperature was raised to 900 °C at a rate of 20 °C/h and annealed for 120 h after which the furnace was shut down and the sample was allowed to cool to room temperature naturally. The final product was fine black powder.

All the high resolution phase contrast transmission electron microscopy (HRTEM, in ICMS, India) and Z-contrast high angle annular dark field imaging (HAADF, in KAUST, Saudi Arabia) were performed in a FEI TITAN aberration corrected 80-300 keV TEM. Powder alloy samples were sonicated for 40 minutes to exfoliate monolayer materials for TEM imaging and energy dispersive spectroscopy (EDS) analysis.

8.3 Theoretical calculation

The Electronic structure calculations were performed using density functional theory (DFT) as implemented in WIEN2k code [38]. WIEN2k uses linearized augmented plane waves as the basis and considers all electrons into the calculation. We have used the following structures for the present calculation: monolayer and bulk form of 2H & 1T MoS_2, WS_2, ReS_2, various alloys between them and also considering structural modulations for ReS_2 and some of the intermediate alloy composition. The schematic of calculated structures are shown in various figures while describing the results. For the construction of bulk (1T/2H) and monolayer (1T/2H) $Re_xMo/W_{(1-x)}S_2$ alloy structure, various sizes of super cell depending on Re concentrations were constructed e.g., (i) 4×4×1 supercell for 6.25% Re, (ii) 4×2×1 for 12.5% Re, (iii) 2×2×1 for 25% and 75% Re, and (iv) 2×1×1 for 50% Re. A Γ centered 30×30×1 and 30×30×18 k point mesh was used for single formula unit cell of monolayer and two formula unit cell of bulk. The number of the k-mesh points was reduced proportionally for the larger supercell.

For bulk MoS_2 and WS_2 calculation, a unit cell consisting two formula unit was considered with Bernal stacking along the *c*-direction. DFTD3 was introduced for dispersion correction which considers van der Waals interaction between the layers [39]. In case of monolayer calculation, 16 Å vacuum was added between the layers in order to prevent interlayer coupling. The optimization of lattice parameters and atomic position for the MoS_2, WS_2 and distorted ReS_2 model were performed using the generalized gradient approximation (GGA) exchange-correlation functional of Perdew, Burke, and Enzerhof (PBE) [40]. The criteria of convergence for force, energy and electronic charge were set below 1 mRy/au, 0.0001 Ry and 0.001 e, respectively. The relaxed lattice parameters of MoS_2, WS_2, modulated ReS_2, and all other alloy structures considered for the present calculations are shown in figure 8.13 and 8.14. The muffin tin radii and RMT were chosen in such a way that they do not overlap. The K_{max} was set at 7.00/RMT.

8.4 Results and Discussion

8.4.1 Types of modulation

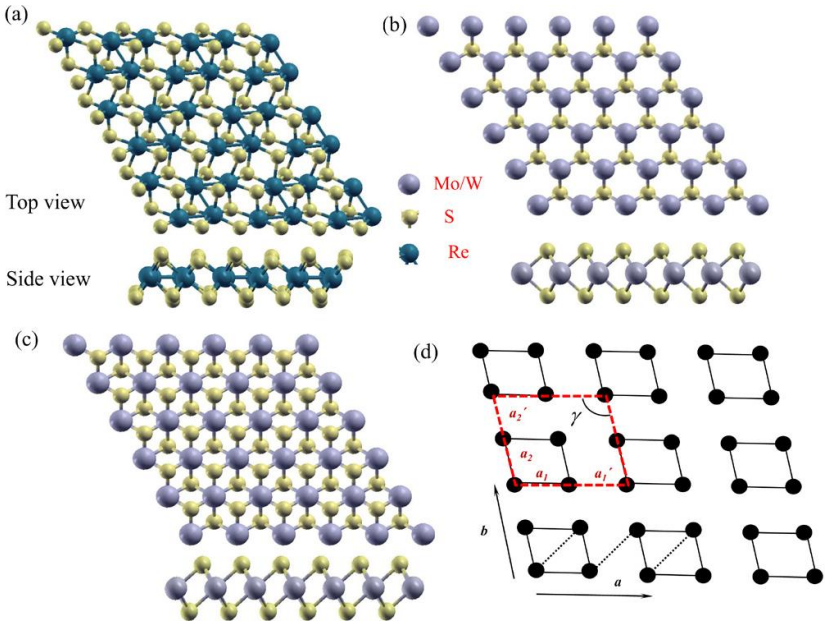

Figure 8.1 Schematic structural models of (a) $1T_d$ ReS_2 (b) 2H MoS_2/WS_2, (c) 1T MoS_2/WS_2, and poly-types. The side view of each of poly-type is also shown. (d) schematic super cell unit for the superstructure phases of $1T_d$ structure with various structural parameters defined by a_1, a_2, a'_1, a'_2, a, b, and γ. These structural parameters are used throughout the text to define various superstructure observed. Also, various colors different types of metal-metal hybridization bonds possible in the systems.

We begin with the experimental structural description and associated superstructures observed by high resolution transmission electron microscopy in both $Re_xMo_{1-x}S_2$ and $Re_xW_{1-x}S_2$ alloy systems. As mentioned earlier, the most stable structure of ReS_2 is $1T_d$ (space group 2: $P\bar{1}$) and for MoS_2 and WS_2 is 2H (space group 194: $P6_3/mmc$).ReS_2 is known to be in a 2D Peierls distorted $1T_d$ structure where four Re atoms hybridize to form Re_4 clusters. Incorporation of Mo and W atoms in the ReS_2 lattice modifies the metal-metal hybridization between the cations and influences the structural modulation and electronic property of the system. Figure 8.1 (a) is the typical $1T_d$ ReS_2 structure where four Re atoms together hybridize to form tetramer Re_4 cluster forming quasi two dimensional chains like superstructure. The calculated super lattice spots corresponding to 1T and periodic modulations/superstructure ($2a\times a$) are indicated with two different color circles. The lattice parameter of monolayer ReS_2 is a = 6.4308 Å, b = 6.4912 Å and γ = 119.03°. The typical stable 2H and distorted 1T structure of MoS_2 and WS_2 are shown in the figure 8.1 (b) & (c). Kindly note, that the length of the edges and the angle between them of the modulated structural units can be different along different directions for the same superstructure periodicity depending on the alloy composition. Therefore, in order to distinguish such modulations between different alloy systems we take help from the geometry by drawing a rhombus with four cations at the corners as shown in Figure 8.1 (d). Two different directions are defined as a_1 and a_2, with an obtuse angle between them as γ. Another two parameters defined as a'_1 and a'_2 along the original a_1 and a_2 directions, which will define the distance between the hybridized units along the two different directions. The super cell lattice parameters of the system are also defined in terms of repeat vectors a and b (figure 8.1 (d)). This is helpful to describe in details the nature of modulation vector and their strength along distinct directions, which in the literature either various nomenclature or dimensionality of modulations (1D or 2D) was used to define such structures. However, distortions can be quasi 2D with different lattice vectors and strength along different directions and therefore, we have used this definition to distinguish the various structural distortions observed in both the alloy systems. Additionally, the bonding lines between cation-cation represent hybridization and various types of hybridization possibilities are also indicated in the same figure. For both the alloys, all the structures are found to be the $1T_d$ poly-type form with different types of superstructures depending on the alloy composition. All the structural parameters obtained from theoretical and experimental observations are described here.

8.4.2 Alloy of $Re_xMo_{1-x}S_2$

Three different types of structural modulations or super structures are observed in this alloy system depending on the composition. Out of three, two different modulations are observed for the same 50% and the third one with a trimerize type modulation for 75% $Re_xMo_{1-x}S_2$ alloy case. Percentage numbers in the alloys indicate the composition in terms of either Mo or W in the host ReS_2 lattice. There are areas where pathways of poly-type structural transition are observed due to gradual changes in Re concentrations and are also described. The EDS analysis for 50% alloy is shown in figure 8.2.

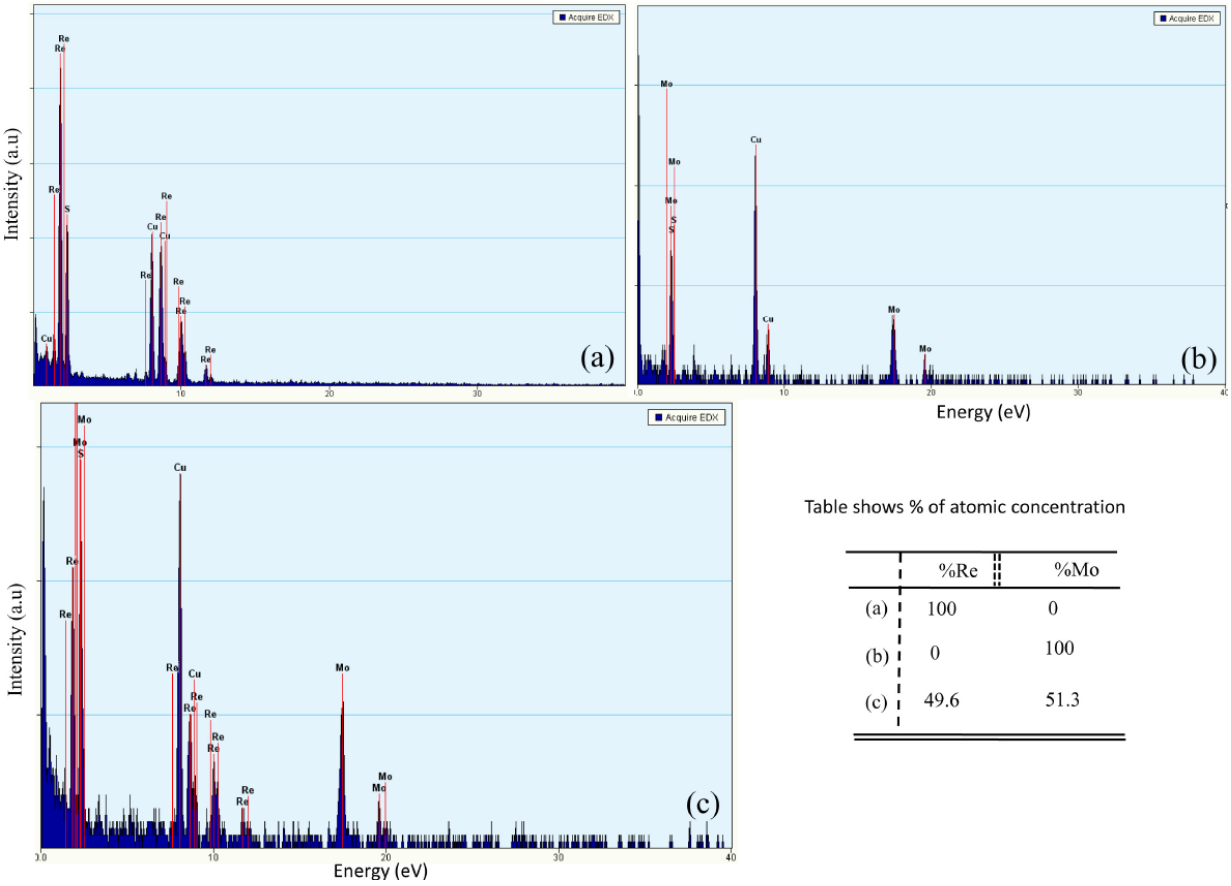

Table shows % of atomic concentration

	%Re	%Mo
(a)	100	0
(b)	0	100
(c)	49.6	51.3

Figure 8.2 (a)-(c) shows the EDS of pure MoS_2, ReS_2, and $Re_{0.5}Mo_{0.5}S$.

8.4.3 Type I modulation of 50% $Re_xMo_{1-x}S_2$

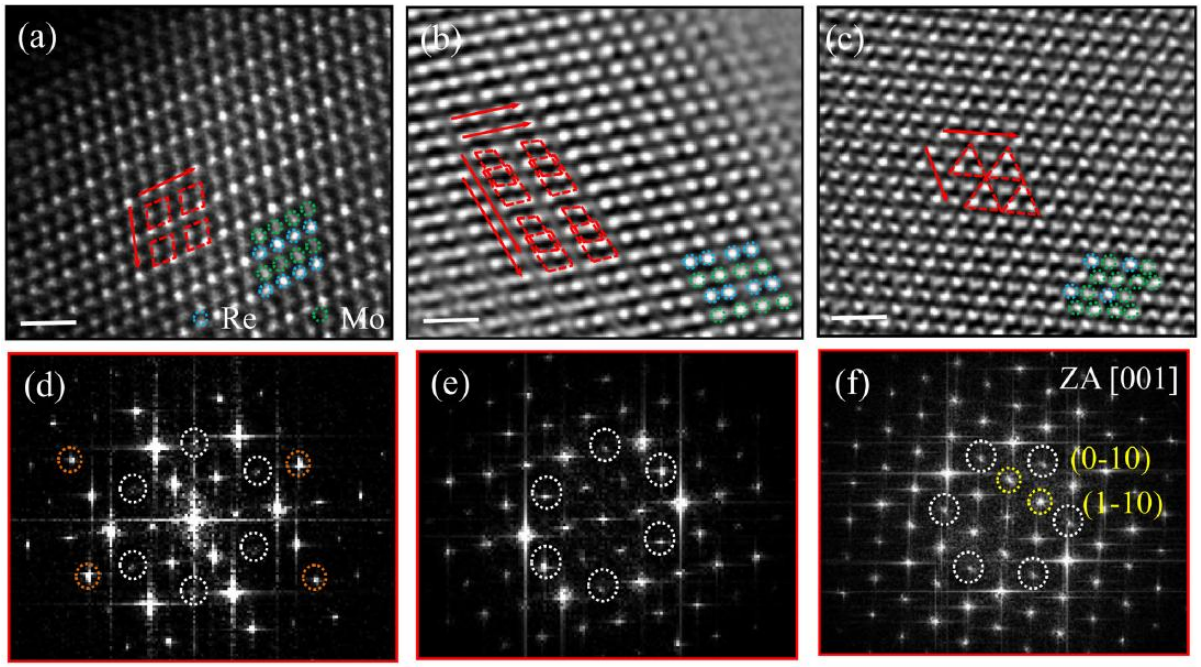

Figure 8.3 Various types of superstructures observed in the case of $Re_xMo_{1-x}S_2$ alloy. Two different types of structural modulations are observed in $1T_d$ phase with X_{Re}= 50%, (a) type I, where alternate rows are filled either by Re or Mo atoms giving rise to a superstructure which can be defined by 2a×2a supercell and (b) type II where the superstructure can be defined by two different 4a×2a supercells. The corresponding FFTs are shown in (d) and (e) where characteristic spots confirming the 1T phase and structural modulation are marked with white and yellow circles show atomic planes, respectively. The major difference between superstructuer (a) & (b) is two different metal-metal hybridization distance (see text for details). (c) A trimer structure modulation is also observed with X_{Re}= 25% areas where trimer made of Mo atoms forming corner sharing triangular arrangement. The corresponding FFT is shown in (f). The structural parameters derived from experimental images are given in the table and indicates that they are more close to ideal hexagonal sytem in case of (c) and triclinic type in case of (a) & (b).The orange circle corresponds to upper lattice spot. The scale bar is 0.5 nm.

Figure 8.3 (a) shows the modulation for the monolayer alloy. Alternate rows are filled by either Re and Mo atoms. This gives rise to the different modulations of lattice parameters along different directions. This is schematically shown in the inset. The Mo-Mo, Re-Re, and Re-Mo distances are 2.88, 2.80 and 2.68 Å, respectively. The acute angle γ of the rhombus is

74°. a'_1 and a'_2 are 2.9, and 2.7 Å. The FFT (fast Fourier transformation) equivalent to the periodic diffraction pattern of the image is shown in figure 8.3 (d). FFT also shows the signature of the $1T_d$ phase. The super lattice spots corresponding to $1T_d$ phase is strong along one of the directions which correspond to the parallel planes containing only Re and Mo atoms. The observed modulation in this case is similar to the ReS_2 but with different lattice vectors. The large scale image of figure 8.3 (a) is shown in figure 8.4.

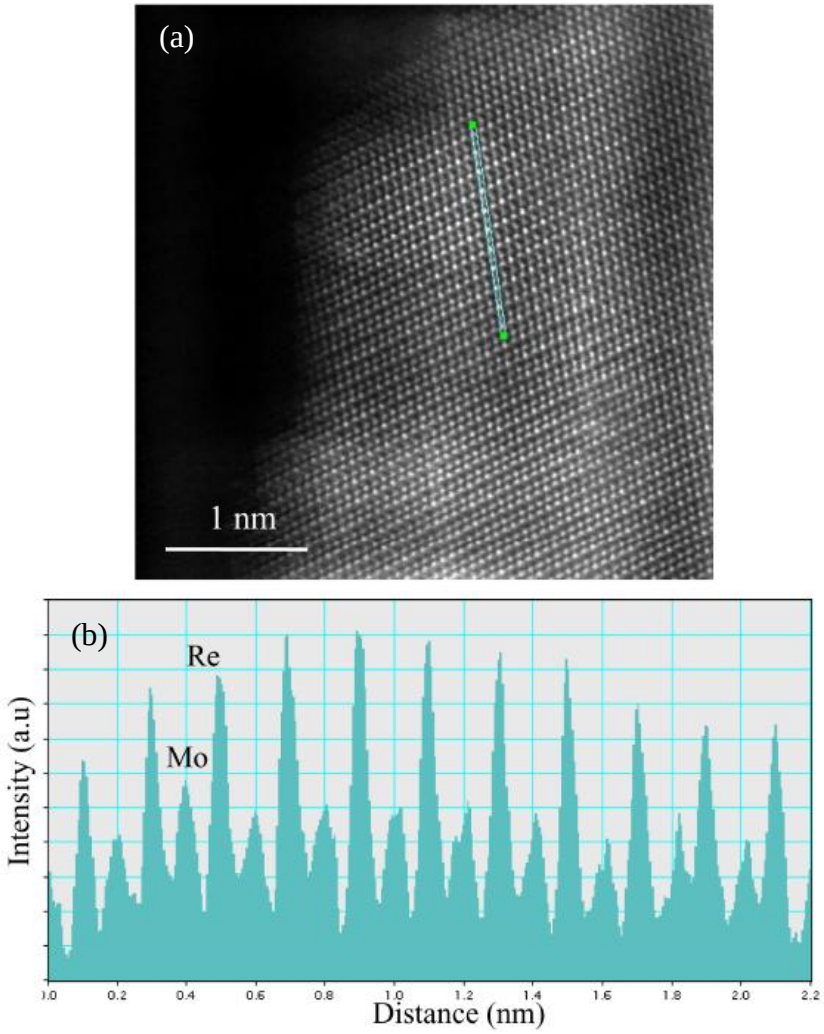

Figure 8.4 (a) Z-contrast HAADF images of 50% $Re_xMo_{1-x}S_2$ alloy with type I structural modulation. (b) Line profile along a row of atoms identifying Re and Mo atoms occupying alternately in the lattice.

The Z-contrast line scan profile of HAADF-STEM clearly shows Re and Mo atoms are occupying alternative column in lattice.

8.4.4 Type II modulation of 50% $Re_xMo_{1-x}S_2$

For the same 50% alloy composition, a unique structural modulation is observed in some areas particularly near the surface regions and to best of our knowledge this type of structural modulation is not known in the literature (figure 8.3 (b)). Two consecutive parallel lines are marked along which modulation of cations are different i.e. one short and another large distance periodic structural modulation. This can also be thought of in terms of two independent one dimensional Peierls distorted atomic chains or 2D type with doubling the edge of one side of the super cell unit. Considering all four atoms from the consecutive rows, a trapezoid like geometry can be identified or in other words the structural parameters can be described using two numbers of rhombuses and doubling the side along one direction (inset of figure 8.3 (b)). The lattice parameters are shown in the same figure. FFT also reflects the corresponding symmetry (figure 8.3(e)). The distances between the atoms which are short and long are 2.42 Å and 2.69 Å, respectively. This trapezoid structure can be stabilized in both tetramer type of modulation in like Re_4 in ReS_2 (2D chain) and NN configurations (1D chain) depending on Re concentration.

8.4.5 Trimerized modulation of 75% $Re_xMo_{1-x}S_2$

In this case, a trimerized modulation is observed as shown in figure 8.3 (c). The triangles are indicated in the figure along with the schematic (inset in figure 8.3(c)) and the length of the edges is equal to each other and is 3.2 Å. At the center of the large hexagon Re atom is occupying the site as marked with the blue circles. The structure can also be described by two parallel lines with one of them completely occupied by Mo atoms and another one is alternately filled by Mo and Re atoms. The distance between the Mo-Re atoms is 2.8 Å. The γ is 109° in this case. The FFT shows the signature of $1T_d$ phase along with structural modulation (figure 8.3 (f)). The observation of stable trimmer modulation is significant in the sense that such a structure was predicted to be the thinnest ferroelectric in the case of MoS_2 [23]. The large scale trimerized modulations with metal-metal bond length are shown in figure 8.5. The present alloy offers a stable trimmer system without intercalation route and might be amenable for a possible thinnest ferroelectric device fabrication. The Mo-Mo distance in the trimmer is ~ 3.2 Å. The Re-Mo or Re-Re bond distance in trimmer is ~ 2.8 Å to 2.9 Å as shown in the HRTEM images.

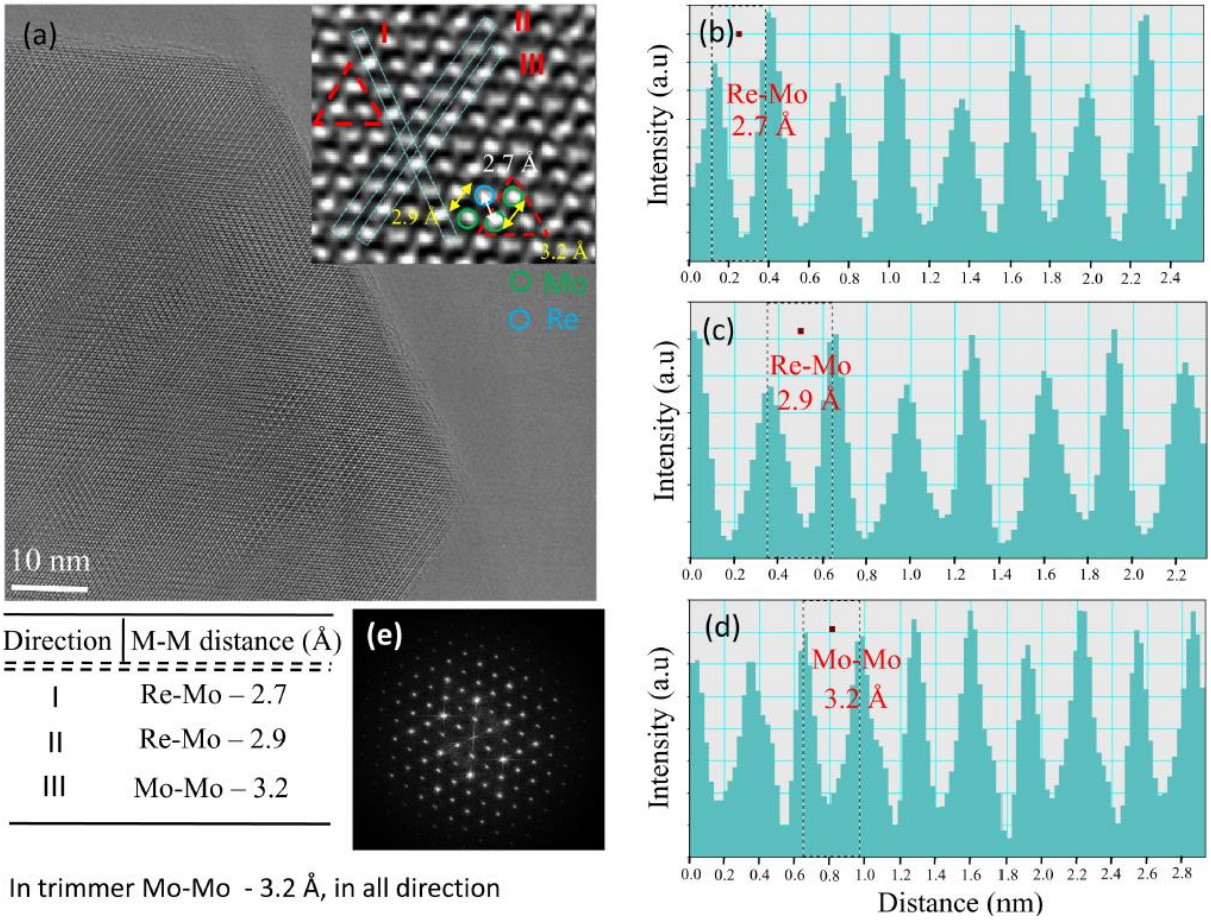

Figure 8.5 (a) Low magnification HRTEM image of trimer. The red and green color indicate Re and Mo atoms respectively. (b) – (c) are line scan to show distances from metal-metal bond from different direction mentioned in the inset. (e) shows the FFT of figure (a). Metal-Metal distances are listed in the table.

8.4.6 Modulated phases from FFT

Simulated diffraction pattern of distorted 1T phases from theoretical crystal structure is well compared with selected area diffraction (SAD) in figure 8.6. We have simulated diffraction pattern of distorted 1T phases from theoretical crystal structure using electron beam direction of [001]. We have used JAMES software to calculate theoretical diffraction. The modulated superstructure of 1T′ is marked with orange and yellow circle while the spots highlighted by white circle can be used to distinguish between 1T′ and 1T′′.

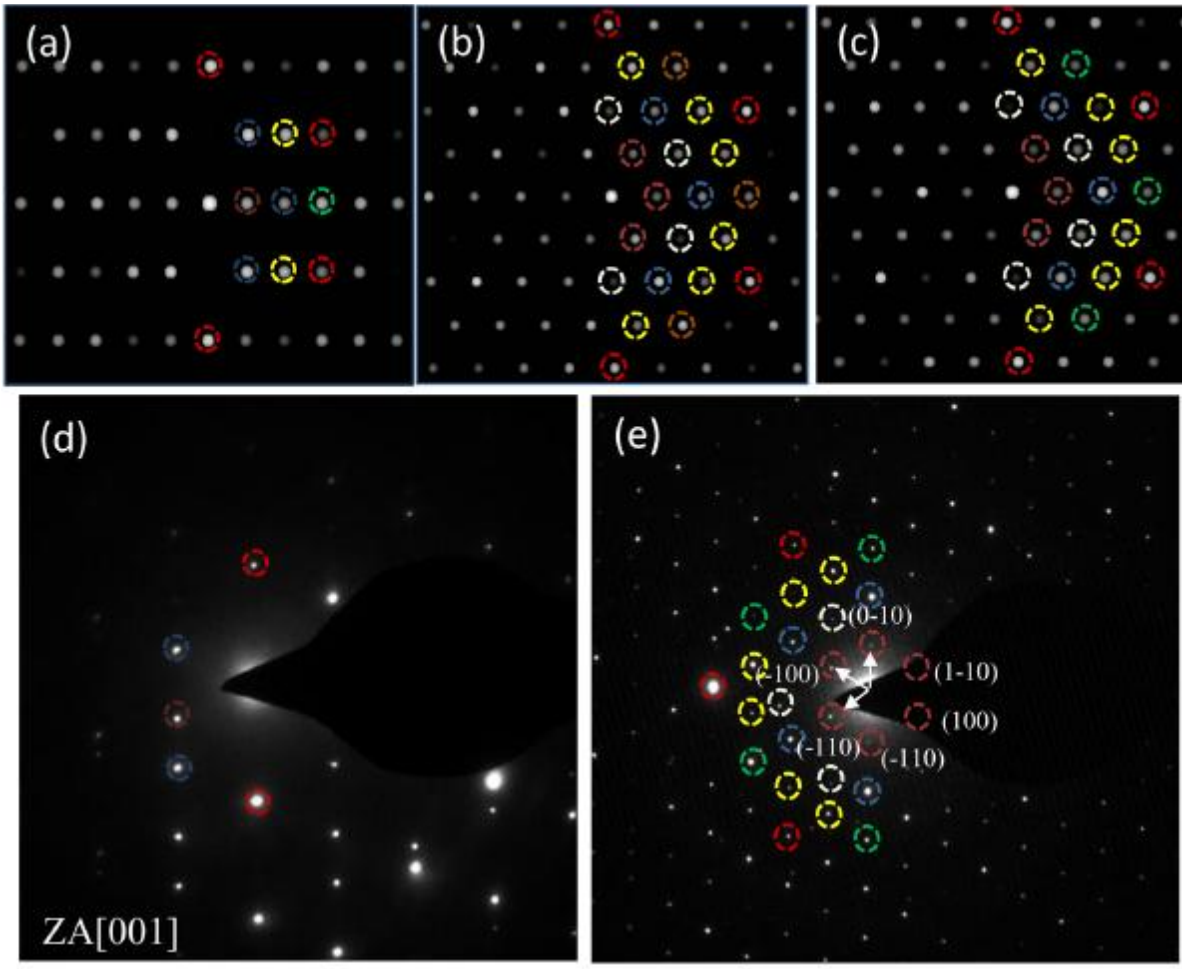

Figure 8.6 (a)-(c) James simulated structure of $1T_d$ matches experimental $1T_d$ (d) and (e)structure.

8.4.7 Distortion in hexagon and sulpher (S) plane gliding: HRTEM

In some areas, the pathways of phase transition between 2H to $1T_d$ structure is observed due to gradual changes in Re concentrations as shown by both HRTEM and HAADF images (figure 8.7 & 8.8).

This is an accidental finding and involves different intermediate phases depending on local Re distributions. Four distinct intermediate transition phases have been identified as shown in figure 8.7. The transition from 2H to $1T_d$ takes place via simultaneous rotation and gliding of one of the two S planes of the 2H crystal structure. As mentioned before, that Re-Re, Re-S bond length are shorter compared to Mo-Mo, Mo-S counterpart because of the smaller ionic radius of Re. The gradual decrease in Metal-S bond length due to introduction of Re atoms at

Mo sites can be observed for the intermediate phases in going from 2H to $1T_d$ and these are indicated and tabulated in the same figure. The intermediate phase IV is similar to the intermediate stripe phase reported earlier for the hydrogenated 2H MoS_2 surface [41].

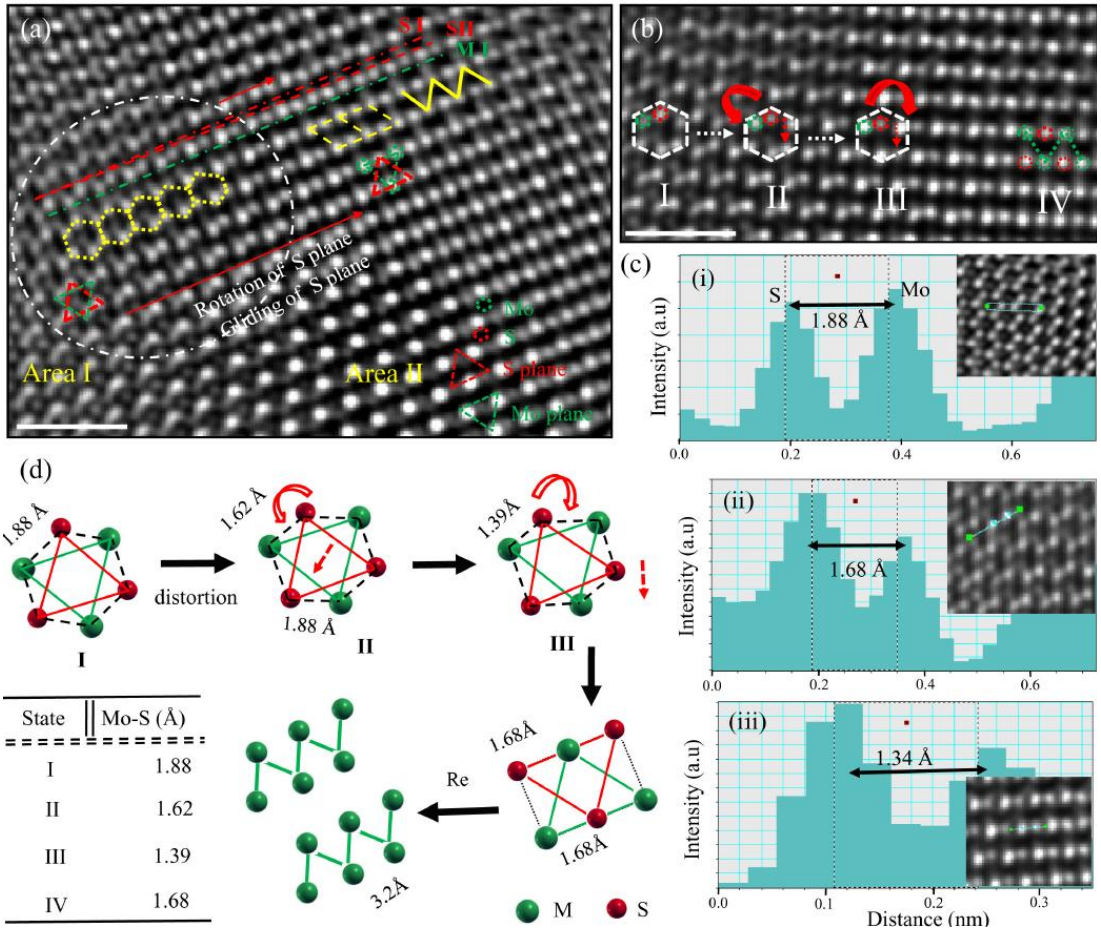

Figure 8.7 (a) is the HRTEM image showing the pathway of phase transition from 2H to $1T_d$ through intermediate metastable state. The phase transition occurs via rotation and gliding of upper S plane and is also indicated. SI and SII lines are the position of upper S plane before and after the S plane movement while the bottom S plane is static. Re doping modulates cation (metal) as shown in yellow color. Figure (b) display the magnified view of gliding and rotation of upper S plane associated with intermediated phases. Figure (c) shows Mo-S bond length in distorted and undistorted MoS_2. Figure (d) is the schematic to represent evolution of $1T_d$ phase from 2H through different intermediate phases. The experimentally derived metal-S bond lengths in different states are listed in the table. The scale bar is 1 nm.

As already mentioned, the presence of four different phases are due to different distribution of Re in the MoS_2 lattice which can clearly be observed in Z contrast image and

the route from 2H to $1T_d$ transition is indicated by arrows figure 8.7. This image shows clearly the movement of S plane due to Re incorporation in the lattice and extent to which the plane will move depends on the local population of Re.

8.4.8 Lattice distortion: High angel annular dark field (HAADF) – scanning transmission electron microscopy (STEM)

Figure 8.8 (c)-(f) is showing the atomically resolved images from areas with single Re substitution, two Re atoms forming a dimmer, three Re atoms forming a trimmer, four Re forming a tetramer, respectively.

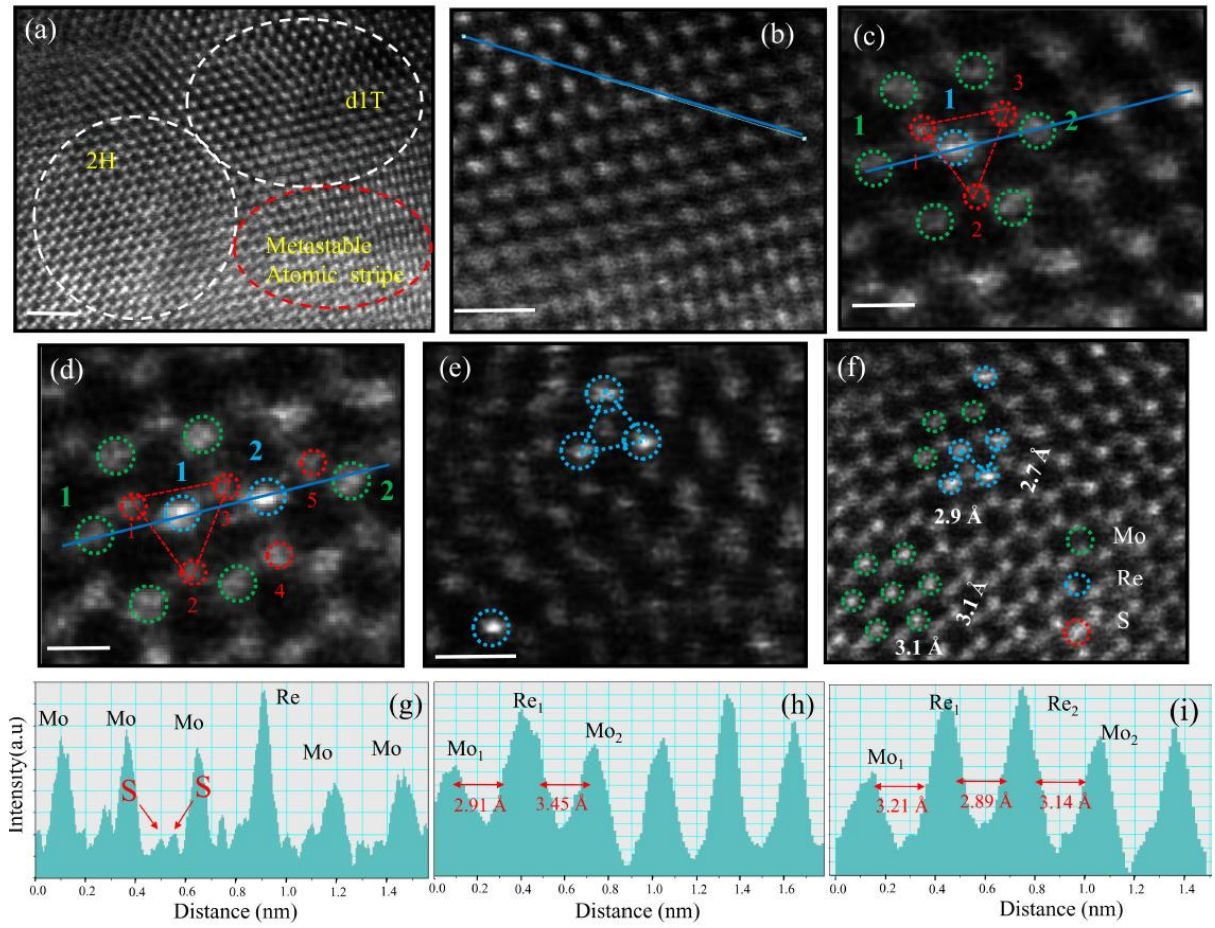

Figure 8.8 (a) The HAADF STEM images show the phase transition from 2H to $1T_d$ through intermediate metastable phases. This is equivalent to figure 3 but with the direct detection of Re atoms in the lattice. Figure (b) is the $1T_d$ phase and the (g) corresponding line scan showing two S peaks in between two metal atoms. Figure (c)-(f) show monoatomic, two, three and four (tetramer geometry, Re_4) atom clusters in Re doped MoS_2. The figure (g) (h) and (i) are the line scan showing Re dopant corresponding to figure (b), (c) and (d) respectively. The scale bars are 0.5 nm for (a), and 0.2 nm for (b)-(f).

The various metal-metal and metal-S bond lengths are also mentioned. It is found that the smallest Re-S bond length in mono atomic doping is 1.39 Å (Re_1-S_1) and for dimmer is 1.42 Å (Re_2-S_3) and 1.65 Å (Re_1-S_3) in Table 8.1. The area where four Re atom forming tetramer the metal-metal distance is 2.7 Å and 2.9 Å which is similar to Re-Re distance in ReS_2. Example line profile identifying two different metals for various clustering are shown in the inset. A gradual S plane rotation (along with gliding of plane) is observed from 2H to $1T_d$ phase and associated modulation of structure due to hybridization between cations.

A detailed schematic representation showing the correlation between the movements of S plane with Re content for various intermediate phases observed experimentally are given in figure 8.7 and this contain very rich structural variation in this 2D alloy system. The distorted metal-anion bond length is listed in the Table 8.1.

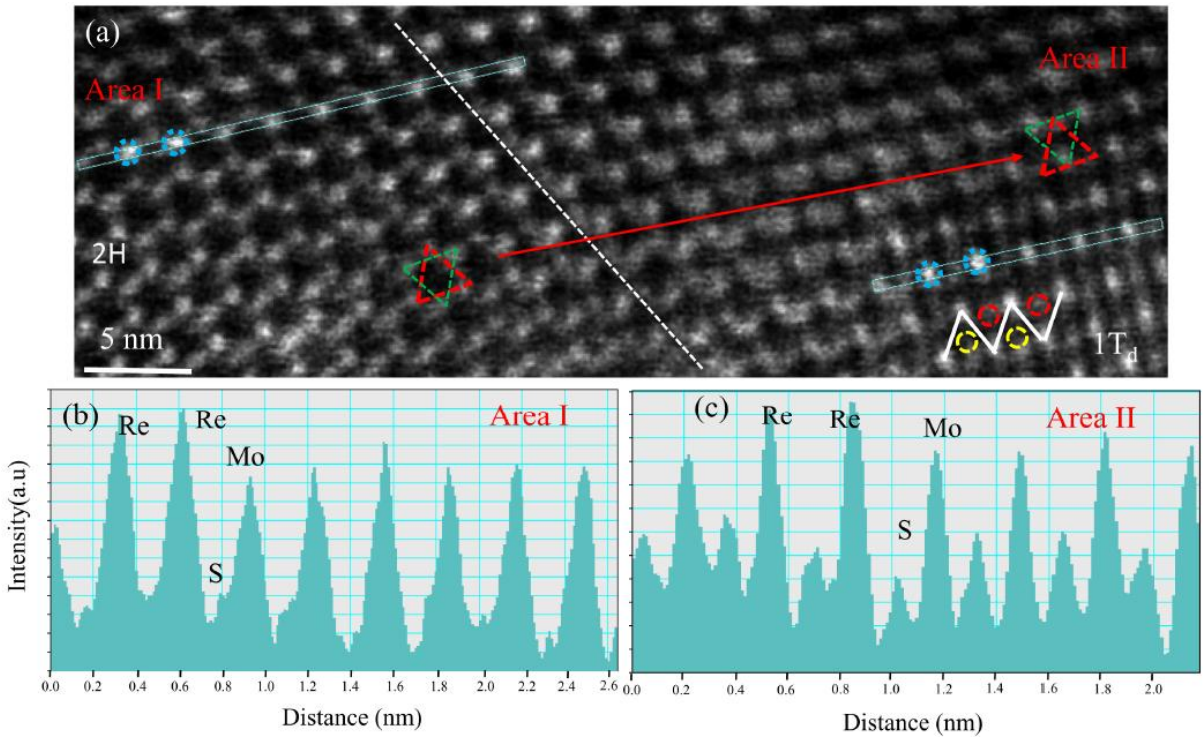

Figure 8.9 (a) shows Re incorporation in 2H phase and in the intermediate phases. The line profile shows the atomic identification in the lattice.

The continuation of figure 8.7 is clearly visible in HAADF STEM image in figure 8.9 where the distorted phases are clearly visible with dopant atoms. It is worth investigating the electronic properties of such intermediate phases, which is part of further work.

Metal-S bond length due to Re dopant

I - Mono atomic
II- di atomic

I

Bond	M-S (Å)
Re-S_1	1.39
Re-S_2	2.22
Re-S_3	1.74
Re-Mo_1	2.91
Re-Mo_2	3.45

II

Bond	M-S (Å)
Re_1-S_1	1.76
Re_1-S_2	2.20
Re_1-S_3	1.65
Re_2-S_3	1.42
Re_2-S_4	2.11
Re_2-S_5	1.97
Re_1-Re_2	2.89
Re_1-Mo_1	3.21
Re_2-Mo_2	3.14

Table 8.1 Metal-metal & metal-S distances for (I) mono atomic Re and (II) di atomic Re dopant.

8.4.9 Possible mechanistic pathway from 2H to $1T_d$

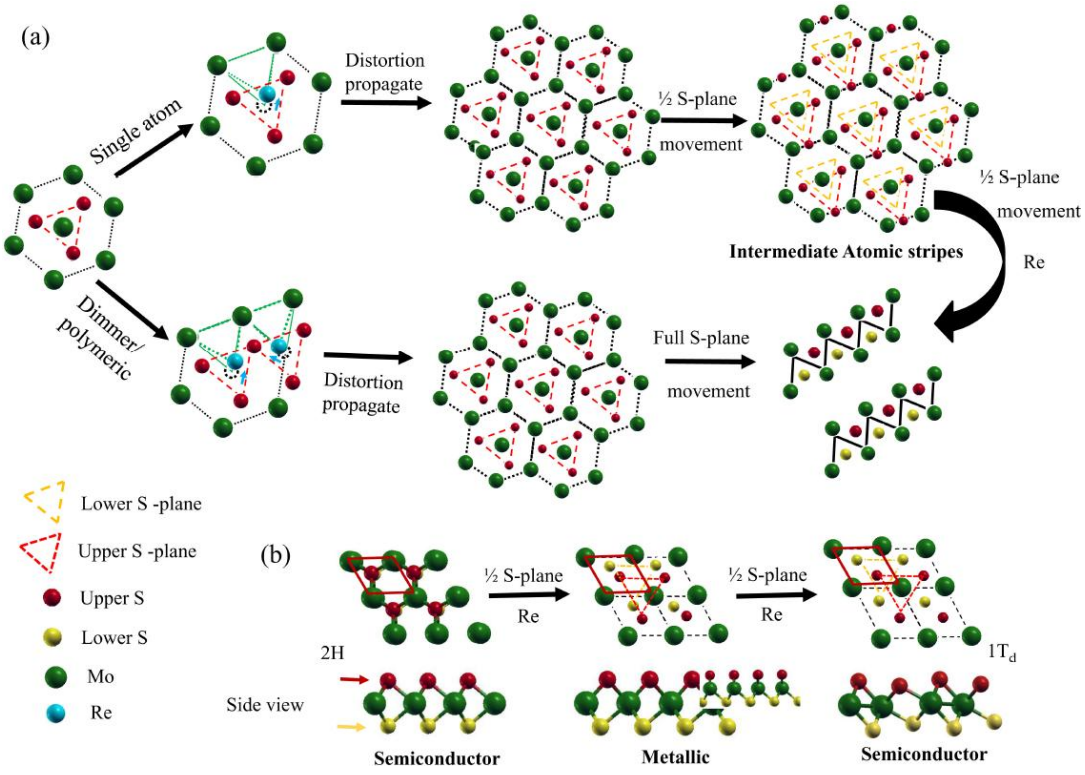

Figure 8.10 The Schemtic representations show the route of poly-type phase trasitions from 2H to $1T_d$ through various intermediate phase. (a) shows two possible route for transition depending on Re concentration, I) Monoatomic Re doping, and II) di or polyatom doping in 2H. (b) shows the side view of (a). The uper sulphur plane is displayed with red color.

The possible mechanistic pathways due to Re doping is described in this schematic (figure 8.10 (a)). We have found how the distortion will work in case of mono atomic and polyatomic Re doping. The Re-Re and Re-metal (Mo/W) bond length being shorter then Mo-Mo / W-W bond length. The single Re incorporation of Re atoms where Re-Re bonding is absent, stabilize the metastable intermediate atomic stripe step due to ½ path movement of any S plane. The distortion due to Re incorporation in lattice propagates through the whole crystal. The blue arrow in the schematic shows the shifted position of Re atoms, which creates smaller Re-Metal bonds in distorted hexagon. The Re incorporation in the intermediate metastable state shows phase transition to $1T_d$ due to another ½ path movement of S plane. In case of polyatomic doping, where Re-Re bonds are present, transformation to $1T_d$ phase occurs directly through complete movement of S-plane. The displacement of S plane in three different phases is shown in figure 8.10 (b). These lattice compression (distortion) due to Re is followed by atomic rearrangement through intermediate state and 2H to $1T_d$ phase transition occurs. The probable phase transition through similar kind of atomic rearrangement is shown by Anjali et.al. using first principle calculation [42]. It is found from our first principle calculation study, using experimental lattice parameters that the Re doped intermediate step shows metallic character in nature. This phase transformation from 2H to $1T_d$ contains three electronic states, Semiconductor (2H) → Metallic (Intermediate) → Semiconductor ($1T_d$).

8.4.10 Alloy of $Re_xW_{1-x}S_2$

In this case, the alloy composition (i.e. 50%) is homogeneous in most of the regions probed and no variation in structural modulation is observed unlike $Re_xMo_{1-x}S_2$ alloy system except few areas where the deviation in modulation is observed probably due to slight variation in composition. This is due to good mixing between W and Re atoms as they are next to each other in the Periodic Table and have almost equal atomic size. This slight variation in the composition cannot easily be determined between W vs. Re atoms, unlike Mo vs. Re atoms where atomic number difference is high. We describe the detailed observation in the next page.

8.4.11 Type I modulation of 50%$Re_xW_{1-x}S_2$

This is exactly similar to the 50% $Re_xMo_{1-x}S_2$ alloy system described earlier with alternating layer of W and Re atoms as indicated in figure 8.11 (a). This gives strong super lattice spots in the FFT image which corresponds to the parallel planes containing mono-type atoms (figure 8.11 (b)). This is a quasi two dimensional system and the geometrical parameters are given in Table 8.2 which is slightly different compared to the MoS_2 counterpart. The angle γ is 80° between the a_1 and a_2 directions. The W-W, Re-Re, and Re-W distances are 2.78, 2.68 Å, and 2.43 Å, respectively. We do not observe type II modulation in this case like in $Re_{0.5}Mo_{0.5}S_2$ alloy system. All these lattice vectors and angels listed in the Table 8.2.

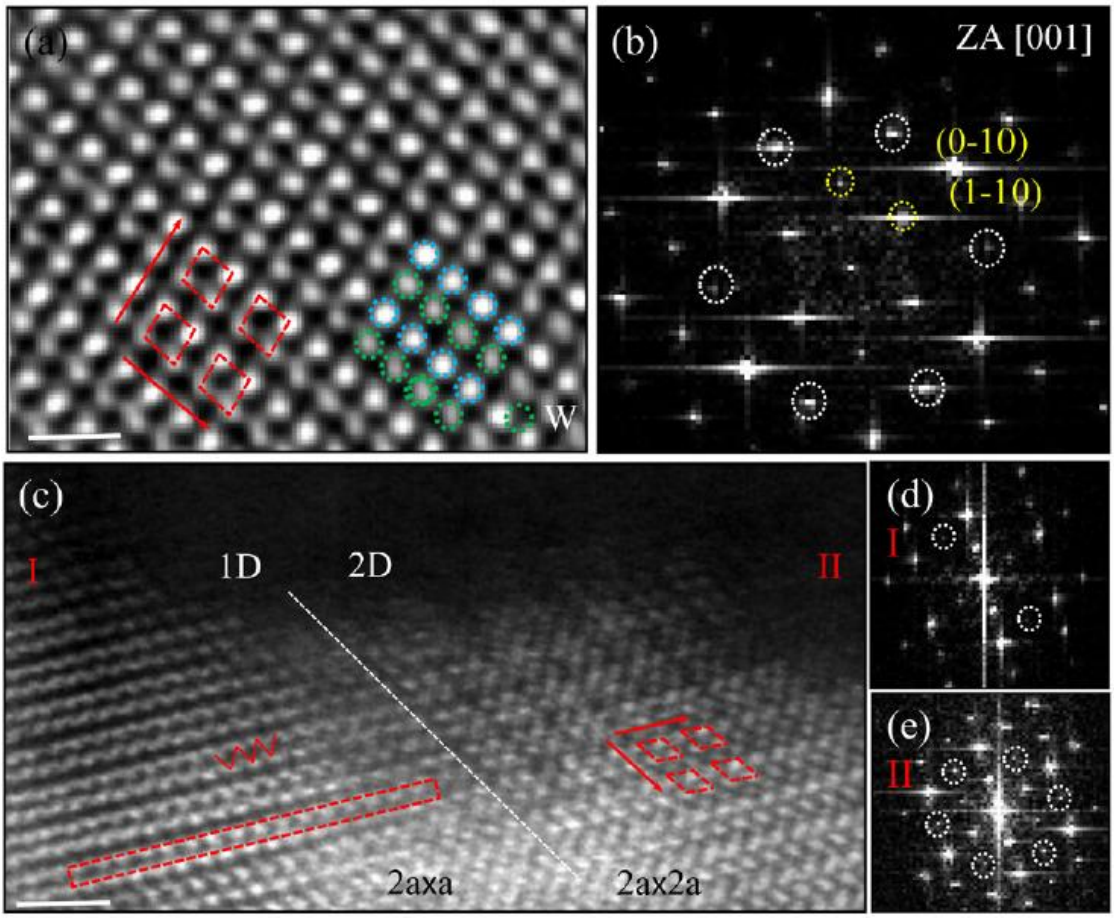

Figure 8.11 (a) HRTEM image and (b) corresponding FFT showing $1T_d$ phase with structural modulation for X_{Re}= 50% $Re_xW_{1-x}S_2$ alloy. This is similar to type I modulation observed in case of $Re_{0.5}Mo_{0.5}S_2$ alloy. (c) Some areas shows strength of structural modulation along different directions i.e. 2D vs. 1D, probably due to slightly variation of W/Re concentration and the corresponding FFTs are shown in the (d) & (e). The scale bar is 1 nm.

8.4.12 Variation in Type I modulation in $Re_xW_{1-x}S_2$

In some areas variation in the lattice parameters of superstructure modulation is observed (figure 8.11 (c)). This may be because of slight variation in W composition in the alloy in these areas. The two different areas are marked corresponding to regions with more 1D and 2D like modulation (figure 8.11 (c)). The distance of atoms inside 1D chain keep increasing near the interface and combine with another 1D chain and form 2D diamond chain like structure crossing the inter face. The existence of 1D-2D system is because of slight variation of Re in WS_2. The modulation vectors and lattice parameter for the different super cells are indicated in Table 8.2.

	a_1	a'_1	a_2	a'_2	γ°
Figure 8.3(a)	2.90	2.98	2.68	3.18	74
Figure 8.3(b)	2.41* 2.7**	3.22 2.98	5.14 5.14		114
Figure 8.3(c)	2.78	3.5	3.2	3.33	109
Figure 8.11(a)	2.42	2.71	2.43	2.71	80
Figure 8.11(c)	2.68 2.77	3.53	3.1 2.82	3.47 3.71	109

- * For Re atom
- ** For Mo atom

Table 8.2 Modulation lattice vectors and their relative angles for different type of experimental distorted 1T structures are tabulated as according figure 8.1(d).

8.4.13 Density functional theory

Density functional theory based calculation was carried out as a function of Mo and W concentration for $Re_xMo_{1-x}S_2$ and $Re_xW_{1-x}S_2$ alloy systems in both monolayer and bulk. Figure 8.12 shows energy diagram for cohesive energy vs % Re concentration.

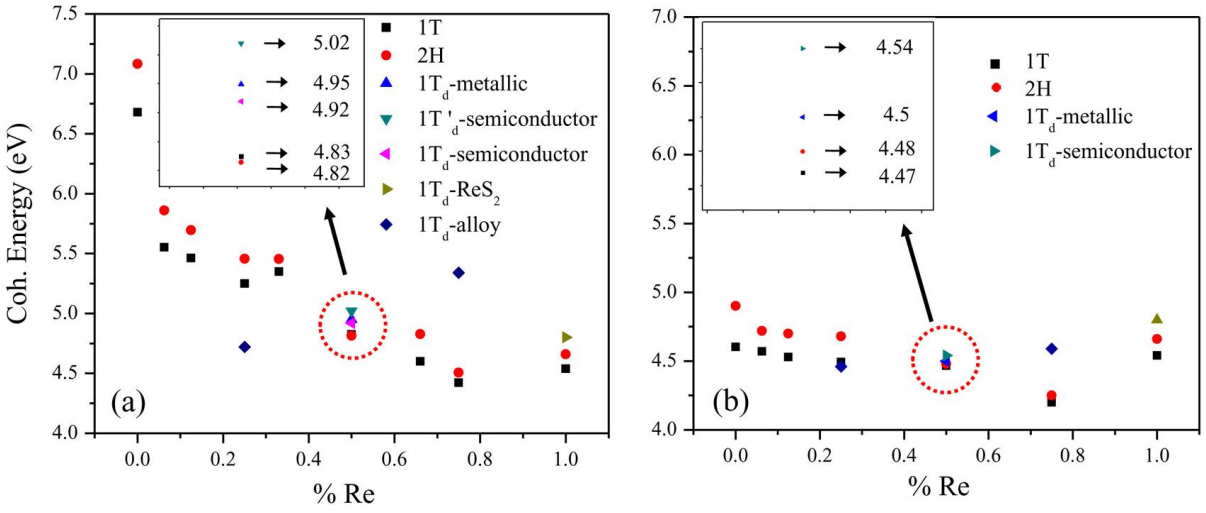

Figure 8.12 Relative stability of 2H vs. 1T poly-type of monolayer (a) MoS_2-ReS_2, (b) WS_2-ReS_2 alloys as a function of Re concentration. Compositions and the corresponding energy values are marked with different colors. Approximately, at X_{Re} = 50%, a structural cross over is observed between 2H & 1T and 2H & 1T_d poly-types. Also, (a) shows the energy values of different structural ground states for 50% $Re_xMo_{1-x}S_2$ alloys.

The data of cohesive energy against alloy composition for monolayer for two different alloys are given in figure 8.12 (a) and (b). The cohesive energy corresponding to 2H and un-modulated 1T poly-types are indicated by different colors points. All the 1T forms of un-modulated alloys are metallic and expected to have imaginary phonon mode similar to 1T MoS_2 and renders them unstable and undergo 2D Peierls structural modulation [25]. Therefore, for some alloy composition e.g., 25, 50 and 75 at.%, modulated 1T_d structural calculation was carried out to investigate the relative stability with respect to its un-modulated and 2H counterparts. One can observe that at ~50 at.% alloy composition a structural cross over between 2H to 1T_d takes place and the modulated structure is the most stable beyond that composition (see the data for 75 at. %). Therefore, it can be expected that for this composition range the alloy would be stable in the modulated 1T_d form. Experimental

results suggest that for $Re_xMo_{1-x}S_2$ alloy system, the $1T_d$ modulated structure is stable even at 75 at.% in addition to 50 at.%, however, with a trimmer type modulation. The initial calculations do not suggest the formation of such structural modulations and defects might be playing a role is stabilizing such structure through electronic charging effect [43]. It will be worth investigating both theoretically and experimentally the electronic property of such alloy superstructure for stable in-plane dipole domain structure for thinnest ferroelectric devices and beyond the scope of the present discussion [25].

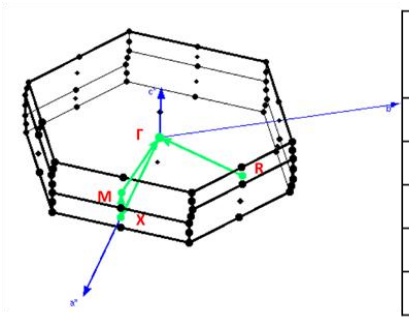

Structure	*a* (Å)	*b*(Å)	γ°	Cohesive energy (eV)
Structure-I	6.167	6.224	119.03	4.94
Structure-II	6.452	6.513	119.03	4.91
Structure-III	6.452	6.513	119.06	5.04
Structure-IV	6.472	6.534	119.03	4.54
Structure-V	6.484	6.543	119.03	4.50

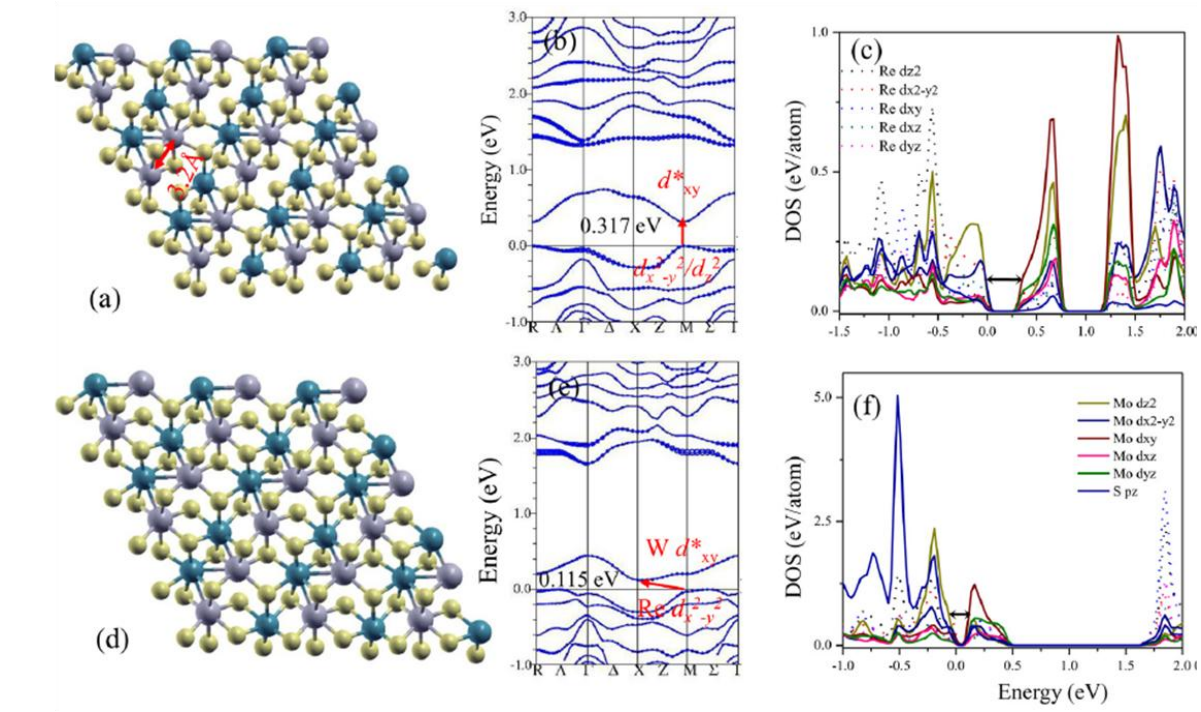

Figure 8.13 The most stable $1T_d$ structure of X_{Re}= 50% (a) $Re_xMo_{1-x}S_2$, (d) $Re_xW_{1-x}S_2$ alloy. Both the structures are semiconducting and the corresponding band structure and density of state are given (b) & (c) , (e) & (f) for $Re_{0.5}Mo_{0.5}S_2$, $Re_{0.5}W_{0.5}S_2$ alloys, respectively.Figure shows the Brillion zone for band structure and structural parameters with cohesive energy for different model structures.

Similarly, it will also be worth investigating any novel properties arising from the type II or trapezoid type modulation for 50% $Re_xMo_{1-x}S_2$ alloy system as part of the future exploration. The relative energy difference between the 2H and $1T_d$ form of structural poly-types at 50% alloy composition is 90 and 40 meV for monolayer $Re_xMo_{(1-x)}S_2$ and $Re_xW_{(1-x)}S_2$ alloys, respectively. The relative energy difference between 2H semiconductor and 1T metallic phase of MoS_2 and WS_2 are ~ 0.25 eV and 0.35 eV, respectively, which are one order of magnitude higher than the 50% alloy case. The relative stability of 1T phase in the SnS_2-MoS_2 alloy system investigated earlier reported a cross over at ~60 at.% of Sn in MoS_2 lattice and all the alloys are found to be metallic in nature [31]. The modulated $1T_d$ structure corresponding to 50% alloy composition for both the cases ($Re_{0.5}Mo_{0.5}S_2$ and $Re_{0.5}W_{0.5}S_2$) are shown in Figure 8.13. The lattice parameters are indicated with the help of rhombus geometry defined earlier. The structure is semiconducting with a band gap of 0.317 eV and 0.115 eV for $Re_{0.5}Mo_{0.5}S_2$ and $Re_{0.5}W_{0.5}S_2$alloys, respectively (figure 8.13 (b) & (c)). However, with slightly different atomic configurations for the same composition, both metallic and semiconducting states are also found to be stable with smaller energy difference. The difference between these later structural states and the most stable structural configuration is the atomic distances between two different cations. The most stable configuration is obtained if the Mo-Mo (or W-W) and Re-Re distances are different than the single value and this is because of the different sizes of the atoms which are also reflected in different lattice parameters of the individual crystals. The energy difference between semiconducting and the metallic ground states are very small, 90 and 40 meV for $Re_{0.5}Mo_{0.5}S_2$ and $Re_{0.5}W_{0.5}S_2$alloys, respectively.

This is extremely important in the sense that by small external stimuli e.g., strain, charge or photon energy can tune the conductivity of such system with the slight modification of atomic arrangement within the same host lattice. This can be useful as a switch, sensors, and many novel nanoscale electronic devices through metal-semiconductor transition [44, 45].

Though similar possibility exists between structural poly-types i.e. between 2H and $1T/1T_d$ in the family, however, the energy difference is significantly higher i.e. ~ 0.25 to 0.35 eV and only alkali metal intercalation route has been shown to be able to control such structural transitions in a reversible way. This is in contrast to irreversible transitions in SnS_2-MoS_2 based alloy reported earlier where the similar transition is composition dependent [31]. The reversible metal-semiconducting transitions between H and T´ phases of $W_{0.67}Mo_{0.33}Te_2$ by charge mediation was also predicted theoretically with the small energy difference between the two structural poly-types [44]. The nature of valence and conduction band for 50%

$Re_xMo_{1-x}S_2$, $Re_xW_{1-x}S_2$ alloy cases are briefly described below. The conduction band maximum (CBM) and the valance band maximum (VBM) of MoS_2 are made of Mo d_Z^2 orbital. In the case of ReS_2, both VBM and CBM have significant contributions from $d_{x^2-y^2}$ and d_{xy} orbital. In case of MoS_2, the direct transition occurs from K (VBM) to K (CBM) and for ReS_2, it is from Γ (VBM) to Γ (CBM). For the two alloy cases, we have found stable semiconductor state for both $Re_{0.5}Mo_{0.5}S_2$ and $Re_{0.5}W_{0.5}S_2$ with the triclinic state having $P\bar{1}$ crystallographic symmetry. Brillion zone and the symmetry points used for plotting band structure are shown in figure 8.13. The VBM energy value at M point is comparable with R point but the CBM energy at M point is lowest for $Re_{0.5}Mo_{0.5}S_2$. $Re_{0.5}Mo_{0.5}S_2$ structure shows fundamental and direct band gap of 0.317 eV with fundamental transition between M to M (figure 8.13 (b)).

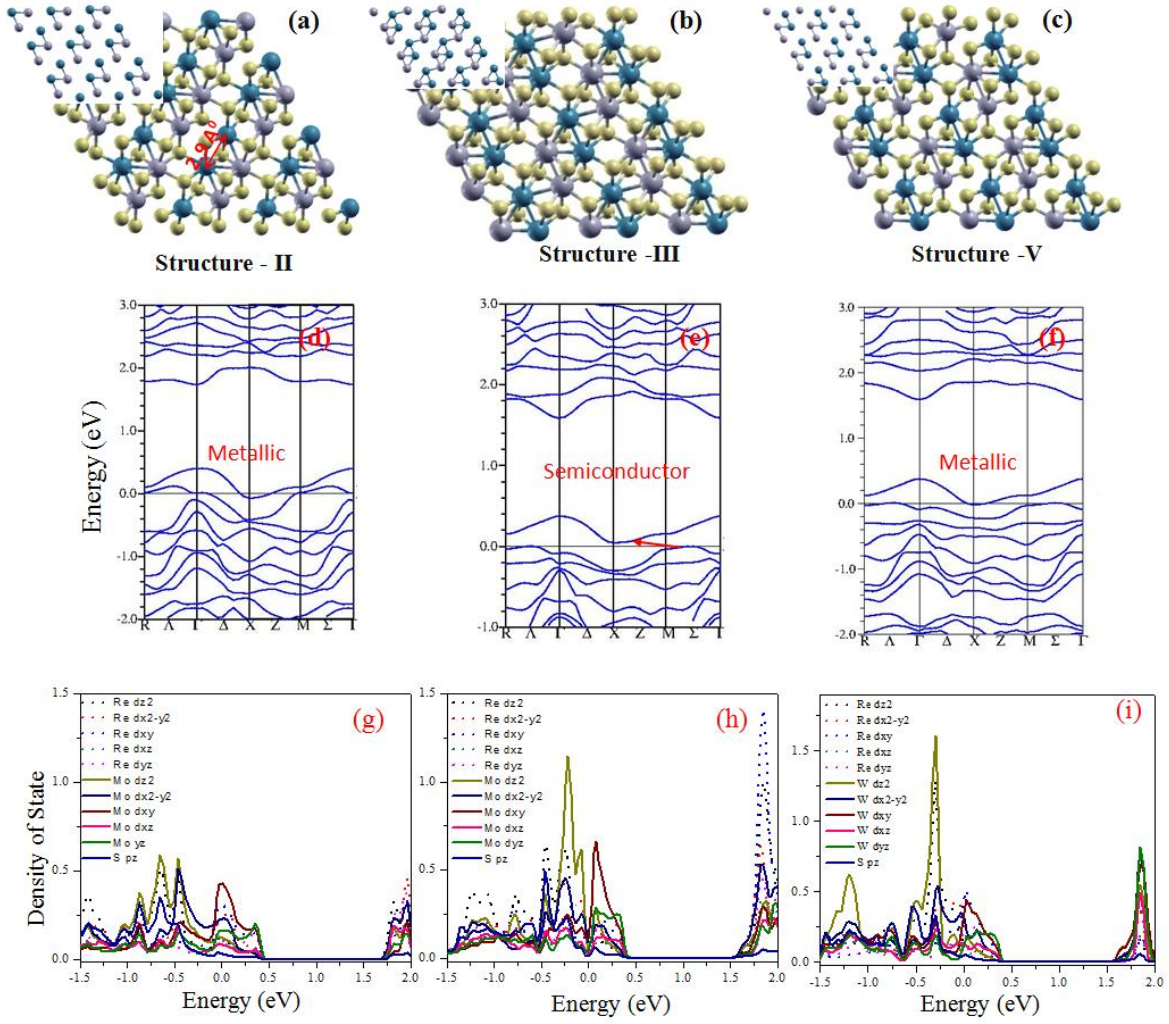

Figure 8.14 2a×a superstructure with slight variation of structural parameters, (a) metallic $Re_{0.5}Mo_{0.5}S_2$ and (b) semiconducting ground states of $Re_{0.5}Mo_{0.5}S_2$. (c) 2a×a superstructure with metallic $Re_{0.5}W_{0.5}S_2$. Band structure and DOS are given below the corresponding structures.

An indirect transition from M to X having band gap of 0.115 eV is found for $Re_{0.5}W_{0.5}S_2$ (figure 8.13 (e)). Figure 8.13 (c) & (f) shows that for $Re_{0.5}Mo_{0.5}S_2$, the fundamental direct band transition has significant contribution from Mo d_z^2, and $d_{x^2-y^2}$ orbitals at VBM and d_{xy} orbital at CBM and similarly the fundamental indirect band transition for $Re_{0.5}W_{0.5}S_2$, is primarily due to Re $d_{x^2-y^2}$ orbital at VBM and W d_{xy} orbital at CBM. The band structure and DOS for other stable configurations are shown in the figure 8.14 and the related lattice parameters are listed in figure 8.13.

8.5 Conclusions

In summary, alloy formation, 2H vs. $1T_d$ structural stability and electronic structure between MoS_2/WS_2 and ReS_2 have been explored both by theory and experiment. Theory indicates a structural cross over between 2H and $1T_d$ at approximately 50% alloy composition for both the system. Experimentally, two different structural modulations for 50% and a trimerized modulation is observed in $Re_{0.25}Mo_{0.75}S_2$ and only tetramerized modulation is observed for WS_2-ReS_2 alloy systems. The trimmer modulation could offer the stable thinnest platform to explore the ferroelectric device. The 50% alloy system is found to be a suitable monolithic candidate for metal semiconductor transition with minute external perturbation. The results show yet another way to tune the various structural types and corresponding electronic structure in this important class of materials system.

8.6 Bibliography

[1] G. Eda, H. Yamaguchi, D. Voiry, T. Fujita, M. Chen, M. Chhowalla, Nano Lett. **11**, 5111−5116 (2012).

[2] T. Cao, G. Wang, W. Han, H. Ye, C. Zhu, J Shi, Q. Niu, P. Tan, E. Wang, B. Liu, J. Feng, Nat. Commun. **3**, 887−892 (2012).

[3] K. Mak, K. He, J. Shan, T. F. Heinz, Nat. Nanotechnol. **7**, 494−498 (2012).

[4] K. S. Novoselov, D. Jiang, T. Booth, V.V. Khotkevich, S. M. Morozov, A. K. Geim, Proc. Natl. Acad. Sci. **102**, 10415-10453 (2005).

[5] K. F. Mak, C. Lee, J. Hone, J. Shan, T. F. Heinz, Phys. Rev. Lett. **102**, 136805 (2010).

[6] U. Maitra, U. Gupta, M. De, R. Datta, A. Govindaraj, C. N. R. Rao, Angew. Chem. Int. Ed. **52**, 13057 – 13061 (2013).

[7] F. Wen, B. Li, Q. Wang, Y. Huang, Y. Gong, Y. He, P. Dong, J. Bellah, A. George, L. Ge, J. Lou, N. J. Halas, R. Vajtai, P. M. Ajayan, Nano Lett. **15 (1)**, 259-265 (2015).

[8] M. Acerce, D. Voiry, M. Chhowalla, Nat. Nanotech. **10**, 313-318 (2015).

[9] H. S. S. R. Matte, A. Gomathi, A. K. Manna, D. J. Late, R. Datta, S. K. Pati, C. N. R. Rao, Angew. Chem. Int. Ed. **49**, 4059 (2010).

[10] E. V. Calman, C. J. Dorow, M. M. Fogler, L. V. Butov, S. Hu, A. Mishchenko, A. K. Geim, Appl. Phys. Lett. **108**, 101901 (2016).

[11] H. Zeng, J. Dai, W. Yao, D. Xiao, X. Cui, Nat. Nanotechnol. **7**, 490–493 (2012).

[12] R. Sahu, D. Radhakrishnan, B. Vishal, D. S. Negi, A. Sil, C. Narayana, R. Datta, J. Cryst. Growth **470**, 51-57 (2017).

[13] K. Dileep, R. Sahu, S. Sarkar, S. C. Peter, R. Datta, J. Appl. Phys. **119**, 114309 (2016).

[14] S. Tongay, H. Sahin, C. Ko, A. Luce, W. Fan, K. Liu, J. Zhou,Y. Huang, C. Ho, J. Yan, D. F. Ogletree, S. Aloni, J. Ji, S. Li, J. Li, F. M. Peeters, J. Wu, Nat. Comm. **5**, 3252, (2014).

[15] X. Fan, Y. Yang, P. Xiao, W. Lau, J. Mater. Chem. A **2**, 20545 (2014).

[16] T. Hu, R. Li, J. Dong, J. Chem. Phys. **139**, 174702 (2013).

[17] K. K. Amara, Y. Chen, Y. Lin, R. Kumar, E. Okunishi, K. Suenaga, S. Quek, G. Eda, Chem. Mater. **28**, 2308-2314 (2016).

[18] A. Andersen, S. M. Kathmann, M. A. Lilga, K. O. Albrecht, R. T. Hallen, D. Mei, J. Phys. Chem. C **116**, 1826–1832 (2012).

[19] X. Rocquefelte, F. Boucher, P. Gressier, G. Ouvrard, P. Blaha, K. Schwarz, Phys. Rev. B **62**, 2397 (2000).

[20] X. Sun, Z. Wang, Z. Li, & Y. Q. Fu, Sci. Rep. **6**, 26666 (2016).

[21] L. Wang, Z. Xu, W. Wang, X. Bai, J. Am. Chem. Soc. **136**, 6693−6697 (2014).

[22] D. Yang, S. J. Sandoval, W. M. R. Divigalpitiya, J. C. Irwin, R. F. Frindt, Phys. Rev. B **43**, 12053 (1991).

[23] F. Wypych, T. Weber, R. Prins, Chem. Mater. **10 (3),** 723–727 (1998).

[24] X. Rocquefelte, F. Boucher, P. Gressier, G. Ouvrard, P. Blaha, K. Schwarz, Phys. Rev. B **62**, 2397 (2000).

[25] N. S. Shirodkar, U. V. Waghmare, Phys. Rev. Lett. **112**, 157601 (2014).

[26] B. Radisavljevic1, A. Radenovic, J. Brivio1, V. Giacometti, A. Ki, Nat. Nanotech **6**, 147-150 (2011).

[27] Y. Rong, Y. Sheng, M. Pacios, X. Wang, Z. He, H. Bhaskaran, J. H. Warner, ACS Nano, **10**, 1093-1100 (2015).

[28] T. Park, J. Suh, D. Seo, J. Park, D. Lin, Y. Huang, H. Choi, J. Wu, C. Jang, J. Chang Appl. Phys. Lett. **107**, 223107 (2015).

[29] M. Tahir, P. Vasilopoulos, F. M. Peeters, Phys. Rev. B **93**, 035406, (2016).

[30] M. Kertesz, and R. Hoffmann, J. Am. Chem. Soc. **106**, 3453-3460 (1984).

[31] F. Raffone, C. Ataca, J. C. Grossman, G. Cicero, J. Phys. Chem. Lett. **7**, 2304−2309 (2016).

[32] L. Yadgarov, D. G. Stroppa, R. Rosentsveig, R. Ron, A. N. Enyashin, L. Houben, R. Tenne Z. Anorg. Allg. Chem. **638 (15)**, 2610–2616 (2012).

[33] A. A. Tedstone, D. J. Lewis, P. O'Brien, Chem. Mater. **28**, 1965−1974 (2016).

[34] Qi -C. Sun, L. Yadgarov, R. Rosentsveig, G. Seifert, R. Tenne, J. L. Musfeldt ACS Nano **7**, 3506–3511 (2013).

[35] M. Chhetri, U. Gupta, L. Yadgarov, R. Rosentsveig, R. Tennec, C. N. R. Rao, Dalton Trans. **44**, 16399 (2015).

[36] K. Dolui, I. Rungger, C. D. Pemmaraju, S. Sanvito, Phys. Rev. B **88**, 075420 (2013).

[37] A. N. Enyashin, L. Yadgarov, L. Houben, I. Popov, M. Weidenbach, R. Tenne, M. Bar-Sadan, G. Seifer, J. Phys. Chem. C **115**, 24586–24591 (2011).

[38] P. Blaha, K. Schwarz, G. K. H. Madsen, D. Kvasnicka, and J. Luitz, WIEN2k: An Augmented Plane Wave + Local Orbitals Program for Calculating Crystal Properties (Karlheinz Schwarz, Techn. Universität Wien, Austria, (2001).

[39] S. Grimme, J. Antony, S. Ehrlich, H. Krieg, J. Chem. Phys. **132**, 154104 (2010).

[40] J. P. Perdew, K. Burke, M. Ernzerhof, Phys. Rev. Lett. **77**, 3865 (1996).

[41] S. Wook Han, W. Seok Yun, J. D. Lee, Y. H. Hwang, J. Baik, H. J. Shin, W. G. Lee, Y. S. Park, K. S. Kim, Phys. Rev B **92**, 241303(R) (2015).

[42] A. Singh, S. Shirodkar, U. V. Waghmare, 2D Mater. **2,** 035013 (2015).

[43] Y. Lin, D. O. Dumcenco, Y. Huang, K. Suenaga, Nat. Nanotech **9**, 391-396, (2014).

[44] C. Zhang, S. KC, Y. Nie, C. Liang, W. G. Vandenberghe, R. C. Longo, Y. Zheng, F. Kong, S. Hong, R. M. Wallace, K. Cho, ACS Nano **10 (8)**, 7370–7375 (2016).

[45] S. S. Chou, Y. Huang, J. Kim, B. Kaehr, B. M. Foley, P. Lu, C. Dykstra, P. E. Hopkins, C. J. Brinker, J. Huang, and V. P. Dravid, J. Am. Chem. Soc. **137**, 1742−1745 (2015).

Chapter IX

Conclusions and future perspectives

.

This chapter provides notes on the important conclusions drawn from the present thesis along with our future focus towards p-type ZnO, large scale epitaxial growth and $1T_d$ transition metal dichalcogenides.

9.1 Summary of the thesis

There are two different aspects covered in this thesis. First one is *p*-type doping problems and its solutions in ZnO and second one is epitaxial growth of TMDs by PLD and low dimensional phase modulation of $1T_d$ MoS_2 and WS_2. The salient features of the work are listed below;

- In the first part of the thesis, we have made significant contribution to solve *p*-type doping problem in ZnO. In depth study of defects and defects complexes using both experiments and density functional theory made clear how to compensate intrinsic effects to stabilize *p*-type ZnO.
- For valence band engineering, we have studied the ambipolar behaviour of Te atom incorporation, solubility, structural features and the corresponding optical property of epitaxial ZnO:Te thin film grown on *c*-plane sapphire by pulsed laser deposition. Ambipolar nature of Te at the oxygen (Te_O) or zinc (Te_{Zn}) site can be controlled through the deposition scheme to transfer Te during the film growth. Solubility of Te at the oxygen site is strongly dependent on the growth temperature. Decrease in band gap is found with Te incorporation both in the oxygen and zinc sites but decrease is more pronounced and composition dependent for the former case. An experimental band bowing parameter of ~7 eV is obtained for Te_O and in agreement with mBJLDA based theoretical calculation [1, 2].
- Both intrinsic and extrinsic defects are interesting to affect optoelectronic properties of ZnO. It is found that the oxygen vacancy (V_O) defects are affecting the separation between individual species in Li_{Zn}-Li_i defect complex to influence the optical property. Li_i compensates the *p*-type activity in this system. Atomic Li percentage and atomic position could be analysed from EELS and FEFF [3].
- We have observed the stable *p*-type conductivity in B and N co-doped epitaxial ZnO thin films grown by pulsed laser deposition [4]. This *p*-type conductivity is associated with the significant decrease in defect emission peaks due to the vacancy oxygen (V_O) and Schottky type-I native defects compared to films grown at low oxygen partial pressure (~10^{-5} Torr). Off-stoichiometric BN_{1+x} is found to be good dopant and resulted in *p*-type conductivity in ZnO.

- In the second part of this thesis, we have solved two important issues in the field of 2D transition metal dichalcogenides; i) large scale epitaxial growth and ii) $1T_d$ phase stability of MoS_2 and WS_2 TMDs.
- Large area MoS_2 and WS_2 Van der Waals epitaxial thin films with complete control over number of layers including monolayer is grown on *c*-plane sapphire by pulsed laser deposition utilizing slower growth kinetics [5]. The stiffening of A_{1g} and E^1_{2g} phonon modes with decreasing number of layers for both MoS_2 and WS_2 show compressive strain with accompanying increase in fundamental direct band gap for monolayer MoS_2 and WS_2, respectively. The strain decays with the number of layers. The results demonstrate a practical route to stabilize and engineer strain for this class of material over large area device fabrication.
- Various types of Peierls like two dimensional structural modulations and relative phase stability of 2H and 1T poly-types in $Re_xMo_{1-x}S_2$ and $Re_xW_{1-x}S_2$ alloy system have been studied [6]. DFT calculation predicts a poly-type phase transition cross over at ~50 at.% of Mo and W in ReS_2 in both monolayer and bulk form, respectively. The 50% alloy system is found to be a suitable monolithic candidate for metal semiconductor transition with minute external perturbation. The results offer yet another effective way to tune the electronic structure and poly-type phases of this class of materials other than intercalation, strain, and vertical stacking arrangement.

9.2 Future perspectives

9.2.1 *p*-type ZnO

Primary success in *p*-type doping of ZnO has been achieved in B and N co-doping in ZnO by PLD by following the *r*-type growth scheme described in chapter V. Now our future plan is;

- Finding a way to increase carrier concentration and mobility for device application.
- Fabrication of bipolar devices for photovoltaic, LEDs, LD and UV emitters for water purification.

9.2.2 2D transition metal dichalcogenides

There are lots of scopes in the 2D transition metal dichalcogenides field after our two major goals. We are able to control the number of MoS_2 and WS_2 in large scale and stabilize $1T_d$ form in ambient condition. Now our aim is to study;

- Layer control growth of hetero-structure by PLD and their opto-electronic properties and device applications.
- Practical novel devices based on the TMDs and TMDs based hetero-structures grown over large area by PLD.
- Thinnest ferroelectric property of trimmer modulation (alloy system) experimentally and their device applications [7].
- Hydrogen evolution reaction for $1T_d$ alloy system.

9.3 Bibliography

[1] R. Sahu, K. Dileep, D. S. Negi, K. K. Nagaraja, S. Shetty, R. Datta, J. Cryst. Growth **410**, 69-76 (2015).

[2] R. Sahu, K. Dileep, D.S. Negi, K. K. Nagaraja, R. Datta, Phys. Stat. Solidi (b) **252 (8)**, 1743-1748 (2015).

[3] R. Sahu, K. Dileep, B. Loukya, R. Datta, Appl. Phys. Lett. **104**, 051908 (2014).

[4] R. Sahu, H. B. Gholap, G. Mounika, K. Dileep, B. Vishal, S. Ghara, R. Datta, Phys. Stat. Solidi (b) **253 (3)**, 504-508 (2016).

[5] R. Sahu, D. Radhakrishnan, B. Vishal, D. S. Negi, A. Sil, C. Narayana, R. Datta, J. Cryst. Growth **470**, 51-57 (2017).

[6] R. Sahu, U. Bhat, N. M. Batra, H. Sharona, B. Vishal, S. Sarkar, S. Assa Aravindh, S. C. Peter, I. S Roqan, P. M. F. J. D. Costa, R. Datta, J. Appl. Phys. **121**, 105101 (2017).

[7] N. S. Shirodkar, U. V. Waghmare, Phys. Rev. Lett. **112**, 157601 (2014).